FOSSIL ENERGY

DOE/BC/15213-1
(OSTI ID: 760868)

ADVANCED TECHNIQUES FOR RESERVOIR SIMULATION AND MODELING OF NON-CONVENTIONAL WELLS

Annual Report
September 1, 1999-August 31, 2000

By
Louis J. Durlofsky

Date Published: August 2000

Work Performed Under Contract No. DE-AC26-99BC15213

Stanford University
Stanford, California

National Petroleum Technology Office
U.S. DEPARTMENT OF ENERGY
Tulsa, Oklahoma

DOE/BC/15213-1
Distribution Category UC-122

Advanced Techniques for Reservoir Simulation and Modeling of Non-Conventional Wells

By
Louis J. Durlofsky

August 2000

Work Performed Under Contract No DE-AC26-99BC15213

Prepared for
U.S. Department of Energy
Assistant Secretary for Fossil Energy

Thomas B. Reid, Project Manager
National Petroleum Technology Office
P.O. Box 3628
Tulsa, OK 74101

Prepared by
Department of Petroleum Engineering
School of Earth Sciences
Stanford University
Stanford, CA 94305-2220

Contents

1. General Introduction 1

Part I. Development of Advanced Reservoir Simulation Techniques for Modeling Non-Conventional Wells 5

2. Modular Gridding and Discretization for Reservoir Simulation 5
2.1 Description of Numerical Issues and Overall Work Plan 5
2.2 Modular Grid Generation 7
2.2.1 Algebraic Grid Generation 7
2.2.2 Elliptic Grid Generation 8
2.2.3 Flow Based Grid Generation 8
2.3 Discretization 12
2.3.1 Flow Equations 12
2.3.2 Finite Volume Schemes 13
2.3.3 Two Dimensional Formulation 15
2.3.4 Three Dimensional Hexahedral Approximations 18
2.3.5 Flux Continuous Schemes 19
2.3.6 Split Tensor Flux on a Structured Grid 23
2.3.7 Unstructured Grids 25
2.4 Simulation Results 25
2.5 Future Directions 27
2.6 References 33

Part II. Coupling of the Reservoir and Non-Conventional Wells in Simulators 35

3. Semi-Analytical Calculation of Productivity Index and Well Index 35
3.1 Semi-Analytical Solution Technique 39
3.2 Incorporation of Skin in Semianalytical Solution 43
3.3 Representation of Heterogeneity with s and k* 44
3.4 Examples 48
3.4.1 Anisotropic Reference Case 49
3.4.2 Fixed Flow Rate Cases 51
3.4.3 Fixed Pressure Cases 55
3.4.4 Multilateral Case 57
3.4.5 Complex Trajectory with Wellbore Hydraulics 59
3.5 Assessment of the Combined Effects of Heterogeneity and Wellbore Pressure Drop 61
3.5.1 Calculation of Well Productivity 61
3.6 Numerical Examples 63
3.6.1 Long Horizontal Wells 64
3.6.2 Short Horizontal Wells 67
3.6.3 Dual-lateral Wells 69
3.7 Discussion and Conclusions 71
3.8 Future Directions 72
3.9 References 73

4. Pressure Drop in the Wellbore 77
4.1 Introduction 77
4.2 Modeling Results for Single Phase Flow in Horizontal Wells 78
4.2.1 Pressure Drop Calculation 79
4.2.2 Friction Factor with Wall Inflow 79
4.3 Experimental Data 81
4.3.1 Stanford/Marathon Experiments 82
4.3.2 Norsk Hydro Experiments 83
4.3.3 Tulsa University Experiments 83
4.4 Comparison of Correlations with Experimental Data 84
4.4.1 Effect of Perforation Density 87
4.5 Conclusions and Future Directions 91
4.6 References 91

Part III. Novel Approaches to Account for Heterogeneities in the Vicinity of Non-Conventional Wells 93

5. Accurate Course Scale Simulation of Horizontal Wells in Heterogeneous Reservoirs 93
5.1 Introduction 93
5.2 Near-Well Upscaling Methodology 95
5.2.1 Local Fine Grid Flow Problem 95
5.2.2 Local Course Grid Flow Problem 99
5.3 Numerical Results for Flow Driven by Horizontal Wells 103
5.3.1 Single Phase Flow Results 104
5.3.2 Three Phase Flow Results 111
5.4 Conclusions and Future Directions 114
5.5 References 115

6. Approximate Finite Difference Modeling of the Performance of Horizontal Wells in Heterogeneous Reservoirs 117
6.1 Introduction 118
6.2 Permeability Representation with *s* and k* 119
6.3 Simplified Finite Difference Modeling of Horizontal Wells in Heterogeneous Reservoirs 120
6.3.1 Fixed Total Liquid Rate Cases 123
6.3.2 Fixed Oil Rate Cases with BHP Constraint 129
6.3.3 Unfavorable Mobility Ratio Displacements 132
6.3.4 Use of *s*-k* Representation on Coarser Grids 133
6.4 Discussion and Conclusions 138
6.5 References 139

7. Potential Application of New Modeling Approaches to Simulation While Drilling 141

Executive Summary

The use of non-conventional wells, which include horizontal, deviated, multilateral and "smart" wells, is essential for the efficient management of oil and gas reservoirs. These wells are able to contact larger regions of the reservoir than vertical wells and can also be used to target isolated hydrocarbon accumulations. Because non-conventional wells can be very expensive to drill and complete, it is important to be able to accurately model their performance. However, predictions of non-conventional well performance are often inaccurate. This is likely due in part to inadequacies in many of the reservoir engineering and reservoir simulation tools used to model non-conventional wells.

Several complexities arise in non-conventional well modeling that do not exist, or exist to a much lesser extent, with vertical wells. For example, non-conventional wells, due to their geometric complexity, intersect reservoir features non-orthogonally. Accurate reservoir simulation models of non-conventional wells therefore require the use of more advanced gridding and discretization techniques. In some cases, however, the construction of a detailed finite difference simulation model is not warranted and the use of an alternative, more approximate technique is appropriate. One such approach is the use of a semi-analytical model based on Green's functions. These models are highly efficient but are limited because they do not include all of the important effects that may influence well performance. Extensions of existing methods to approximate additional physics, such as the effects reservoir heterogeneity, would improve their usefulness considerably.

The effects of pressure losses in the wellbore, which are generally negligible for vertical wells, can be important for non-conventional wells and therefore must be modeled. Several correlations for pressure drop in horizontal wells exist, though these were generally developed independently and with reference to limited experimental data. The unification and extension of the existing correlations to model all of the available data are therefore needed. Another important aspect of non-conventional well modeling is the accurate representation of the reservoir heterogeneity in finite difference simulation models. The effects of near-well permeability variation on well performance can be very substantial, and the use of standard techniques for upscaling may lead to inaccurate simulation models.

The research proposed in our five year project addresses all of the areas discussed above. The work is divided into three main categories: (1) advanced reservoir simulation techniques for modeling non-conventional wells; (2) improved techniques for computing well productivity (for use in reservoir engineering calculations) and well index (for use in simulation models); and (3) accurate approaches to account for heterogeneity in the near-well region. Our progress through the first year of funding in each of these main areas is as follows.

We are actively developing new gridding and discretization techniques for the accurate representation of non-conventional wells and other geometrically complex reservoir features. We are emphasizing a so-called modular approach, in which different regions of the reservoir can be gridded using different grid systems. Improved discretization techniques are also required because the simulation grids are in general non-orthogonal and permeability is in general a full tensor quantity. To date, we have developed and implemented techniques for efficiently simulating such systems when the local grids (i.e., each

grid module) are structured. Detailed simulation results for two phase systems, illustrating the significant improvement in accuracy and efficiency offered by our new techniques relative to standard approaches, are presented. In the future, we plan to extend our approaches to unstructured modules and to develop improved strategies for gridding.

We next present the development and application of a new semi-analytical method for the approximate modeling of non-conventional wells in heterogeneous reservoirs. The approach is based on a new representation of reservoir heterogeneity that is in a form simple enough for use in the semi-analytical technique but that captures some essential physics. Comparisons of semi-analytical results with detailed finite difference simulations illustrate the generally high level of accuracy attainable using our new procedure. We then apply the semi-analytical methodology to a detailed study of the combined effects of reservoir heterogeneity and wellbore hydraulics on the performance of non-conventional wells. In the future, we plan to extend these approaches to model more complex ("smart") wells and to use our semi-analytical results to determine accurate well indexes for use in finite difference reservoir simulation.

The development and testing of a new correlation for pressure drop in horizontal wells is described next. This correlation models the frictional component of the wellbore pressure drop, accounting for the effects of inflow into the well through the perforations. The effects of fluid acceleration are modeled separately. Using the new correlation, improved agreement with experimental data from three different sources is obtained. In the future, we intend to model two and three phase wellbore flows and to investigate ways to efficiently introduce our wellbore flow models into finite difference reservoir simulators.

The third portion of this report describes the development of new approaches for capturing the effects of reservoir heterogeneity on well performance in coarse scale finite difference models. We present two such approaches. The first method is appropriate for use in finite difference models generated via a detailed upscaling of the fine grid permeability field. This method, which is a general near-well upscaling technique, is shown to provide coarse scale simulation results in close agreement with reference fine scale results for horizontal well problems. Results for both single phase and three phase flow problems are presented. The second method is more approximate (though it is easier to apply) and entails the use of the simplified permeability representation referred to above. Despite its simplicity, this method is shown to provide reasonable coarse scale simulation results for many flow quantities of interest. Future work will be geared toward extending these approaches to treat general non-conventional wells and to implementing the near-well upscaling technique within the context of modular gridding.

Finally, we briefly discuss the eventual incorporation of many of the methodologies described in this report into a Simulation While Drilling modeling tool. Such a tool would allow for the optimization of the well length and trajectory during the actual drilling operation. In the future, we plan to begin applying some of our new methods to this challenging and important problem.

Abstract

Research results for the first year of a five year project on the development of improved modeling techniques for non-conventional (e.g., horizontal, deviated or multilateral) wells are presented. New reservoir simulation techniques, able to provide accurate geometric representations of non-conventional wells, are developed and applied. Simulation results demonstrate significant improvements in accuracy relative to current techniques. A new and efficient semi-analytical technique based on Green's functions for the approximate modeling of non-conventional well performance is also developed. This method, appropriate under single phase flow conditions, includes an approximate treatment of the effects of reservoir heterogeneity. Results using this model compare well to reference finite difference simulations. A new correlation for wellbore pressure drop is developed. This correlation is able to accurately model a wider variety of experimental data than previous correlations. New methods for modeling the effects of near-well reservoir heterogeneity on well performance in coarse scale finite difference models are presented. These methods are shown to provide considerably more accurate results than standard techniques. Future work will be directed toward the extension of the methods to more general cases involving unstructured simulation grids, more complex wells and multiphase wellbore flow.

Publications from this Work:

- Castellini, A., Edwards, M.G. and Durlofsky, L.J.: "Flow Based Modules for Grid Generation in Two and Three Dimensions," Proceedings of the 7th European Conference on the Mathematics of Oil Recovery, Baveno, Italy, Sept. 5-8, 2000.
- Durlofsky, L.J.: "An Approximate Model for Well Productivity in Heterogeneous Porous Media," *Math. Geol.*, **32**, 421-438, 2000.
- Edwards, M.G.: "M-matrix Flux Splitting for General Full Tensor Discretization Operators on Structured and Unstructured Grids," *J. Comp. Phys.* **160**, 1-28, 2000.
- Mascarenhas, O. and Durlofsky, L.J.: "Coarse Scale Simulation of Horizontal Wells in Heterogeneous Reservoirs," *J. Pet. Sci. and Eng.*, **25**, 135-147, 2000.
- Wolfsteiner, C., Durlofsky, L.J. and Aziz, K.: "Approximate Model for Productivity of Nonconventional Wells in Heterogeneous Reservoirs, *SPEJ*, 218-226, June 2000.
- Wolfsteiner, C., Durlofsky, L.J. and Aziz, K.: "Efficient Estimation of the Effects of Wellbore Hydraulics and Reservoir Heterogeneity on the Productivity of Non-Conventional Wells," paper SPE 59399 presented at the SPE Asia Pacific Conference, Yokohama, Japan, April 25-26, 2000.
- Yeten, B., Wolfsteiner, C., Durlofsky, L.J. and Aziz, K.: "Approximate Finite Difference Modeling of the Performance of Horizontal Wells in Heterogeneous Reservoirs," paper SPE 62555 presented at the SPE Western Regional Meeting, Long Beach, June 19-23, 2000.

Presentations on this Work were given at the Following Conferences:

- International Energy Agency Workshop and Symposium, Paris, Sept. 1999
- Stanford - Heriot-Watt Reservoir Description Forum, Perthshire, UK, Sept. 1999
- SPE Annual Technical Conference and Exhibition, Houston, Oct. 1999
- Institute of Mathematics and Its Applications, Minneapolis, Feb. 2000
- SPE Asia Pacific Conference, Yokohama, Japan, April 2000
- SPE Western Regional Meeting, Long Beach, June 2000
- DOE Oil Technology Program – Contractor Review Meeting, June 2000
- Gordon Research Conference, Andover, New Hampshire, Aug. 2000

1 General Introduction

Reservoir simulation and related technologies (e.g., geologic modeling, data integration, and upscaling) have advanced considerably in recent years. As a result, reservoir simulation now represents the primary tool for reservoir management. However, significant challenges still remain in several key areas. One of the most important of these is in the modeling of non-conventional wells, which include horizontal, multilateral and other highly complex wells. Accurate tools for modeling such wells are extremely important, as the costs for drilling and completing wells of this type are very high. However, many of the existing simulation approaches, which are adequate for the modeling of vertical wells, are not suitable for non-conventional wells.

Significant complexities appear in non-conventional well modeling for several reasons. These wells, due to their geometric complexity, intersect reservoir features non-orthogonally. Therefore, more general gridding, discretization and solution techniques are required to accurately describe their performance. In addition, existing tools for coupling the well to the reservoir may not be adequate for non-conventional wells. The well index, which is the specific quantity that couples the well to the reservoir in simulation models, is closely related to the productivity index, a basic reservoir engineering quantity. Both quantities relate the well production rate to an imposed pressure drop. The determination of improved well indexes for non-conventional wells in simulation models is therefore closely linked to the determination of an accurate productivity index for non-conventional wells. In addition, effects due to pressure losses in the wellbore, which are generally negligible for vertical wells, can be important for non-conventional wells and therefore must be modeled. Another important aspect of non-conventional well modeling is the accurate representation of the effects of near-well heterogeneity in the simulation model. These effects can be very substantial, and existing techniques for near-well heterogeneity representation may be inaccurate or overly time consuming.

Our work in this project is directed toward significantly improving modeling approaches in the three main areas discussed above. Specifically, this project targets the development of (1) advanced reservoir simulation techniques for modeling non-

conventional wells; (2) improved techniques for computing well productivity (for use in reservoir engineering calculations) and well index (for use in simulation models), including the effects of wellbore flow; and (3) accurate approaches to account for heterogeneity in the near-well region. We now discuss each of these issues in more detail.

Because non-conventional wells introduce significant geometric complexity into the simulation model, standard Cartesian approaches or simple corner point models may not be appropriate. In the vicinity of the well, more general grid systems, locally aligned with the well, may be required. Because the type of grid appropriate for the near-well region may not be the grid type most suitable for the bulk of the reservoir, we are developing a so-called multi-block or modular gridding approach. Modular gridding allows for the use of different grid types in different regions of the reservoir. For example, around a deviated or horizontal well the grid might be radial (or nearly so); in the vicinity of a complex multilateral well the grid could be fully unstructured. Examples of fully unstructured grid systems include grids based on tetrahedral, pyramid, or prismatic elements.

Our work on multi-block grids is described in Part 1 (Chapter 2) of this report. The development and use of a modular approach to grid generation and simulation is complicated for several reasons. For example, gridding and discretization techniques must be developed for each of the grid types included. We describe in detail our recent work directed toward the development of simulation models based on modular grids. Methods for the accurate treatment of full tensor permeabilities and non-orthogonal (and non-K-orthogonal) grids are described. The significant errors inherent in existing approaches, and the improved results attainable using our new methodology, are clearly demonstrated through a variety of two and three dimensional examples.

The use of semi-analytical techniques (based on Green's functions) for modeling the performance of non-conventional wells operating under single phase flow conditions represents an alternative to the use of detailed finite difference simulation in some cases. Such models are appropriate both for the estimation of productivity index and well index. We recently extended existing semi-analytical methods to approximately account for the effects of near-well heterogeneity. In Part II (Chapter 3) of this report we describe the

development and application of our new methods to the modeling of non-conventional wells in heterogeneous reservoirs. We first present the basic approach and illustrate its level of accuracy relative to reference finite difference solutions. We then apply the approach to a detailed study of the combined effects of wellbore hydraulics and reservoir heterogeneity. Our results illustrate the importance of reservoir heterogeneity and, in some cases, wellbore hydraulics. These results further demonstrate the large amount of variation in well performance that is observed between different geostatistical realizations.

In Part II (Chapter 4) we also describe the development of a new correlation for pressure drop in a horizontal well. This correlation represents the pressure drop due to friction and accounts for the effects of inflow (flow into the well through perforations). Improved agreement between the correlation and experimental data from a variety of sources (Stanford / Marathon, Norsk Hydro and Tulsa University), relative to that attainable using existing correlations, is clearly demonstrated.

The third important area we are targeting is the improved representation of the effects of near-well heterogeneity in coarse scale finite difference models. Geostatistical modeling approaches are capable of providing finely gridded geological characterizations, though these models are often too detailed to be practically useful for reservoir simulation. Some type of averaging, or upscaling, is therefore required. Many such approaches have been developed and existing methods are capable of providing accurate coarse scale reservoir descriptions in regions away from wells. In the near-well region, however, standard upscaling approaches can yield significant inaccuracies and improved coarse scale descriptions are necessary.

In Part III (Chapters 5 and 6) we present methods capable of providing coarse scale finite difference models of horizontal wells. The method described in Chapter 5 is a general approach, appropriate for use in finite difference models generated via the detailed upscaling of the fine grid permeability description. This method is demonstrated to provide accurate coarse scale flow results for single phase and three phase flow problems involving horizontal wells in highly complex heterogeneity fields. The method described in Chapter 6 is much simpler and easier to apply, though it is also more approximate.

This method entails the representation of the reservoir in terms of a constant (anisotropic) permeability and a near-well effective "skin," which accounts for near-well heterogeneity. Despite its simplicity, this method is shown to provide reasonably accurate coarse scale simulation results for many flow quantities of interest.

Finally, in Chapter 7, we describe how several of the approaches described in the preceding chapters can be combined to provide a Simulation While Drilling capability. This capability would allow for the real time optimization of the well length and trajectory during the actual drilling operation and could result in significant cost savings.

We note that some of the work presented in this report was performed prior to the official start of the funding period (September, 1999). This work represents research proposed in our original proposal (submitted April, 1998) but begun prior to September, 1999. This work was funded under our industrial affiliates programs (SUPRI-B, SUPRI-HW) and is included in this report because it represents a portion of the work originally proposed to DOE.

Part I. Development of Advanced Reservoir Simulation Techniques for Modeling Non-Conventional Wells

A key aspect of our overall research is the development of general simulation approaches for the modeling of complex reservoirs. Our work in this area involves the development of a modular reservoir simulator with general gridding and discretization capabilities. Here we describe our approaches for gridding and discretization and present results illustrating the powerful capabilities of the modular approach.

2 Modular Gridding and Discretization for Reservoir Simulation

by Michael G. Edwards

2.1 Description of Numerical Issues and Overall Work Plan

The goals of this work are to develop numerical methods and grid generation techniques for reservoir simulation that can accommodate general three dimensional deviated wells and complex reservoir geometry and geology. Both the development of grid generation techniques and numerical methods that can reliably compute the physically correct solution to complex simulation problems on three dimensional flexible grids are under study. Structured and unstructured grid generation techniques are being developed. The aim here is to retain a structured grid whenever possible while allowing for unstructured grids when necessary. The need for unstructured grids can arise locally when faithfully modeling complex deviated wells, faults, pinchouts or when increasing local grid resolution (Local Grid Refinement). In addition, for other more complex reservoir boundaries, the task of generating a grid can sometimes be simplified by employing direct triangulation. To allow general flexibility a multiblock method is being developed, where the reservoir domain can be decomposed into a structured or unstructured set of subdomains. In the work presented here, each subdomain grid is structured (logically Cartesian). Future work will include the development of interfaces that will allow a discontinuous change in logical coordinate density so that locally unstructured grids can be used for specific regions or subdomains of the reservoir.

A major assumption in most of today's commercial simulators is that the pressure equation always has a diagonal tensor. The design and efficiency of such codes is intrinsically linked to the diagonal tensor assumption. However, this assumption is only true if the computational grid is aligned with the principal axes of the tensor. In general a full tensor pressure equation arises in reservoir simulation whenever (a) the medium is anisotropic and non-aligned with the local coordinate directions, (b) upscaling (with cross-flow effects included) is used to compute the grid block permeability tensors or (c) non-K-orthogonal structured and unstructured grids are employed. Consequently, in general, all diagonal tensor simulators will suffer from $O(1)$ errors in flux (Aavatsmark et al., 1997; Arbogast et al., 1995; Edwards, 1997, 1998; Edwards and Rogers, 1998) when applied to cases involving these major features. For example, while these simulators appear to allow for non-K-orthogonal grids through the definition of corner point geometry, only the diagonal tensor permeability-geometry contribution to the flux is included, thus leading to an $O(1)$ error in flux (even for the Laplace equation) on a non-orthogonal grid (Edwards, 1998).

Consistent full tensor schemes are being developed for modeling problems with generally discontinuous full tensor coefficient fields in three dimensions. However, the introduction of a full tensor typically increases the support of the standard scheme on a logically Cartesian grid from 5 to 9 nodes in 2-D and from 7 to 27 nodes in 3-D. This represents a potentially large increase in computational cost, as the pressure field is recalculated at every time step of the simulation.

In addition to developing full tensor discretization schemes, the efficiency of the solution process is also being addressed. A general operator splitting formulation is under development which enables full tensor solutions to be computed while using reduced operator matrices that generally reduce computation time compared to full matrix inversion. In addition, full tensor operators can be included with minimal code changes. A summary of the properties of the finite volume schemes is presented. The schemes are applied to a number of problems involving strong cross-flow due either to the local or global orientation of the grid relative to the problem. Benefits of the method are clearly demonstrated.

2.2 Modular Grid Generation

Generation of a grid via a single technique such as an algebraic method (Gordon and Hall, 1973), Thompson mapping (Thompson et al., 1985), conformal mapping or even streamlines and equipotentials may prove to be adequate for certain reservoir types. While such possibilities are not disregarded, methods of grid generation are sought that will allow greater flexibility for general purpose reservoir simulation. Rather than generate problem specific grids, the approach adopted here is to build the reservoir grid from a set of modular grids, where each local grid is appropriately chosen according to the local geometry, geology and/or mean (representative) flow conditions. Accordingly, the reservoir is decomposed into a set of subdomains. Let us assume that for each well in the reservoir an appropriate *well* module can be defined which resolves the local heterogeneities. It then remains to define the grids for subdomains without wells. We shall call the latter grids *field* modules. Since the well modules will occupy a relatively small volume of the reservoir the larger component of grid generation will be performed using *field* modules. The advantages of this strategy are that the *field* modules can be generated independently using the most appropriate grid generation method locally.

Thus far a basic three dimensional multiblock algorithm has been developed. The reservoir domain is decomposed into either a structured or unstructured set of subdomains where each subdomain grid (or *field* module) is currently structured (logically Cartesian). The subdomain grid generation techniques employed include the algebraic transfinite interpolant method (Gordon and Hall, 1973), elliptic grid generation (Thompson et al., 1985) and flow based grid generation (Castellini et al., 2000; Durlofsky et al., 1997; Edwards et al., 1998; Edwards et al., 1999; Portella and Hewett, 1998; Tran, 1995).

2.2.1 Algebraic Grid Generation. The default grid is defined by the transfinite interpolant method which is illustrated in two dimensions below:

$$\mathbf{r}(\xi_1,\xi_2) = (1-\xi_2)\mathbf{r}_S(\xi_1) + \xi_2\mathbf{r}_N(\xi_1) + (1-\xi_1)\mathbf{r}_W(\xi_2) + \xi_1\mathbf{r}_E(\xi_2) \\ -((1-\xi_1)\xi_2\mathbf{r}_N(0) + \xi_1\xi_2\mathbf{r}_N(1) + (1-\xi_1)(1-\xi_2)\mathbf{r}_S(0) + \xi_1(1-\xi_2)\mathbf{r}_S(1)) \quad , \tag{2-1}$$

where $\mathbf{r} = (x, y)$ and (ξ_1, ξ_2) are the transform variables. An example is given in **Fig. 2-1**. Subdomain decomposition is illustrated in **Fig. 2-2** where the logical subdomain corners are indicated with nodes. Note that the right hand subdomain 3 has two neighboring surfaces that are parallel; this enables a singularity to be treated with a quadrilateral grid. After domain subdivision the algebraic interpolant grid generation method is used to generate a local grid in each subdomain (**Fig. 2-3**). A major benefit of this technique is that the grid generation for each subdomain is performed independently and is almost instantaneous due to the use of interpolants.

2.2.2 Elliptic Grid Generation. The term "elliptic grid generation" is used here to denote a class of grid generation techniques that involve solving a coupled set of elliptic partial differential equations to generate grid coordinates. Many variants have been proposed with various forms of grid control functions. One of the most well known approaches is the Thompson mapping (Thompson et al., 1985). The Laplacian system is one of the simplest members of the above class and is also used here. The Laplacian system is given by

$$\nabla^2\mathbf{r} = 0 \tag{2-2}$$

and is solved directly for the position vector coordinates $\mathbf{r} = (x, y, z)$. The Laplacian smoothing technique provides a means of globally or locally generating a grid directly by solving the system of Eq. 2-2 subject to boundary coordinate constraints. The method can also be used to smooth a grid (Laplacian smoothing) generated by an alternative method. The smoothing process involves applying an iterative relaxation method to solve the system of Eq. 2-2 and performing an "incomplete solve" with just a small number of iterations. For example, after smoothing the grid of Fig. 2-3, the final grid is shown in **Fig. 2-4**.

2.2.3 Flow Based Grid Generation. The term "flow based grid generation" is used here to denote grids that are generated by using streamline or flow field information to

determine local grid node density and coordinate line orientation. When heterogeneity is present key requirements of an optimal subdomain module are that the grid be dense in high flow regions so as to resolve connected flow paths of the reservoir or subdomain.

In this work the flow field information used for modular grid generation is determined via a local single phase flow response obtained by solving the pressure equation over a subdomain subject to mean flow boundary conditions. The choice of boundary conditions is not unique and their effects are currently being studied.

Streamlines that result from a local flow response are naturally clustered in high velocity regions and flow paths of the module. This streamline information is used to automatically concentrate fine grid cells in important flow regions. For example, a flow based grid can be built from the streamlines and equipotentials of the mean flow problem. Such grids have been proven to be K-Orthogonal (Edwards, 1999), meaning that the local general geometry-permeability tensor is always strictly diagonal. Thus K-Orthogonality, together with the natural clustering properties of streamlines, provides strong motivation for developing flow modules based on local streamline information.

The *modular* strategy allows flow based grids to be generated locally and independently while only requiring that the pressure equation be solved over the local subdomain (Castellini et al., 2000; Edwards, 1999). Flow based modules are of prime importance for generally heterogeneous regions and fluvial and channeled subdomains. The flow based strategy is currently under development and will be discussed in more detail in a future report.

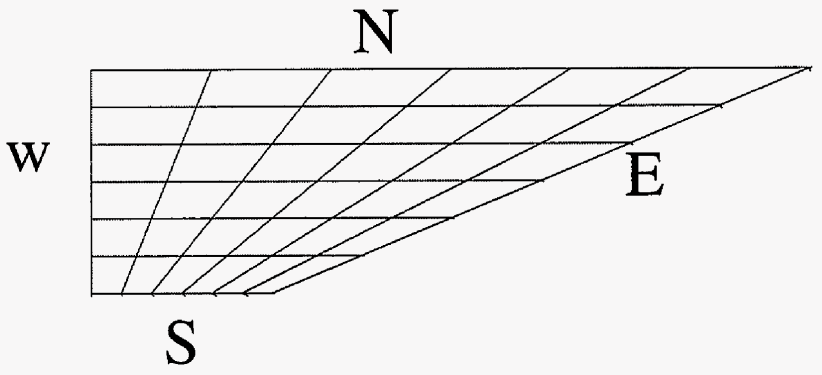

Fig. 2-1: Algebraic Grid

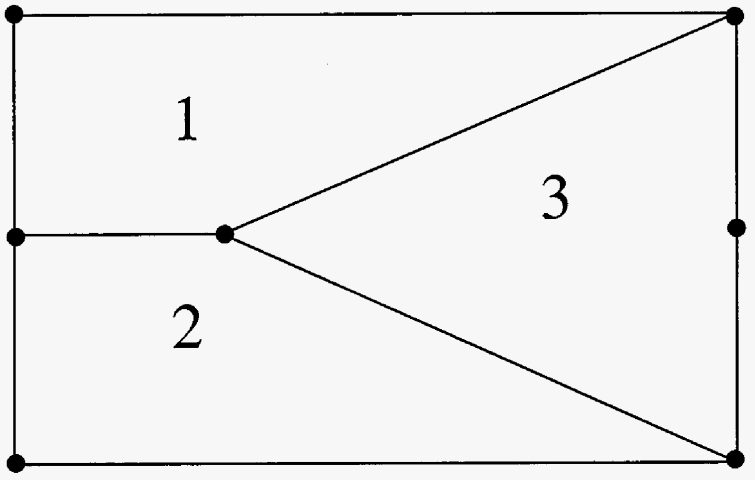

Fig. 2-2: Multiblock: 3 subdomains

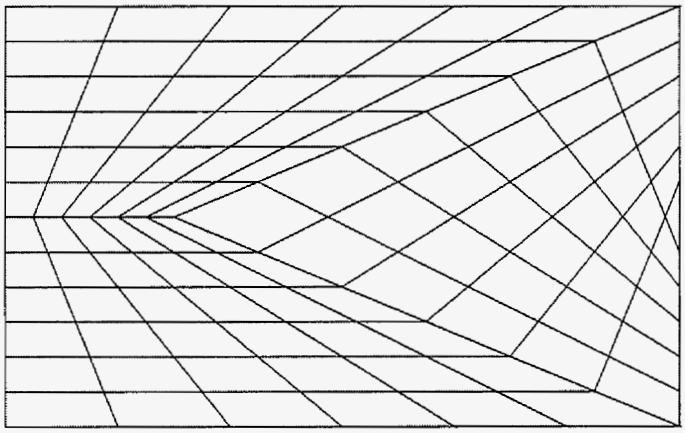

Fig. 2-3: Algebraic multiblock grid

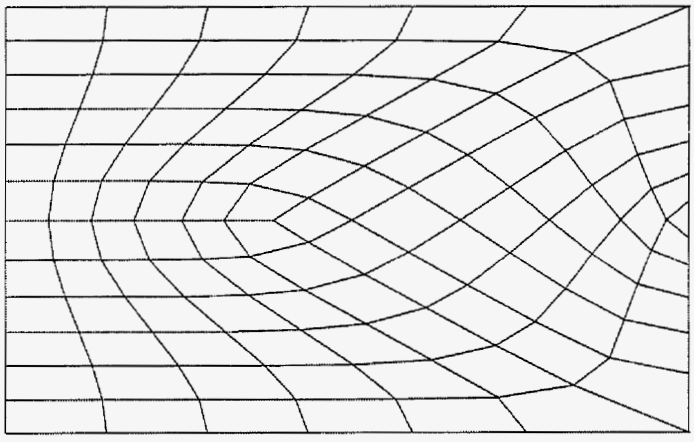

Fig. 2-4: Algebraic grid after smoothing

2.3 Discretization

2.3.1 Flow Equations. Without loss of generality, the schemes presented here are illustrated with respect to two phase flow models, with unit porosity and with capillary pressure neglected. The continuity equation for each phase $j = 1,...N_p$ (here $N_p = 2$) is written as

$$\int_{\Omega} \left(\frac{\partial s_p}{\partial t} + \nabla \bullet \mathbf{v}_p\right) d\tau = m_p(x, y) \ , \tag{2-3}$$

where the integral is taken over domain Ω and $\nabla = (\partial_x, \partial_y)$. Here s_p and m_p are the *pth* phase saturation and specified phase flux respectively. Since the pore volume must always be filled by the fluids present, this gives rise to the volume balance

$$\sum_{p=1}^{N_p} s_p = 1 \ . \tag{2-4}$$

The momentum equations are defined through Darcy's law where

$$\mathbf{v}_p = -\lambda_p \mathbf{K}(\nabla \phi - \rho g \nabla h) \ , \tag{2-5}$$

is the *pth* phase velocity, $\mathbf{K}$ is the (diagonal) absolute permeability tensor, ϕ is the pressure and the *pth* phase mobility is given by

$$\lambda_p = k_{rp}(s_p)/\mu_p \ , \tag{2-6}$$

where μ_p and k_{rp} are the respective phase viscosity and relative permeability. Neumann boundary conditions apply on the boundary $\partial\Omega$ and require zero flux on boundaries together with reflection conditions for saturation. Inflow-outflow conditions apply at wells where fluxes are prescribed together with Dirichlet conditions for saturation. Pressure must be specified at least once for incompressible flow. Initial data in terms of saturation and pressure fields are also prescribed. Further details can be found in Aziz and Settari (1979).

The conservation laws of Eq. 2-3 are now formulated in general curvilinear coordinates (ξ_1, ξ_2, ξ_3). First the system is integrated over a control volume with surface $\partial\Omega_{CV}$ using the Gauss flux theorem to yield

$$\int_{\Omega_{CV}} \frac{\partial s_p}{\partial t} d\tau + \oint_{\partial\Omega_{CV}} \mathbf{v}_p \bullet \hat{\mathbf{n}} ds = m_p \ . \tag{2-7}$$

In order to simplify notation gravity will be omitted from the formalism. However, once the discrete flux is defined, gravity can be included immediately. The closed surface integral of phase velocity can now be expressed as the sum of the outward normal fluxes F_i over the surfaces of a cuvilinear control volume, viz

$$\oint_{\partial\Omega_p} \mathbf{v}_p \bullet \hat{\mathbf{n}} ds = \sum_{i=1}^{2Nd} \mathsf{F}_i \ , \tag{2-8}$$

where Nd is the spatial dimension. The outward normal flux is given by

$$\mathsf{F}_i = -\int \lambda_p \sum_{j=1}^{Nd} T_{ij} \phi_{\xi_j} d\Gamma \ , \tag{2-9}$$

where

$$T = |J| J^{-1} K J^{-T} \ , \tag{2-10}$$

is the general tensor which is function of the Cartesian permeability tensor and geometry, and $J_{i,j} = \partial x_i / \partial \xi_j$ is Jacobian of the curvilinear coordinate transformation.

2.3.2 Finite Volume Schemes. The most common reservoir simulation schemes are cell (block) centered or point distributed where flow variables and rock properties are assumed to have piecewise constant variations with respect to the control-volumes of the mesh. The permeability tensor is assumed to be diagonal and control-volume face fluxes are proportional to the harmonic mean of adjacent cell permeabilities multiplying their corresponding discrete pressure differences; e.g., at face $(i+1/2, j, k)$ the flux takes the well known form

$$F_{i+1/2,j,k}(\phi) = -\frac{2K_{11i,j,k}K_{11i+1,j,k}\Delta y}{(K_{11i,j,k}+K_{11i+1,j,k})\Delta x}(\phi_{i+1,j,k}-\phi_{i,j,k}) \quad . \tag{2-11}$$

This approximation gives rise to a five point scheme in two dimensions and a seven point scheme in three dimensions. In this work a fully implicit formulation (Aziz and Settari, 1979) is employed to solve Eq. 2-3 and is written in the locally conservative integral form:

$$\begin{aligned}
&(s_{Pi,j,k}^{n+1} - s_{Pi,j,k}^{n})\tau_{i,j,k} + \Delta t(\lambda_P(s_{Pi+1/2,j,k}^{n+1})F_{i+1/2,j,k}(\phi^{n+1}) - \lambda_P(s_{Pi-1/2,j,k}^{n+1})F_{i-1/2,j,k}(\phi^{n+1}) \\
&+ \lambda_P(s_{Pi,j+1/2,k}^{n+1})F_{i,j+1/2,k}(\phi^{n+1}) - \lambda_P(s_{Pi,j-1/2,k}^{n+1})F_{i,j-1/2,k}(\phi^{n+1}) \\
&+ \lambda_P(s_{Pi,j,k+1/2}^{n+1})F_{i,j,k+1/2}(\phi^{n+1}) - \lambda_P(s_{Pi,j,k-1/2}^{n+1})F_{i,j,k-1/2}(\phi^{n+1})) = \Delta t M_{Pi,j,k}
\end{aligned} \tag{2-12}$$

for a logically Cartesian grid where τ_i is the control volume. The system is solved with respect to the aqueous phase saturation and pressure (s_1, ϕ); the oleic phase saturation s_2 is deduced from Eq. 2-4. The hyperbolic flux contribution is upwinded according to the wave direction across each edge; e.g., at edge $(i+1/2, j, k)$ the direction is a function of $\lambda_P(s_{Pi+1/2,j,k}^{n+1})F_{i+1/2,j,k}(\phi^{n+1})$, and for a positive outward wave, $s_{Pi+1/2,j,k}^{n+1} = s_{Pi,j,k}^{n+1}$, otherwise $s_{Pi+1/2,j,k}^{n+1} = s_{Pi+1,j,k}^{n+1}$. This method is known as the single point upstream weighting scheme in reservoir simulation and is a function of four points of the seven point stencil, where the four points vary according to the local upwind direction. In this case the net fluxes of Eq. 2-12 are comprised of cell edge based quantities.

Several new schemes have been proposed and developed for full tensor simulation in recent years (e.g., Aavatsmark et al., 1997; Arbogast et al., 1997; Edwards and Rogers, 1998; Edwards, 1995, 2000; Lee et al., 1998; Verma and Aziz, 1997). These schemes all employ nine point operators for the pressure equation on logically Cartesian grids in two dimensions. In this work cell vertex/point distributed schemes are considered.

2.3.3 Two Dimensional Formulation. Finite volume discretizations will be defined with respect to grid vertex control volumes. For vertex i, j the control volume is defined by joining cell centers to the cell edge mid-points of those edges that are attached to the $(i, j)th$ vertex (see **Figs. 2-5a** and **2-5b**). As a result, each quadrilateral is subdivided into four quadrants with each quadrant forming part of the control-volume associated with the corresponding cell vertex. Consequently, each control-volume is generally comprised of a polygon. The methods presented also apply to cell centered formulations by translating the operations onto a grid that is essentially the dual mesh (Edwards and Rogers, 1998).

A systematic procedure for deriving and coding full stencil schemes is to build the fluxes in a cell-wise fashion. For a given cell $(i+1/2, j+1/2)$, a flux is calculated along the normal to each control volume face inside the cell (Figs. 2-5a and 2-5b), leading to the four fluxes

$$F_{N\,i+1/2,j+1/2} \qquad N = 1...4$$

per quadrilateral where suffices $N = 1...4$ are the local edge numbers of the quadrilateral. The fluxes are distributed to their adjacent cell edges that are intersected by the control volume faces. In this way the finite volume scheme net edge fluxes are assembled via summation of fluxes that correspond to common edges and

$$\mathsf{F}_{i+1/2,j} = F_{3i+1/2,j-1/2} + F_{1i+1/2,j+1/2} \,, \qquad (2\text{-}13)$$

$$\mathsf{F}_{i,j+1/2} = F_{2i-1/2,j+1/2} + F_{4i+1/2,j+1/2} \,.$$

For the discrete fully implicit formulation the net edge based fluxes of Eq. 2-13 are substituted directly into Eq. 2-12 to yield a block banded Jacobian with a nine node discrete operator for pressure and a five node operator for saturation, where the upwind directions are now functions of the local full tensor fluxes.

For cell-wise constant spatial coefficients a general family of nine-point full (or diagonal) tensor schemes can be defined (Edwards, 1995) where the flux takes the form

$$F_{1i+1/2,j+1/2}(\phi) = -\Big[T_{11i+1/2,j+1/2}((1-\eta)\Delta_{\xi_1}\phi_{i+1/2,j} + \eta\Delta_{\xi_1}\phi_{i+1/2,j+1}) + T_{12i+1/2,j+1/2}\frac{(\Delta_{\xi_2}\phi_{i,j+1/2} + \Delta_{\xi_2}\phi_{i+1,j+1/2})}{2}\Big]\frac{1}{2} \quad , \qquad (2\text{-}14)$$

and $\Delta_{\xi_1}\phi_{i+1/2,j} = \phi_{i+1,j} - \phi_{i,j}$, $\Delta_{\xi_2}\phi_{i,j+1/2} = \phi_{i,j+1} - \phi_{i,j}$. The family is parameterized by the quadrature point η. For discrete ellipticity, where $(T_{ab})^2 \le T_{aa}T_{bb}$ in each cell, the discrete matrix corresponding to the scheme with flux given by Eq. 2-14 is symmetric positive definite for all quadrature points η such that $0 \le \eta < 1/2$. Conditional diagonal dominance results for $\eta > 0$. Further details and properties of the schemes are presented in Edwards (1995, 1998) and Edwards and Rogers (1998).

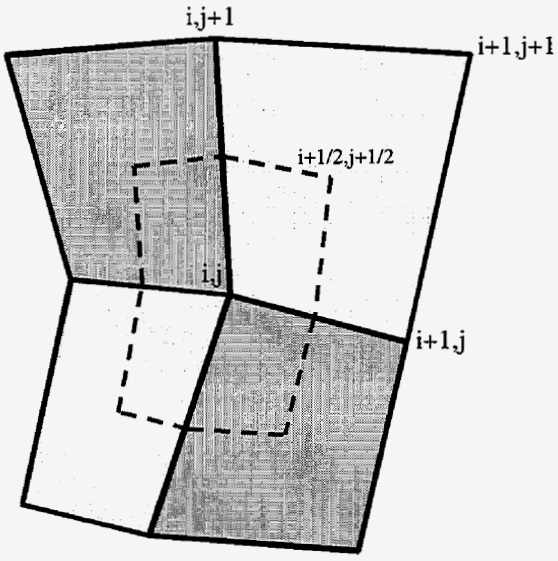

2-5a: Dashed line = surface of control-volume *i,j*

Cell vertex flow variable, Cell-wise constant tensor (shaded)

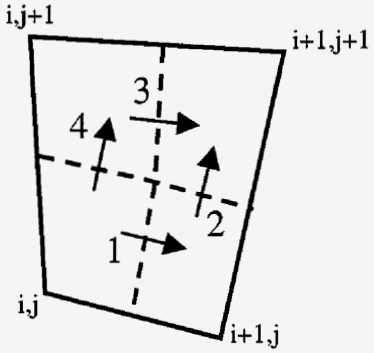

2-5b: Cell-edge flux locations 1,2,3,4

Fig. 2-5: Dual variable scheme, control-volume and flux calculation

2.3.4 Three Dimensional Hexahedral Approximations. The procedure for building full tensor schemes in three dimensions follows a similar cell-wise construction. For vertex i,j,k the control volume is defined by joining cell centers to the cell face mid-points and then joining the cell face mid-points to the cell edge mid-points (see **Fig. 2-6**). As a result, each hexahedral is subdivided into eight sub-cells, where each sub-cell is attached to a unique vertex of the hexahedra. The union of all sub-cells that share a common vertex defines the control-volume for the cell vertex scheme.

In three dimensions, 12 fluxes are defined with respect to each cell, where as in two dimensions, one flux is associated with each edge of the cell. For a given cell $(i+1/2, j+1/2, k+1/2)$, the fluxes are calculated along the normals to each of the control volume faces inside the cell, as shown in Fig. 2-6, leading to twelve fluxes

$$F_{N\,i+1/2,j+1/2,k+1/2} \qquad N=1...12$$

per hexahedral where suffices $N=1...12$ are the local edge numbers of the hexahedra. The fluxes are distributed to their adjacent cell edges and the finite volume scheme net edge fluxes are assembled via summation of fluxes that correspond to a common edge.

For a structured hexahedral mesh the net edge based flux at surface $(i+1/2, j, k)$ of the cell is given by

$$\mathsf{F}_{i+1/2,j,k} = F_{1\,i+1/2,j+1/2,k+1/2} + F_{3i+1/2,j-1/2,k+1/2} + F_{11\,i+1/2,j-1/2,k-1/2} + F_{9\,i+1/2,j+1/2,k-1/2} \quad . \text{(2-15)}$$

For a fully implicit formulation the net edge based fluxes of Eq. 2-15 are substituted directly into Eq. 2-12 and yield a block banded system with a 27 node discrete operator acting for pressure and a 7 node operator for saturation. The upwind directions are now functions of the local full tensor fluxes. Referring to edge $(i+1/2, j, k)$, the upwind direction is determined via $\lambda_P(s^{n+1}_{P\,i+1/2,j,k})\mathsf{F}_{i+1/2,j,k}(\phi^{n+1})$.

For cell-wise constant coefficients a three dimensional generalization of the

family of schemes of Eq. 2-14 is defined below where, e.g., the flux associated with edge 1 takes the form

$$F_{1i+1/2,j+1/2,k+1/2}(\phi) = -\Big[T_{11i+1/2,j+1/2,k+1/2}(((1-\eta)\Delta_{\xi_1}\phi_{i+1/2,j,k} + \eta\Delta_{\xi_1}\phi_{i+1/2,j+1,k}))(1-\zeta)$$
$$+ ((1-\eta)\Delta_{\xi_1}\phi_{i+1/2,j,k+1} + \eta\Delta_{\xi_1}\phi_{i+1/2,j+1,k+1}))\zeta) +$$
$$+ T_{12i+1/2,j+1/2,k+1/2}\left(\frac{\Delta_{\xi_2}\phi_{i,j+1/2,k} + \Delta_{\xi_2}\phi_{i+1,j+1/2,k} + \Delta_{\xi_2}\phi_{i,j+1/2,k+1} + \Delta_{\xi_2}\phi_{i+1,j+1/2,k+1}}{4}\right)$$
$$+ T_{13i+1/2,j+1/2,k+1/2}\left(\frac{\Delta_{\xi_3}\phi_{i,j,k+1/2} + \Delta_{\xi_3}\phi_{i+1,j,k+1/2} + \Delta_{\xi_3}\phi_{i,j+1,k+1/2} + \Delta_{\xi_3}\phi_{i+1,j+1,k+1/2}}{4}\right)\Big]\frac{1}{4} \tag{2-16}$$

The family is parameterized by (η,ζ), where $0 \le \eta < 1/2$ and $0 \le \zeta < 1/2$.

2.3.5 Flux Continuous Schemes. When rock and flow variables are chosen to be control-volume distributed (i.e., point distributed or cell centered), the permeability tensor can be discontinuous across the control-volume faces and flux continuity must be enforced. Flux continuous full tensor discretization operators are presented in Edwards and Rogers (1998). In two dimensions, four auxiliary continuous control-volume interface pressures are introduced per cell (**Figs. 2-7** and **2-8**) and sub-cell normal fluxes are defined (two fluxes per triangle). Equating fluxes on the left and right hand sides of each of the interfaces (*1,2,3,4*) leads to a local 4×4 linear system of equations for the four interface pressures (determined by linear combinations of the four cell vertex pressures). An equivalent scheme was developed independently by Aavatsmark et al. (1997). For a diagonal tensor the methods reduce to the standard two point flux approximation with the coefficient defined by the harmonic mean. A family of schemes is also presented in Edwards and Rogers (1998) which ensures that flux continuous approximations are obtained for both nine-point diagonal and full tensor operators. In general the local cell edge fluxes can be expressed in terms of the algebraic coefficients that are derived from the continuity conditions. The flux at edge e then takes the form

$$F_e(\phi) = -\sum_{j=1}^{Ned} \alpha_j^e \Delta_j \phi \quad , \tag{2-17}$$

where summation is over the total number of cell edges. If permeability is locally constant over the four sub control-volume elements then for an appropriate choice of flux quadrature the coefficients reduce to those of Eq. 2-14; e.g., with $e=1$,

$$\alpha_1^1 = \frac{1}{2} T_{11i+1/2,j+1/2}(1-\eta), \quad \alpha_3^1 = \frac{1}{2} T_{11i+1/2,j+1/2}\eta$$
$$\alpha_2^1 = \frac{1}{4} T_{12i+1/2,j+1/2}, \quad \alpha_4^1 = \frac{1}{4} T_{11i+1/2,j+1/2} \tag{2-18}$$

The generalization of flux continuous schemes to three dimensions involves the introduction of 12 auxiliary interface pressures that are eliminated via local flux continuity conditions in an analogous procedure to that described by Aavatsmark et al. (1997). Development of these schemes is currently being considered for general structured and unstructured three dimensional grids.

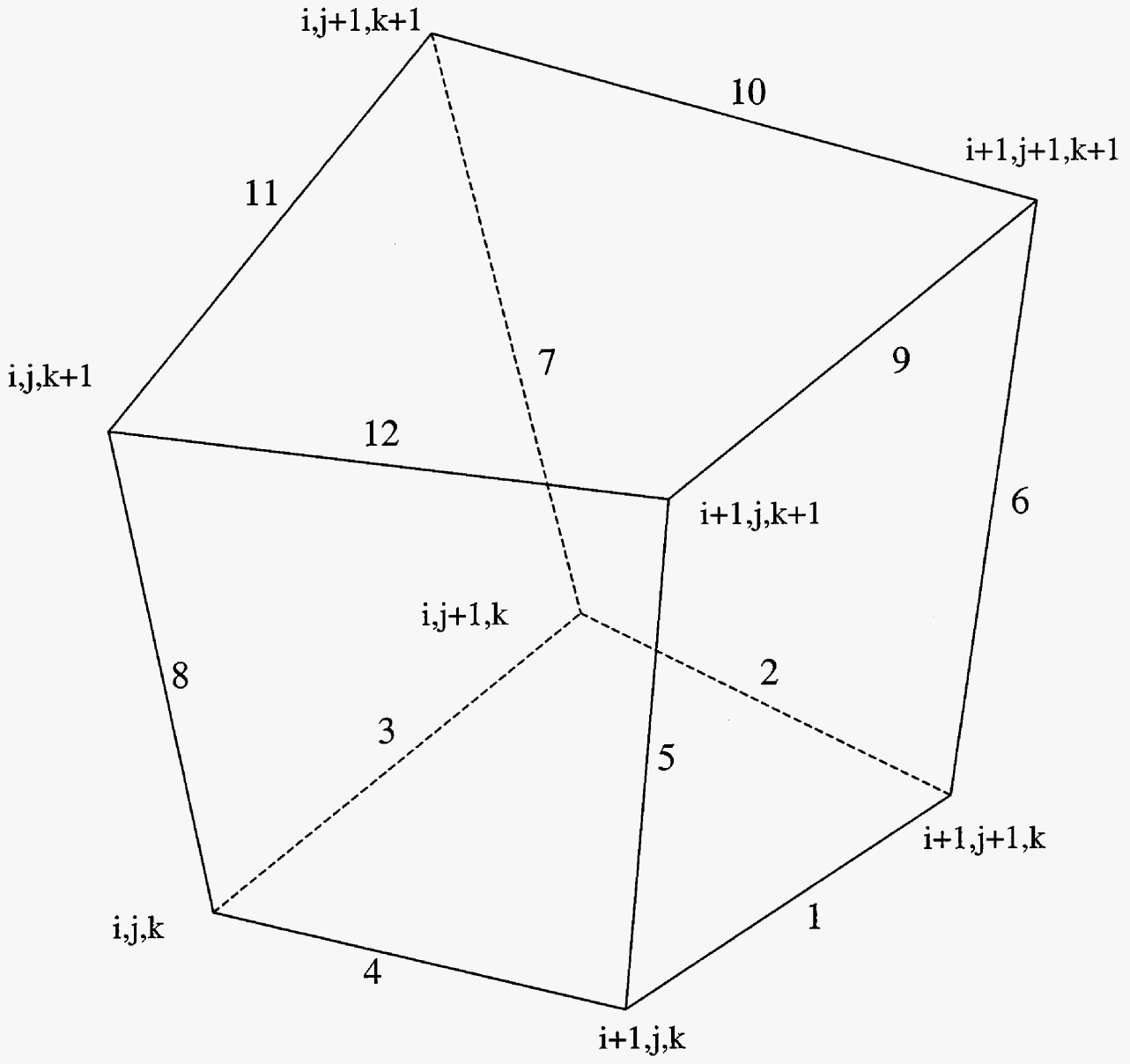

Fig. 2-6: Hexahedral cell vertex indicies and local cell edge numbers

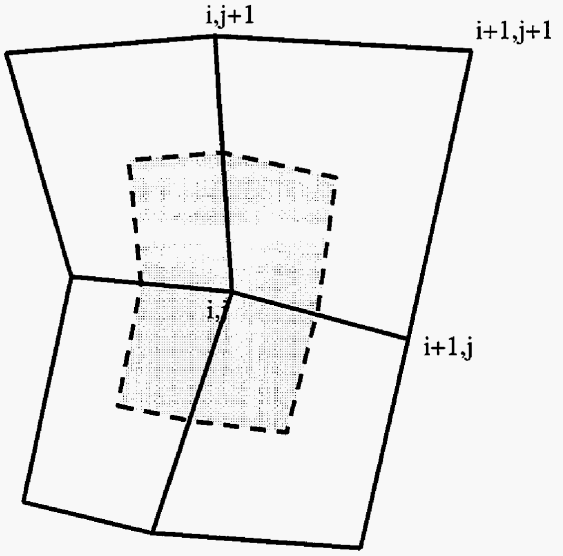

2-7a: Dashed line = surface of control-volume *i,j*

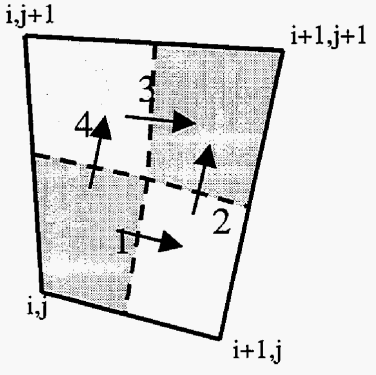

2-7b: Cell-wise fluxes N,S,E,W

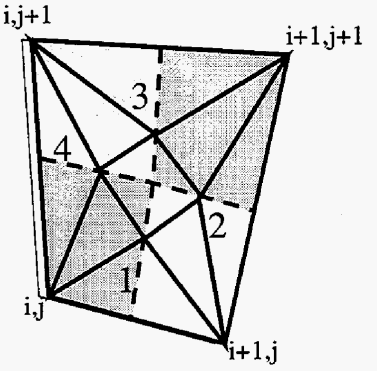

2-7c: Sub-cell triangle basis for flux continuity

Cell vertex flow variable, constant tensor per control-volume (shaded)

Fig. 2-7: Control-volume distributed scheme, control-volume and flux calculation

2.3.6 Split Tensor Flux on a Structured Grid. In the previous section discrete full tensor operators were introduced which increase the stencil size and thus the bandwidth of the Jacobian matrix from 7 to 27 row entries in three dimensions. While the above approximations of the full tensor pressure equation are symmetric positive definite, they are also conditionally diagonally dominant (Edwards and Rogers, 1998). When coupled with the non-symmetric diagonally dominant upwind approximation for the essentially hyperbolic phase equations, the resulting enlarged block Jacobian of the fully implicit full tensor system of Eqs. 2-15 and 2-12 is neither symmetric positive definite nor diagonally dominant. This is in contrast to the standard diagonal tensor fully implicit formulation, which maintains a smaller Jacobian bandwidth and an underlying diagonal dominance.

Motivated by the above observations the aim here is to develop a consistent scheme for multiphase flow with a full tensor velocity field that maintains the benefits of a fully implicit formulation while only requiring inversion of the standard seven-point Jacobian matrix of the system. This development extends the two dimensional deferred correction (Edwards, 1998) and split operator semi-implicit formulations (Edwards, 2000) to a fully implicit formulation in three dimensions. On a logically rectangular grid the essence of the approach involves calculating the seven point operator (arising from two-point flux assembly) at the new time level $n+1$ while the remainder terms are calculated at the old time level n, resulting in a reduced Jacobian matrix of standard size.

A split time level discretization operator can be defined for general tensor schemes by splitting at the flux level (Edwards, 2000). Flux splitting enables semi-implicit schemes to be defined for evolutionary problems that avoid the additional iterations that would otherwise be required by splitting at the matrix level, while maintaining local conservation, consistency and stability of the formulation (Edwards, 2000). The split flux is defined by approximating the full stencil flux at the old time level and adding the leading two point flux at the new time level while subtracting the two point flux at the old time level. The general split flux takes the form

$$F^{S}_{N_{i+1/2,j+1/2,k+1/2}}(\phi^{n+1},\phi^{n}) = F^{2P}_{N_{i+1/2,j+1/2,k+1/2}}(\phi^{n+1}) + F_{N_{i+1/2,j+1/2,k+1/2}}(\phi^{n}) - F^{2P}_{N_{i+1/2,j+1/2,k+1/2}}(\phi^{n}) \quad N=1,...12 \tag{2-19}$$

Referring to the fluxes of Eqs. 2-17 and 2-18, the two-point flux contribution from cell $i+1/2, j+1/2, k+1/2$ can be written as

$$F^{2P}_{1_{i+1/2,j+1/2,k+1/2}}(\phi) = -\mathsf{T}_1^{2P}\Delta_{\xi_1}\phi_{i+1/2,j,k} \ ,$$

where $\mathsf{T}_1^{2P} = \alpha_1^1 + \alpha_3^1$ in two dimensions and $\mathsf{T}_1^{2P} = \alpha_1^1 + \alpha_4^1 + \alpha_9^1 + \alpha_{11}^1$ in three dimensions, and is proportional to a harmonic approximation of the general tensor coefficient T_{11}; c.f. Eqs. 2-17 and 2-18. The single phase split edge based flux at $(i+1/2, j, k)$ is given by

$$\mathsf{F}^{S}_{i+1/2,j,k}(\phi^{n+1},\phi^{n}) = F^{S}_{1_{i+1/2,j+1/2,k+1/2}}(\phi^{n+1},\phi^{n}) + F^{S}_{3_{i+1/2,j-1/2,k+1/2}}(\phi^{n+1},\phi^{n}) + F^{S}_{11_{i+1/2,j-1/2,k-1/2}}(\phi^{n+1},\phi^{n}) + F^{S}_{9_{i+1/2,j+1/2,k-1/2}}(\phi^{n+1},\phi^{n}) \ . \tag{2-20}$$

A semi implicit formulation for multiphase flow is obtained by replacing each of the fluxes in Eq. 2-12 with edge based time split fluxes. The upwind direction at edge $(i+1/2, j, k)$ is now determined via $\lambda_P(s^{n+1}_{P_{i+1/2,j,k}})\mathsf{F}^{S}_{i+1/2,j,k}(\phi^{n+1},\phi^{n})$. In the computations performed here the previous time level solution is used on the right hand side. Thus the method effectively recovers the full tensor solution from the diagonal tensor solution. By using the consistent split time level flux (with respect to pressure) diagonal dominance is gained and the Jacobian to be inverted always retains an underlying M-matrix with standard minimal band width (seven-point) structure. A possible alternative strategy is to perform a fully implicit inexact Newton iteration using the Jacobian assembled from the two-point fluxes as the driver. The scheme could then be used semi-implicitly or in an inner iterative loop such as deferred correction (Edwards, 1998). Further discussion on splitting strategies and types of iteration is given in Edwards (2000).

The leading discretization error due to the split operator can be shown to be $O(\Delta t)$. This has been confirmed with computed convergence rates (Edwards, 2000). Stability of the split scheme is also proven in Edwards (2000) for the case of constant elliptic coefficients.

2.3.7 Unstructured Grids. A semi-implicit split finite volume formulation (Edwards, 2000) for solving Eq. 2-3 on a structured or unstructured grid can be written in the general locally conservative integral form

$$(s_{Pi}^{n+1} - s_{Pi}^{n})\tau_i + \Delta t \sum_{k=1}^{Nedge} \lambda_P(s_{Pe(k,i)}^{n+1}) F_{e(k,i)}^{S}(\Phi^{n+1}, \Phi^{n}) = \Delta t M_{Pi} \ ,$$

where summation is over all edges $e(k,i)$ passing through the *ith* grid vertex. The net edge based flux is now comprised of all adjacent (conforming) cell edge fluxes including local grid cells of different type (e.g. triangle and/or quadrilateral cells in 2-D). As before, cell edge saturations are upwinded, the upstream direction being a function of the local net edge flux.

2.4 Simulation Results

In the results below, saturation contour plots are used to illustrate the differences between the various numerical procedures. The advantage of mixed structured-unstructured grids is demonstrated for a two dimensional problem involving a fault crossed by a high permeability streak with pinchouts as shown in **Figs. 2-8a** and **2-8b**. The geometry of the problem is faithfully represented by the grid of Fig 2-8b. The boundary conditions are those of the standard quarter five spot problem, with an injector at the bottom left corner and a producer in the upper right corner. The strong effects of the complex heterogeneity are clearly evident in the solution (**Fig. 2-8d**), which contrasts with **Fig. 2-8c**, computed on the same grid and at the same time (0.5 PVI) for a homogeneous (constant) permeability field. The split operator solution (**Fig. 2-8e**), compares favorably with full matrix inversion while reducing computation time substantially. This illustrates the benefit of the new method on general grids in two dimensions.

The next case involves a three dimensional non-K-orthogonal hexahedral grid with a resolution of only 5×5×9 nodes (**Fig. 2-9a**). An injector and producer are placed at the near bottom left and far upper right hand corners of a square domain. A homogeneous full Cartesian tensor is imposed on the domain with maximum principal component aligned with the maximum flow gradient of the problem. In this case both the grid and the Cartesian tensor contribute strong cross flow effects.

Standard simulators only allow diagonal tensor coefficients and include geometry effects by modifying these coefficients via so-called transmissibility modifiers. The saturation field computed by a standard implicit scheme with diagonal tensor (corner-point) geometry is shown in **Fig. 2-9b**. In contrast, the results computed with the full tensor schemes, using either full matrix inversion (**Fig. 2-9c**) or the split tensor operator (**Fig. 2-9d**), are in excellent agreement and clearly capture the elongated shock front caused by the dominant principal permeability tensor component. There is a large discrepancy between the results, due to the $O(1)$ error in flux that is incurred when using the diagonal tensor on a non-K-orthogonal grid. This problem illustrates the importance of full tensor computation in three dimensions. The split-flux operator reduces the computation time by nearly a factor of two when compared with the full tensor, full Jacobian matrix inverse computation, while obtaining a comparable result.

The last test case illustrates the methods on unstructured hexahedral grids. The reservoir consists of a rectangular box shaped domain with a horizontal injector and producer inserted in the middle of the left and right hand side faces of the domain (**Fig. 2-10a**). The Cartesian permeability tensor is isotropic and constant throughout the reservoir.

An unstructured hexahedral grid is now used to model the problem (**Fig. 2-10b**). A planar cross section of the grid is shown in Fig. 2-4. The saturation field computed by a standard implicit scheme with a two point flux and diagonal tensor geometry is shown in **Fig. 2-10c**. The effect of the $O(1)$ error in flux is severe in this case, resulting in a complete buckling of the shock front. The discrepancy in results is entirely due to non-orthogonal grid effects as the Cartesian tensor is isotropic. In contrast, the results computed with the full tensor schemes, using either full matrix inversion (**Fig. 2-10d**) or

the split tensor operator (**Fig. 2-10e**), are again in excellent agreement and clearly remove the predominant error caused by the standard two-point flux approximation. This problem illustrates the importance of full tensor computation in three dimensions on unstructured grids. The split-flux operator again reduces the computation time by a factor of two when compared with the full tensor, full Jacobian matrix inverse computation.

2.5 Future Directions

Currently the reservoir domain can be decomposed into a structured or unstructured set of subdomains where each subdomain grid is structured (logically Cartesian) with a continuous logical coordinate density between subdomains. Future work will include the development of interface regions that will allow a discontinuous change in logical coordinate density so that locally unstructured grids can be introduced when necessary; e.g., at faults, pinchouts or when increasing local grid resolution by local grid refinement. A two dimensional example involving faults and pinchouts was presented which demonstrates the advantages of mixed grids for more complex reservoir problems. In two dimensions there are only two cell types (quadrilaterals and triangles) and the interface between cell types is relatively unambiguous. In 3-D there are four cell types, namely hexahedra, tetrahedra, prisms and pyramids, as shown in **Fig. 2-11**. An interface between a structured hexahedral grid and an unstructured grid can take many different forms in three dimensions and can be comprised of all four cell types. Interfaces will be explored and discretization schemes for all of the cell types will be developed. Operator splitting will also continue to be studied and developed for general grids.

Flow based gridding will also be developed along with appropriate well modules. A robust upscaling technique is an important ingredient here, as the flow based grids can differ significantly from an underlying geological grid. Upscaling to general grid blocks and cell shapes will be an important aspect of this project. Large sensitivities in flow results have been observed when using different upscaling algorithms on curvilinear grids (Castellini et al., 2000) and serve to emphasize the importance of upscaling when developing general gridding techniques. Currently, state of the art flow response based upscaling algorithms, even with simple pressure-flux or periodic boundary conditions,

cannot be applied directly. The main difficulty here is that flow based grids do not generally conform to their underlying geological grids and therefore a consistent flow response upscaling technique involves development of appropriate fine to coarse grid operators. Techniques to address this problem are currently under development in two dimensions (He, 2000; Wen et al., 2000). The extension to three dimensions will be performed in a future project. We anticipate further scope for improvement in flow resolution when a more robust and general coarse grid to fine grid three dimensional upscaling algorithm is available.

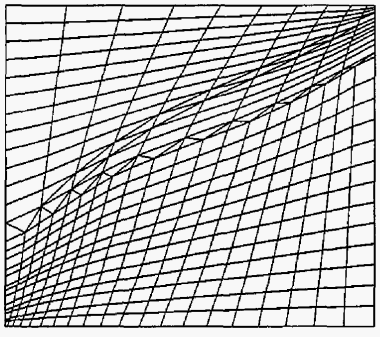

2-8a: Unstructured grid

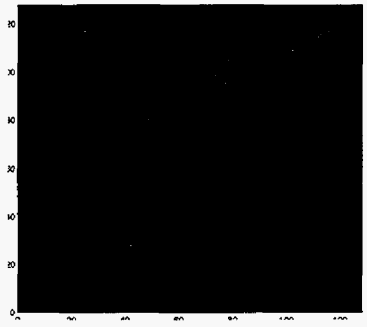

2-8b: Unstructured grid and heterogeneity

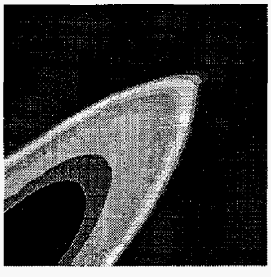

2-8c: Homogeneous

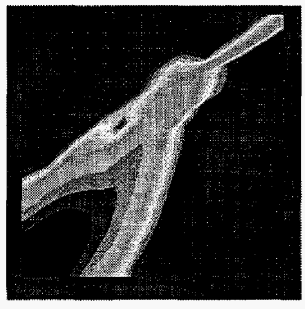

2-8d: Full tensor full matrix inverse

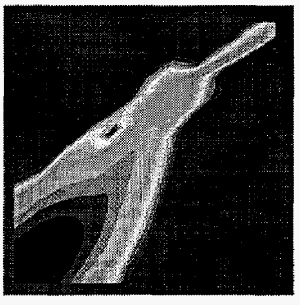

2-8e: Full tensor - split flux

Fig. 2-8: Fault crossed by a high permeability streak with pinchouts

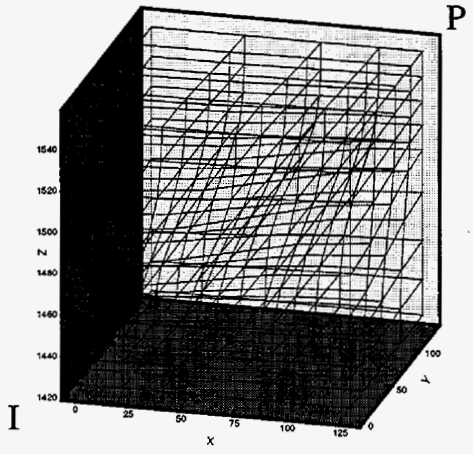

2-9a: Non-orthogonal grid

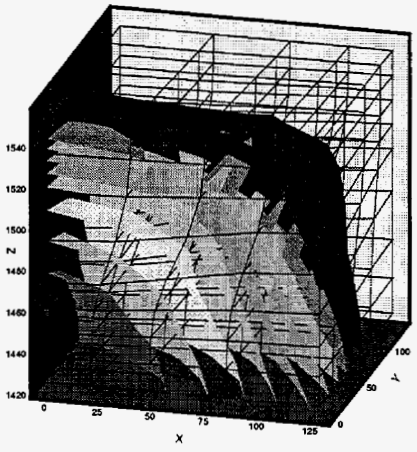

2-9b: Diagonal tensor
fully implicit

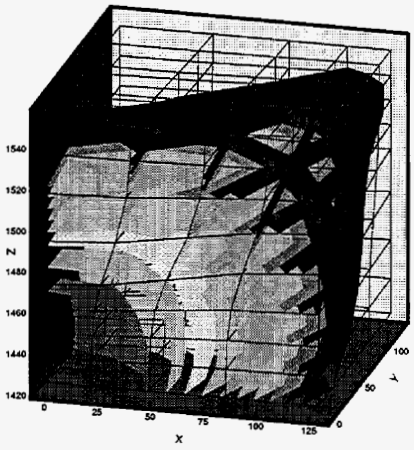

2-9c: Full tensor, full matrix inverse
fully implicit

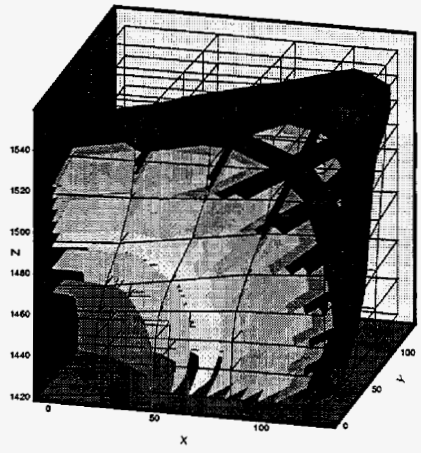

9d:Full Tensor, Split Flux
Semi-Implicit

Fig. 2-9: Structured non-orthogonal hexahedral grid with full Cartesian tensor

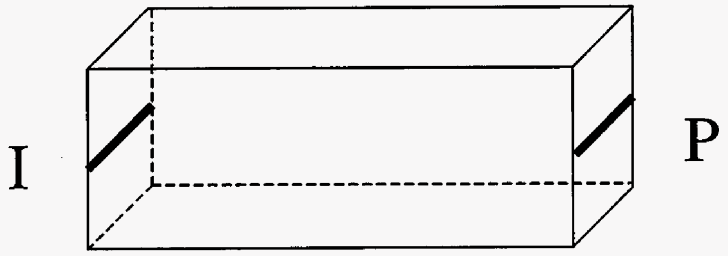

2-10a: Horizontal injection and production

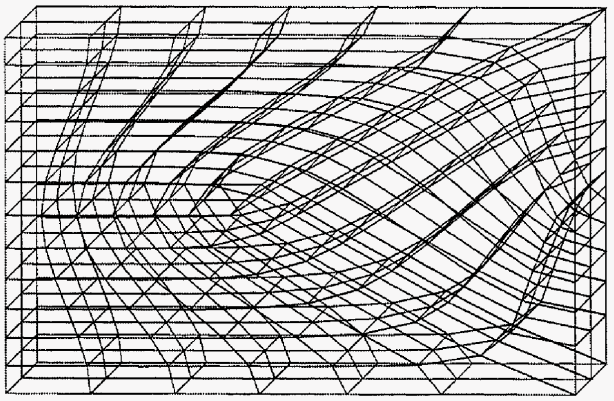

2-10b: Unstructured multiblock grid

Fig. 2-10: Unstructured hexahedral grid and horizontal injector and producer

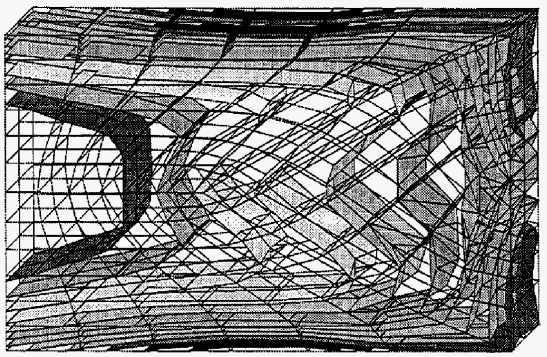

2-10c: Diagonal tensor (2-point flux) solution

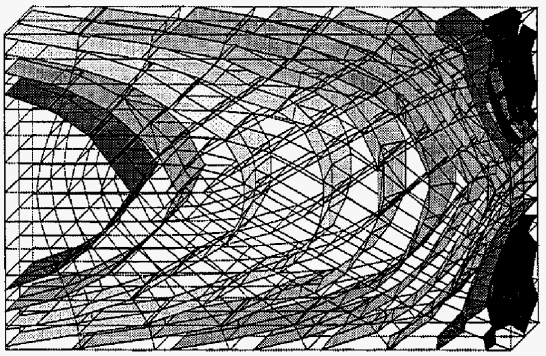

2-10c: Full tensor (full matrix inverse) solution

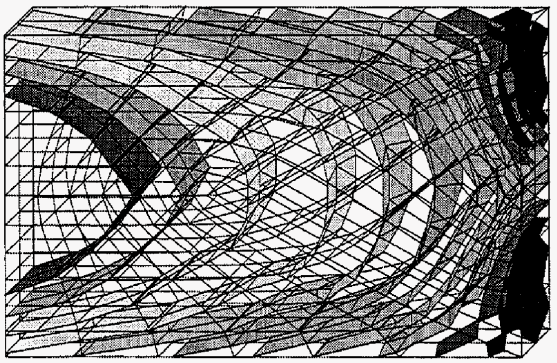

2-10e: Full tensor (split flux) solution

Fig. 2-10: Unstructured hexahedral grid and horizontal injector and producer - (continued)

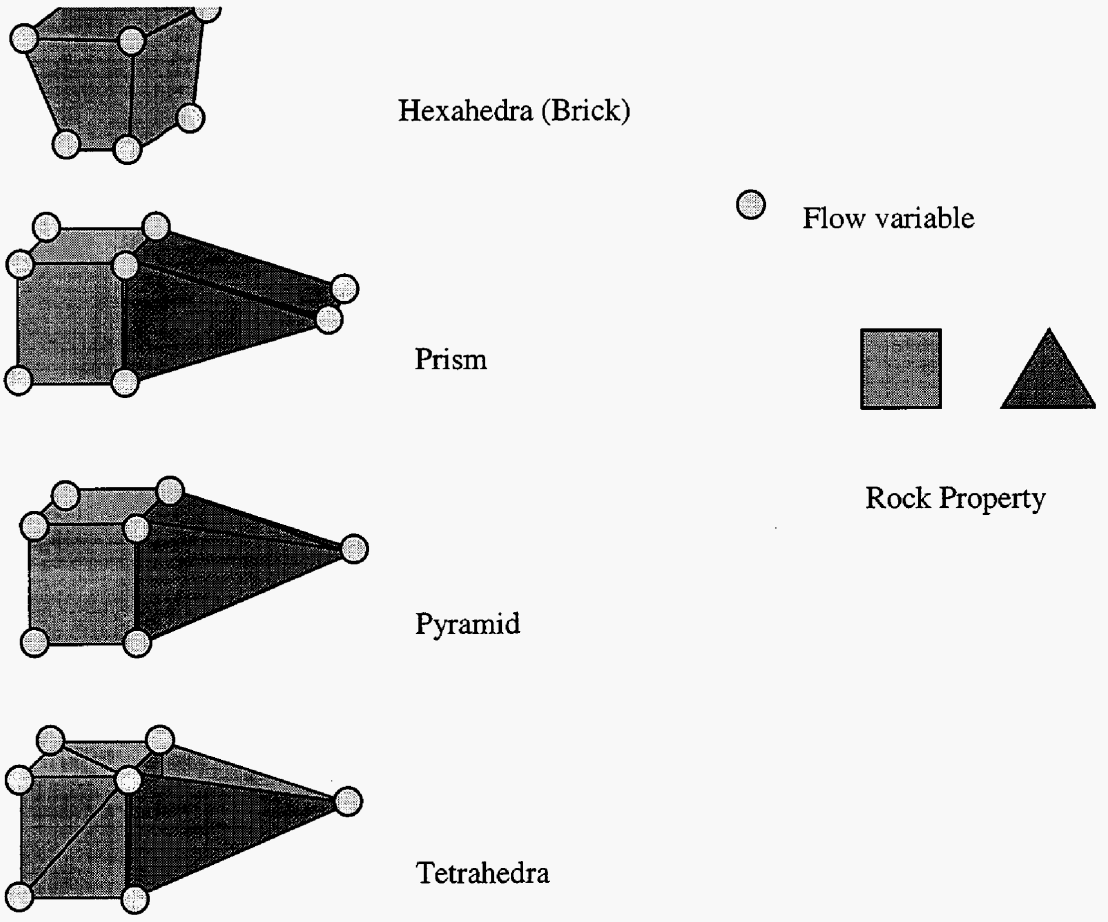

Fig. 2-11: Structured - unstructured grid cell interfaces
Disretization schemes (future work)

2.6 References

Aavatsmark, I., Barkve, T. and Mannseth, T.: "Control-Volume Discretization Methods for 3D Quadrilateral Grids in Inhomogeneous, Anisotropic Reservoirs," paper SPE 38229 presented at the 1997 SPE Symposium on Reservoir Simulation, Dallas, Texas, June 8-11.

Arbogast, T., Wheeler, M.F. and Yotov, I.: "Mixed Finite Elements for Elliptic Problems with Tensor Coefficients as Cell centered Finite Differences," *SIAM Numer. Anal.*, **34**, 828-852, 1997.

Arbogast, T., Keenan, P., Wheeler, M.F. and Yotov, I.: "Logically Rectangular Mixed Methods for Darcy Flow on General Geometry" paper SPE 29099 presented at the 1995 SPE Symposium on Reservoir Simulation, San Antonio, Texas, Feb. 12-15.

Aziz, K. and Settari, A.: *Petroleum Reservoir Simulation,* Applied Science Publishers, London, 1979.

Castellini, A., Edwards, M.G. and Durlofsky, L.J.: "Flow Based Modules for Grid Generation in Two and Three Dimensions," Proceedings of the 7th European Conference on the Mathematics of Oil Recovery, Baveno, Italy, Sept. 5-8, 2000.

Durlofsky, L.J., Jones, R.C., and Milliken, W.J.: "A Nonuniform Coarsening Approach for the Scale Up of Displacement Processes in Heterogeneous Porous Media," *Adv. Water Res.*, **20**, 335-347, 1997.

Edwards, M.G.: "Symmetric, Flux Continuous, Positive Definite Approximation of the Elliptic Full Tensor Pressure Equation in Local Conservation Form," paper SPE 29147 presented at the 1995 SPE Symposium on Reservoir Simulation, San Antonio, Texas, Feb. 12-15.

Edwards, M.G "Cross-Flow, Tensors and Finite Volume Approximation with Deferred Correction," *Comput. Methods Appl. Mech. Engrg.*, **151**, 143 – 161, 1998.

Edwards, M.G. and Rogers, C.F.: "Finite Volume Discretization with Imposed Flux Continuity for the General Tensor Pressure Equation," *Comp. Geosciences,* **2**, 259-290, 1998.

Edwards, M.G., Agut, R. and Aziz, K.: "Quasi K-Orthogonal Streamline Grids, Gridding and Discretization," paper SPE 49072 presented at the 1998 SPE Annual Technical Conference and Exhibition, New Orleans, Sept 28 – 30, 1998.

Edwards, M.G. "Split Tensor Discretization Operators Coupled with Quasi K-Orthogonal Grids," paper SPE 51903 presented at the 1999 SPE Symposium on Reservoir Simulation, Houston, Texas, Feb. 14-17.

Edwards, M.G., Li, B. and Aziz, K.: "Modular Mesh Generation with Embedded Streamline-Potential Grids." paper SPE 51911 presented at the 1999 SPE Symposium on Reservoir Simulation, Houston, Texas, Feb. 14-17.

Edwards, M.G.: "M-matrix Flux Splitting for General Full Tensor Discretization Operators on Structured and Unstructured Grids," *J. Comp. Phys.* **160**, 1-28, 2000.

Gordon, W.J. and Hall, C.A.: "Construction of Curvilinear Co-ordinate Systems and Applications to Mesh Generation," *Int. J. for Num. Methods in Eng.*, **7**, 461-477, 1973.

He, C.: "Upscaling to General Quadrilateral Grids," Master's report, Stanford University, June 2000.

Lee, S.H., Durlofsky, L.J., Lough, M.F. and Chen, W.H.: "Finite Difference Simulation of Geologically Complex Reservoirs with Tensor Permeabilities," *SPERE&E*, 567-574, Dec. 1998.

Portella, R.C.M. and Hewett, T.A.: "Upscaling, Gridding, and Simulation Using Streamtubes," paper 49071 presented at the 1998 SPE Annual Technical Conference and Exhibition, New Orleans, Sept. 27-30, 1998.

Thompson, J.F., Warsi, Z.U.A. and Mastin, C.W.: *Numerical Grid Generation*, North-Holland, New York, 483 p, 1985.

Tran, T.T.B: "Stochastic Simulation of Permeability Fields and Their Scale-Up for Flow Modeling", PhD Thesis, Stanford University, 1995.

Verma, S. and Aziz, K. "A Control Volume Scheme for Flexible Grids in Reservoir Simulation," paper SPE 37999 presented at the 1997 SPE Symposium on Reservoir Simulation, Dallas, Texas, June 8-11, 1997.

Wen, X.-H., Durlofsky, L.J., Lee, S.H. and Edwards, M.G.: "Full Tensor Upscaling of Geologically Complex Reservoir Descriptions," paper SPE 62928, to be presented at the 2000 SPE Annual Technical Conference and Exhibition, Dallas, Oct. 1-4.

Part II. Coupling of the Reservoir and Non-Conventional Wells in Simulators

As discussed in Chapter 1, existing approaches for coupling the well to the reservoir may lose accuracy in problems involving non-conventional wells. The well is coupled to the reservoir through the well index, which is closely related to the productivity index, commonly used in reservoir engineering analyses. The calculation of productivity index for non-conventional wells is considered in detail in Chapter 3. New semi-analytical methods based on Green's functions, capable of approximating the effects of reservoir heterogeneity and wellbore flow, are presented. The extension of these methods for the calculation of well index is discussed. Much of the work described in this chapter was presented in papers by Durlofsky (2000) and Wolsteiner et al. (2000a, 2000b).

Modeling of flow in the wellbore itself, which is generally not necessary in the case of vertical wells, can be important in non-conventional wells. This is because pressure losses can be much more substantial in the case of non-conventional wells due to their much greater length. Calculation of pressure losses in the wellbore is complicated because there is inflow along the well (due to production) and because the flow often involves more than a single phase. In Chapter 4 we present models for wellbore pressure loss that account for the effects of wellbore friction and acceleration. New correlations, capable of modeling data from a variety of experimental systems, are presented for single phase flow. Extension of these correlations for multiphase flow will be the subject of future work.

3 Semi-Analytical Calculation of Productivity Index and Well Index

by Christian Wolfsteiner, Louis J. Durlofsky and Khalid Aziz

In reservoir simulation models, the wellbore is not modeled explicitly but is rather linked to the reservoir through use of a so-called well model. Well models, such as those due to Peaceman (1983), represent the well production (or injection) from grid block i,j,k in

terms of a well index (WI), the wellbore pressure (p_{wb}) and the pressure of the grid block ($p_{i,j,k}$) via:

$$q_{i,j,k} = WI(p_{wb} - p_{i,j,k}) \quad , \tag{3-1}$$

where $q_{i,j,k}$ represents the flow rate from the well into block (i,j,k). The form of Eq. 3-1 is very similar to the general expression for well productivity index (PI):

$$q = PI(p_{wb} - < p >) \quad , \tag{3-2}$$

where q is now total well production and $<p>$ is the average reservoir pressure. The similarity between Eqs. 3-1 and 3-2 illustrates why techniques developed for the calculation of PI can also be applied to the calculation of WI. Thus, though our emphasis here will be on the development and application of efficient semi-analytical approaches for the calculation of PI for non-conventional wells, these techniques also lend themselves to the calculation of WI. The detailed calculation and application of well indexes for complex non-conventional wells will be the subject of our future work.

One approach for determining the well productivity is to simulate the reservoir performance using a finite difference simulator. This is the most rigorous approach available, though it is also the most demanding in terms of time and data requirements. An alternate approach for modeling the productivity of non-conventional wells operating under primary production is to employ a semi-analytical solution technique. Early work along these lines included single horizontal wells (of infinite conductivity) aligned parallel to one side of a box shaped reservoir. Solution methods were successive integral transforms (Goode and Thambynayagam, 1987; Kuchuk et al., 1990) and the use of instantaneous Green's functions (Daviau et al., 1985; Clonts and Ramey, 1986; Ozkan et al., 1989; Babu and Odeh, 1989), resulting in infinite series expressions. More complex geometries were considered later (Economides et al., 1996; Maizeret, 1996; Ouyang, 1998) as numerical integration became more feasible. A number of works (see Ouyang (1998) and citations therein) include coupling of wellbore hydraulics (i.e., finite conductivity wells) with reservoir flow. The method we apply in this study is that of Ouyang (1998).

All of the semi-analytical techniques mentioned above have the advantage of limited data requirements and high degrees of computational efficiency. These techniques are, however, limited to homogeneous systems or at most strictly layered systems (Lee and Milliken, 1993; Basquet et al., 1998). This represents a substantial limitation because the productivity of non-conventional wells can be significantly impacted by fine scale heterogeneities in the near-well region. Fine scale heterogeneity can be incorporated into detailed simulation models, though the resulting models are complex to build and require substantial computation time to run.

In this work we extend an existing semi-analytical approach to approximately account for heterogeneity in the near-well region. This enables us to apply the semi-analytical approach to more realistic heterogeneous systems. We accomplish this by introducing an effective skin s into the semi-analytical model and then estimating this effective skin as a function of position along the wellbore. The skin is computed via local, weighted integrations of the permeability field in the near-well region. This skin differs significantly from skin in the usual sense, as it is here due to intrinsic heterogeneity in the permeability field rather than from formation damage or stimulation. Away from the wellbore, the reservoir is modeled in terms of the large-scale effective permeability, $\mathbf{k}^*$. The overall method is highly efficient and approximates both near-well effects (through s) and global effects (through $\mathbf{k}^*$) with reasonable accuracy.

The approach presented here combines and extends formulations developed in two separate earlier studies. These studies addressed the development of a semi-analytical well model (Ouyang, 1998) and the approximation of the effects of heterogeneity in the region near a vertical well (Durlofsky, 2000). The semi-analytical well model is applicable for very general well configurations and also accounts for pressure drop in the wellbore due to friction, gravitational and acceleration effects. These can be important in long horizontal wells.

The approximate heterogeneity model applied here was originally developed for the modeling of vertical wells in heterogeneous, two dimensional areal systems. Both single well and two well systems were considered. The basic approach was shown to provide accurate estimates for well productivity, relative to fine grid simulation results,

for many geostatistical realizations over a range of geostatistical parameters (Durlofsky, 2000). As will be shown below, our new method successfully builds upon both the semi-analytical well model and the approximate heterogeneity model.

Another technique for approximately modeling the effects of heterogeneity on horizontal wells was previously developed by Brekke and Thompson (1996). This method, based on a network modeling type of approach, differs considerably from the procedure presented here in that our methodology has as its basis a semi-analytical solution technique. The earlier method does, however, display accurate results for a range of problems similar to those considered here.

In this chapter we first describe the overall method in detail. Then, we present numerical results for horizontal and multilateral wells in heterogeneous three dimensional systems. These results are in many cases compared with detailed finite difference calculations to assess their level of accuracy. Our new description is shown to provide an accurate estimate of production rate, as a function of position along the wellbore, for a variety of well configurations and for different heterogeneous permeability fields.

Next, we apply our general semi-analytical method to an investigation of the combined effects of reservoir heterogeneity and wellbore hydraulics on the productivity of non-conventional wells. We consider multiple realizations of permeability fields of prescribed statistics and compute the productivity of the well in each case. For each realization, we compute the well productivity both with and without the effects of wellbore hydraulics included. We then determine the (ensemble) average and the variation in well performance and also gauge the impact of wellbore hydraulics on well productivity. We additionally compare the ensemble-averaged productivity with the productivity computed using an "average" homogeneous reservoir description. We show that the productivity of the averaged reservoir description generally deviates somewhat from the ensemble-averaged productivity. However, we find that the averaged reservoir description is quite useful for determining the magnitude of the effect of the wellbore hydraulics.

3.1 Semi-Analytical Solution Technique

The basic semi-analytical approach we employ for the solution of the coupled wellbore-reservoir problem is described in detail by Ouyang and Aziz (1998). The reservoir is modeled as a parallelepiped with any combination of constant potential or no-flow boundary conditions on the six bounding faces. Isothermal flow in the reservoir is described by the single phase pressure equation for slightly compressible flow, with proper initial and boundary conditions,

$$\nabla \cdot (\mathbf{k} \cdot \nabla \Phi) = \phi \mu c_t \frac{\partial \Phi}{\partial t} \quad . \tag{3-3}$$

Equation 3-3 is formulated using potential $\Phi = p + (g/g_c)\rho z$ rather than pressure p to account for gravity effects, which can be significant. The permeability **k** is assumed to be a diagonal tensor. In the actual numerical solution, the problem is rescaled to the isotropic equivalent.

Wells can have an arbitrary configuration and trajectory (see **Fig. 3-1**). Each well i_W (of a total of n_W wells) can have $n_L(i_W)$ laterals which in turn consist of $n_S(i_W, i_L)$ segments. The total number of segments N_S is then given by

$$N_S = \sum_{i_W=1}^{n_W} \sum_{i_L=1}^{n_L(i_W)} n_S(i_W, i_L) \, . \tag{3-4}$$

The inner boundary condition is either constant rate or constant pressure for each individual well. The basic method, as previously implemented, does not account for skin.

Wellbore hydraulics are also included in the model. For the flow of a single phase liquid in a wellbore, the wellbore pressure gradient consists in general of frictional, gravitational and accelerational contributions. Employing the potential we can suppress the gravitational term; this now lets us express the potential gradient in the wellbore as

$$\frac{d\Phi}{d\xi} = \left(\frac{d\Phi}{d\xi}\right)_f + \left(\frac{d\Phi}{d\xi}\right)_a \quad , \tag{3-5}$$

where ξ designates the coordinate along the wellbore. The last term in Eq. (3-5) is due to wellbore inflow and fluid expansion. Detailed correlations for calculation of these terms are provided by Ouyang (1998).

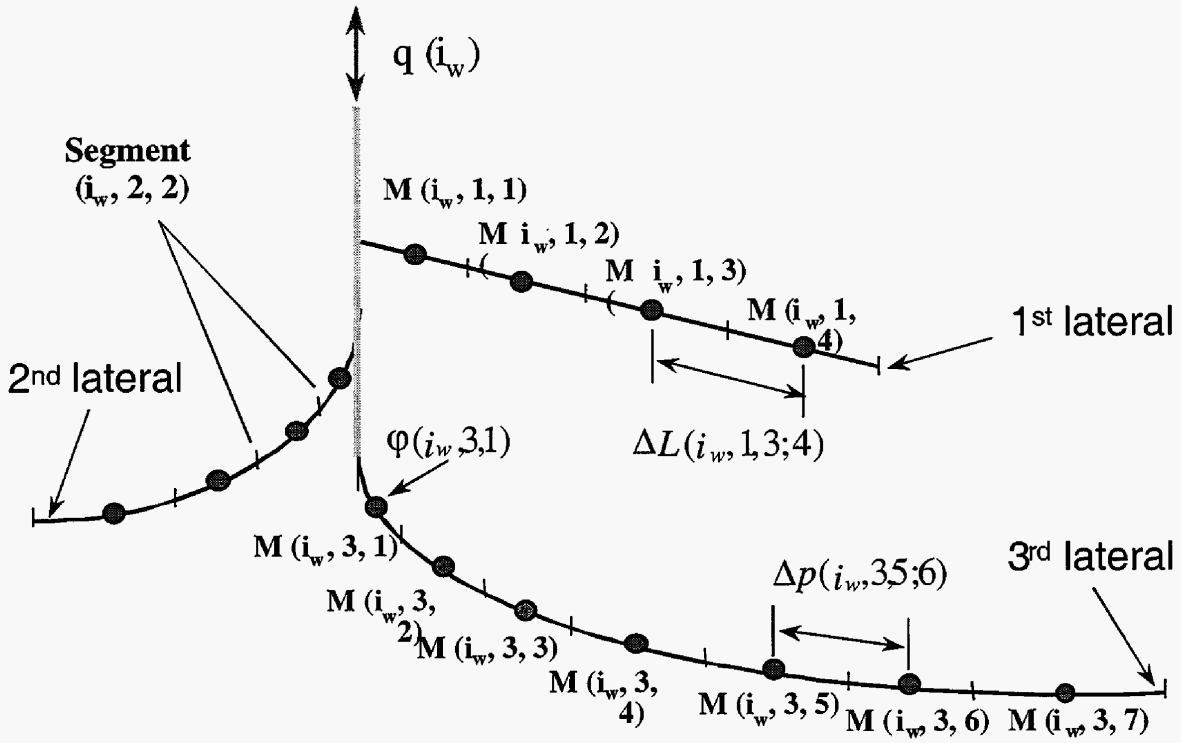

Fig. 3-1: Arbitrary well configuration (see Ouyang and Aziz, 1998)

The frictional pressure loss is expressed in dimensionless form via the friction factor f. Many correlations exist for f for closed pipe (no influx); these require some modification for the general case with influx. For the case of turbulent flow with influx (producing well), we apply the following correlation, developed by Ouyang et al. (1998),

$$f = f_0\left(1 - 0.0153 Re_w^{0.3978}\right) , \tag{3-6}$$

where f_0 is the friction factor in the absence of wall influx and Re_w is the wall Reynolds number (Reynolds number based on influx). The friction factor f_0 depends only on the axial Reynolds number and the pipe roughness and is available from standard correla-

tions. Note that the frictional pressure losses in wellbores with influx are less than those in closed pipe (evident from the minus sign in Eq. 3-6). However, because of the accelerational pressure losses, the total pressure drop is higher in the case with influx. We note also that different correlations for f are required if the flow is laminar or if the well is an injector rather than a producer (Ouyang et al., 1998).

The method of solution for this coupled reservoir-well problem is referred to as *Instantaneous Point Source/Sink Solution* (Economides et al., 1996; Maizeret, 1996; Ouyang, 1998). We solve for the dimensionless potential drawdown Φ_D in any point M of the bounded reservoir given an arbitrarily oriented well sink/source segment S. The approach entails the use of Green's functions, with superposition of image wells, application of Neumann's product rule (Gringarten and Ramey, 1973) and integration over space and time.

Free-space Green's functions for instantaneous sinks/sources satisfying Eq. 3-3 in one dimension are well known (Carslaw and Jaeger, 1959). An infinite series of image sinks/sources is superimposed to model a sink/source point between two boundaries, each with either constant pressure or no-flow boundary conditions. As an example for the case of no-flow boundaries at dimensionless locations 0 and 1, the potential drawdown at point x at time t caused by the instantaneous source with unit strength at x_0 and initial time is given by

$$\begin{aligned}\psi_x(x,x_0,t) &= 1+2\sum_{k=1}^{\infty}\exp(-k^2\pi^2 t)\cos k\pi x\cos k\pi x_0 \\ &= \frac{1}{(4\pi t)^{1/2}}\sum_{k=-\infty}^{k=\infty}\left[\exp\left(-(x-2k-x_0)^2/4t\right)+\exp\left(-(x-2k+x_0)^2/4t\right)\right]\end{aligned} \tag{3-7}$$

These two expressions are equivalent as shown by application of Poison's formula. Both involve infinite series, but the exponential form converges faster for small t, while the trigonometric representation is advantageous for large t. In this case, the sources are all of the same strength at the locations $x_0 \pm k$ for all integer k. Similar forms can be obtained for mixed or constant potential boundaries.

A solution for the three dimensional problem is achieved by multiplying linear solutions of the form of Eq. 3-7 (Neuman's product rule). Following this, we integrate

over time to account for a continuous rather than an instantaneous sink/source. Finally, an integration of the point sinks/sources over the well segment yields the drawdown expression for M; i.e., $\Phi_D(M,S)$.

Our coupled reservoir-wellbore system has $2N_S$ unknowns: the dimensionless inflow (or outflow) $q_{ID}(i_W, i_L, i_S)$ and potential drawdown $\Phi_{WD}(i_W, i_L, i_S)$ at the midpoint $M(i_W, i_L, i_S)$ of each segment (see Fig. 3-1). The method yields N_S potential drawdown equations, N_S - n_W equations for wellbore hydraulics (of the form of Eq. 3-5) relating the potential of a segment to that of its neighbors, and n_W mass balance equations of the form

$$q_D(i_W) = \sum_{i_W=1}^{n_W} \sum_{i_L=1}^{n_L(i_W)} q_{ID}(i_W, i_L, i_S) , \tag{3-8}$$

for a total of $2N_S$ equations.

The wellbore hydraulics relate the pressure of each segment to that of its neighbor, so it is possible to reduce the number of unknown drawdowns to a single $\Phi_{WD}(i_W, i_L, 1)$ per lateral by inserting Eq. 3-5 into the potential drawdown equations. Because the starting segments at the heel of each lateral are close together, we can assume $\Phi_{WD}(i_W, 1, 1) \sim \Phi_{WD}(i_W, i_L, 1)$. The number of potential drawdown unknowns is then reduced to n_W.

This problem is nonlinear as described and would call for a method such as Newton-Raphson, involving the formation of a Jacobian matrix which would lead to larger computational times. However, it was previously observed that the wellbore hydraulics equations can be decoupled from the system without much loss of accuracy (Ouyang, 1998). As a first step, the linear system of n_W mass balance and N_S potential drawdown equations is solved neglecting the wellbore hydraulics. The solution obtained under these simplifying assumptions (uniform potential or infinite conductivity well condition) gives a first estimate for the in/outflow distribution along each lateral. The wellbore hydraulics can then be calculated and included in the original system. We iterate in this manner until our unknowns are sufficiently accurate. This loosely coupled scheme is efficient and has proven sufficiently robust for the examples considered.

3.2 Incorporation of Skin in Semi-analytical Solution

The mechanical skin effect is generally used to account for altered permeability in the near wellbore region for an otherwise homogeneous reservoir. This concept is commonly extended to account for non-Darcy flow effects, partial completions, completions different from open hole (Thomas et al., 1996) and slanted wells.

Here we will introduce a skin that accounts for the effects of near well heterogeneity on wellbore flow. Before describing how we actually compute this skin, we will first review the skin concept and then describe how skin effects are incorporated into the semi-analytical approach described above. Our actual approach for the calculation of skin is described in the next section.

Hawkins (1956) gave an expression for a dimensionless skin in radial system,

$$s = \left(\frac{k}{k_a} - 1 \right) \ln \frac{r_a}{r_w} , \tag{3-9}$$

This form is obtained by solving for steady state flow in a cylindrical system (resistances in series) as depicted in **Fig. 3-2** for a reservoir of thickness h. The scalar permeability of the unaltered reservoir is k and k_a is a different permeability over the region $r_w < r < r_a$; i.e., in a ring around the wellbore.

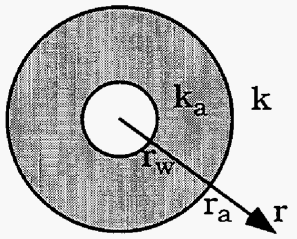

Fig. 3-2: Flow in series in a radial system

We now describe how skin is introduced into the semi-analytical formulation described in the previous section. Consider a lateral with four segments (**Fig. 3-3**) where the fourth segment S_4 has a skin s_4 associated with it. The M_i are the equivalent pressure

points located at a distance r_W from the segment axis (in the isotropic case). A potential drawdown calculated at such a point is taken as the well drawdown at that segment. As an example, the potential drawdown Φ_{WD} in S_1 given itself and all other segments is, by superposition:

$$\Phi_{WD}(S_1) = \sum_{i=1}^{4} q_{ID}(S_i) \cdot \Phi_D(M_1, S_i), \tag{3-10}$$

where $\Phi_D(M,S)$ is the Green's function from the IPSS solution and $q_{ID}(S)$ is the dimensionless in/out flow rate of segment S. However, the drawdown in S_4 is changed due to its skin,

$$\Phi_{WD}(S_4) = \sum_{i=1}^{4} q_{ID}(S_i) \cdot \Phi_D(M_4, S_i) + q_{ID}(S_4) \cdot s_4 \quad . \tag{3-11}$$

Note that Eq. 3-10 still implicitly accounts for the skin s_4 because all of the segment drawdowns are coupled through the wellbore hydraulics. In the case of an infinitely conductive well, the drawdown along the lateral is constant. In the Examples section below, we show a clear validation of this skin implementation (cf. **Fig. 3-4** below).

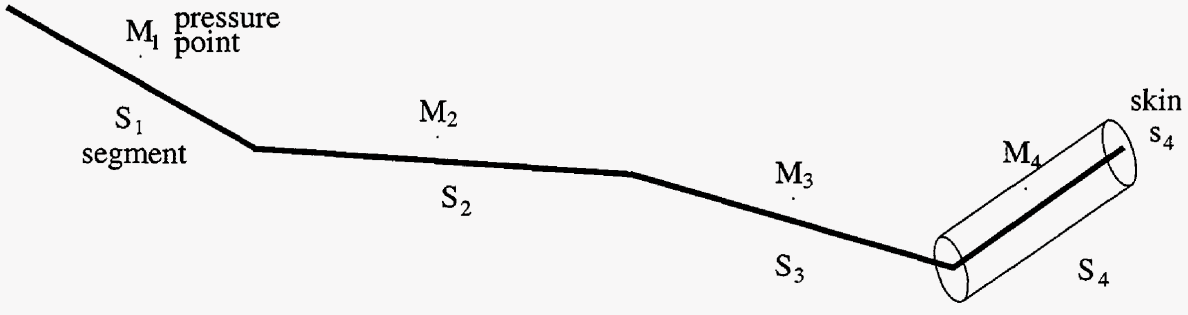

Fig. 3-3: Superposition of segment drawdowns with skin

3.3 Representation of Heterogeneity with s and k*

We have described our basic semi-analytical approach for the representation of non-conventional wells in homogeneous reservoirs and the way in which we incorporate skin into this solution. We now discuss how we represent reservoir heterogeneity in terms of

a background effective permeability $\mathbf{k}^*$ and a local skin along the wellbore. We note that additional skin effects, due to near-well damage or stimulation, could also be included in the overall s-$\mathbf{k}^*$ approach. These skin effects would simply be added to the skin we compute below and the total skin would then be used in the semi-analytical solution.

We will assume that our reservoir models are realizations drawn from an ensemble of known statistics. We will require that the correlation structure; i.e., the correlation lengths in three principal directions, are known. These may not be known a priori, but they can be readily determined via ordinary variogram modeling. We generate our unconditioned permeability realizations on a dense regular grid through use of the geostatistical toolbox GSLIB (Deutsch and Journel, 1998).

As indicated above, the s-$\mathbf{k}^*$ approach requires us to estimate both an average or background permeability and a locally varying skin defined along the wellbore. We first consider the calculation of the skin, s. We can compute this skin with reference to Eq. 3-9. We need to estimate the size and shape of the "altered" zone, the permeability k_a in this altered zone, and the scalar background permeability which will be denoted as k_s^*. The scalar k_s^*, to be used in the skin equations in place of k, will be derived from the diagonal tensor $\mathbf{k}^*$. Therefore, we will defer the description of how k_s^* is computed until after our description of the calculation of $\mathbf{k}^*$.

The size and shape of the altered permeability zone (referred to as the search region) is determined from the correlation structure of the permeability field. For a generally anisotropic correlation structure, we use an elliptical cylinder around each segment. The half axes are aligned with the directions of anisotropy of the variogram and are of length one half of the corresponding correlation length. In Eq. 3-9, r_a is computed as the geometric mean of the two half axes forming the search region. Other choices for r_a are possible though we did not observe much sensitivity to this parameter.

The altered permeability k_a in Eq. 3-9 is computed as a weighted power average of the permeabilities in the search region. Following previous studies in two (Durlofsky, 2000) and three (Desbarats, 1994) dimensions, we represent this average as follows:

$$k_a^{\omega} = \frac{1}{\Gamma_a} \int_a \frac{k^{\omega}(\mathbf{x})}{r^n} d\mathbf{x} \quad , \tag{3-12}$$

where ω designates the averaging exponent (power), r indicates radial distance, n is the distance weighting, and the integral is evaluated over the search region a. The normalization Γ_a is computed via $\Gamma_a = \int r^{-n} d\mathbf{x}$. We evaluate Eq. 3-12 through use of a Monte Carlo type of integration (Press et al., 1993) which randomly samples data points within the search area, excluding the wellbore itself.

The parameters ω and n, and even the size and shape of the averaging region, could be tuned through some type of parameter fit. However, in the examples presented below, we do not introduce any tuning of these parameters. For the log-normally distributed cases considered, we determine ω and n through physical considerations alone. Specifically, we take ω = 0 (logarithmic weighting) and n = 2. This corresponds to a generalized geometric average (strictly applicable for log-normally distributed permeability fields and reasonable for more general cases) weighted appropriately for radial flow.

The global (or background) permeability $\mathbf{k}^*$ is simply computed as the effective permeability for linear flow, as was done previously by Durlofsky (2000). This can be computed most accurately by solving the single phase incompressible pressure equation numerically on the geostatistical fine grid. This calculation must be performed with a prescribed global pressure drop in each of the three coordinate directions to determine the diagonal components of $\mathbf{k}^*$. This calculation is relatively inexpensive as it involves only single phase flow and needs to be done only once for a given realization. However, with very finely gridded permeability fields this calculation can become somewhat demanding.

As an alternative, approximations employing the statistics of the permeability field can be used. We found the approach suggested by Ababou (1990) to be reasonably accurate for our calculations. In three dimensions the diagonal entry of the tensor in coordinate direction d= x,y,z is

$$k_{dd}^{*} = k_g \exp\left[\frac{\sigma_{\ln k}^2}{2}\left(1-\frac{2l_h}{3l_d}\right)\right] . \qquad (3\text{-}13)$$

This formula was developed for log-normally distributed permeability fields which have a geometric mean k_g and correlation lengths l_d (l_h is the harmonic average of the three correlation lengths). Note that this equation uses $(\sigma_{\ln k})^2$, the variance of the log-permeability. In the examples below we specify the log-normal permeability fields in terms of the mean m and the coefficient of variation (standard deviation divided by mean) C_v rather than in terms of $\sigma_{\ln k}$.

As indicated above, although our effective permeability (computed in either manner) is a diagonal tensor, the skin formula is in terms of a scalar k. We therefore set $k = k_s^* = (k_{xx}^* \, k_{yy}^* \, k_{zz}^* \,)^{1/3}$ in Eq. 3-9 (i.e., $k = k_s^*$ is the geometric average of the $\mathbf{k}^*$ permeability components).

Our s-$\mathbf{k}^*$ approach provides a varying skin distribution along the laterals of the wells. Using this skin, the semi-analytical tool computes a flow and pressure response (or productivity) for each well segment. Comparisons between these results and those of a standard finite difference numerical simulation will be discussed in the next section. We note here, however, that given a "true" flow and pressure response from the finite difference simulator, it is possible to determine a skin distribution that matches this reference solution up to an arbitrarily small error. We refer to this skin as the *true skin*. Due to the relatively weak coupling of the system, we can compute the true skin using a simple perturbation method rather than a general optimization procedure. Though this true skin is computed for a given time, it appears to provide an accurate approximation for other times, including the early transient period.

The concept of true skin is useful for several reasons. Most notably, it establishes the existence (in a numerical sense) of an s-$\mathbf{k}^*$ type of solution for the types of permeability fields considered. Further, in tuning the method, the skin distribution can be matched rather than the inflow profile, saving computation time. Finally, a true skin computed for single phase flow can be applied for more general cases, such as in a general multiphase flow problem in a finite difference simulator.

Although the overall semi-analytical approach is only appropriate for single phase flow, it might be possible to use the technique to qualitatively represent some effects due to multiphase flow. For example, the method might be used to model the effects of trapped water or gas within the wellbore, which can occur in wells of undulating trajectory. Assuming the locations of these regions are known or can be estimated, the well performance could be modeled by prescribing high skin in the affected regions (to minimize local inflow) and by modifying the wellbore friction model (to capture the effects of the additional phase on the wellbore pressure loss). Such a treatment would of course be very approximate, but it might be useful in some cases for a qualitative evaluation of well performance.

3.4 Examples

The examples presented in this section demonstrate the capabilities of the proposed method. Most of these results are compared with those from a finite difference numerical simulator (Eclipse Reservoir Simulator, 1996). This reference solution was computed using the detailed geostatistical model (45×45×35 cells) and the default well model of Peaceman (1983).

The s-$\mathbf{k}^*$ semi-analytical solution approach was implemented in a C++ code. The code is quite efficient computationally and requires only about 2 minutes of computation time on a single 400 MHz processor for a 50 segment model at a given report time. The code is not fully optimized, so these timings could be improved. The computation time is independent of the orientations of the wells and segments and depends largely on the number of actual segments. The code has been parallelized and the increase in speed is nearly linear with the number of processors. This high degree of parallel efficiency results because the computation time is dominated by the formation of the matrix, which parallelizes very naturally. The time requirements for the semi-analytical solution method are essentially independent of the level of detail in the geostatistical permeability description (though the numerical calculation of $\mathbf{k}^*$ will scale with the size of the fine grid model). Therefore, the efficiency advantage of the method over a finite difference technique will increase as the model size increases. It is also important to note that the extra

overhead of the s-$\mathbf{k}^*$ method compared to the base semi-analytical method is insignificant; the calculation of skin along the wellbore requires only about 5 seconds for an example with 50 segments.

In the calculations below, we consider slightly compressible single phase flow. In most cases, we use only straight well laterals, which are aligned with the grid in the finite difference simulator. We do not include wellbore hydraulics except when otherwise stated. Gravitational effects are included in all of the calculations. Ten logarithmically spaced time steps were taken in the finite difference runs out to a final time of 100 days.

Tables 3-1 to **3-3** provide the basic reservoir description, the statistics of four different log-normally distributed permeability realizations (referred to as perm*X*), and schematics of the various well geometries (well*Y*) respectively. The examples involve different well geometries coupled with the different permeability realizations. In Table 3-2, l_x, l_y, l_z refer to dimensionless correlation lengths; i.e., the actual correlation length non-dimensionalized by the reservoir length in the appropriate coordinate direction. Spherical variogram models with no sill were used in all cases. Note that in Table 3-3 only the black well sections are perforated; the gray lines indicate the location of the vertical pilot hole (the heel of lateral).

3.4.1 Anisotropic Reference Case. Our first example serves to demonstrate that skin is implemented correctly in the semi-analytical solution. The reservoir is homogeneous but anisotropic with permeability prescribed as k_{xx}=200, k_{yy} =100, k_{zz} =50 md. This example follows geometry wellA of Table 3-3: the well is fully penetrating and produces at 10,000 STB/d. Five different skin values (s=0,-2,0,1,3, see Table 3-3) are specified along the well. In the semi-analytical solution, the well is modeled with 45 segments.

The semi-analytical (solid curve) and finite difference (dashed curve) solutions for inflow as a function of position along the well ξ are presented in Fig. 3-4. The curves represent the total inflow into each segment (solid curve) or grid block (dashed curve). The agreement between the two curves is clearly very close, indicating that skin is properly implemented into the semi-analytical solution technique. As is evident from Fig. 3-4, the inflow is reduced in sections of positive skin, as would be expected. End effects

at the boundaries of the skin zones are also apparent; e.g., segments of low skin draw additional fluid from adjacent higher skin regions.

Table 3-1: Reservoir, Fluid and Well Properties

drainage area	4500 x 4500 ft^2
thickness	175 ft
vert. bounds	sealing (no flow)
horiz. bounds	sealing (no flow)*
porosity ϕ	0.25
compress. c_t	3.0×10^{-5} psi^{-1} at p_{ini}
density ρ	60 lb_m/ft^3
viscosity μ	1 cp
form. fac. B	1.05 RB/STB
initial potential φ_{ini}	3000 psi
total rate Q	10,000 STB/d (primary*)
min. bhp $p_{w,min}$	2800 psi (secondary*)
well radius r_w	2.4 in.
report time	40 days

*these specifications differ for the fixed pressure example

Table 3-2: Statistics of the Permeability Fields

realization	permA	permB / B2	permC
mean m	100 md	103 / 101 md	109 md
coefficient of variation C_v	1	1.8 / 1.6	1.4
corr. structure $\{l_x=l_y, l_z\}$	0.3, 0.3	0.3, 0.1	0.5, 0.05
background perm. k_s^*	79 md	67 / 67 md	136 md

Table 3-3: Well Configurations of the Examples Presented

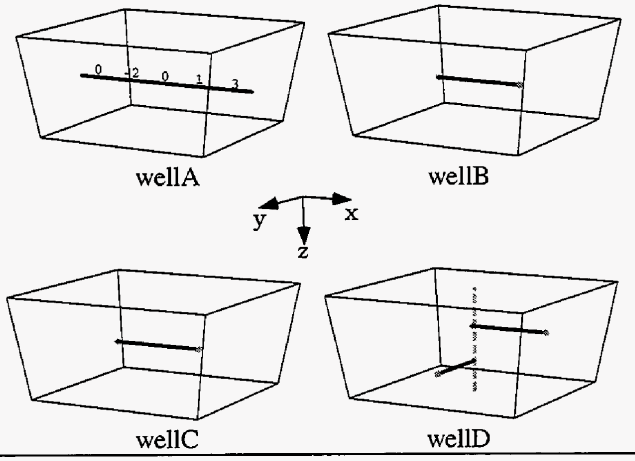

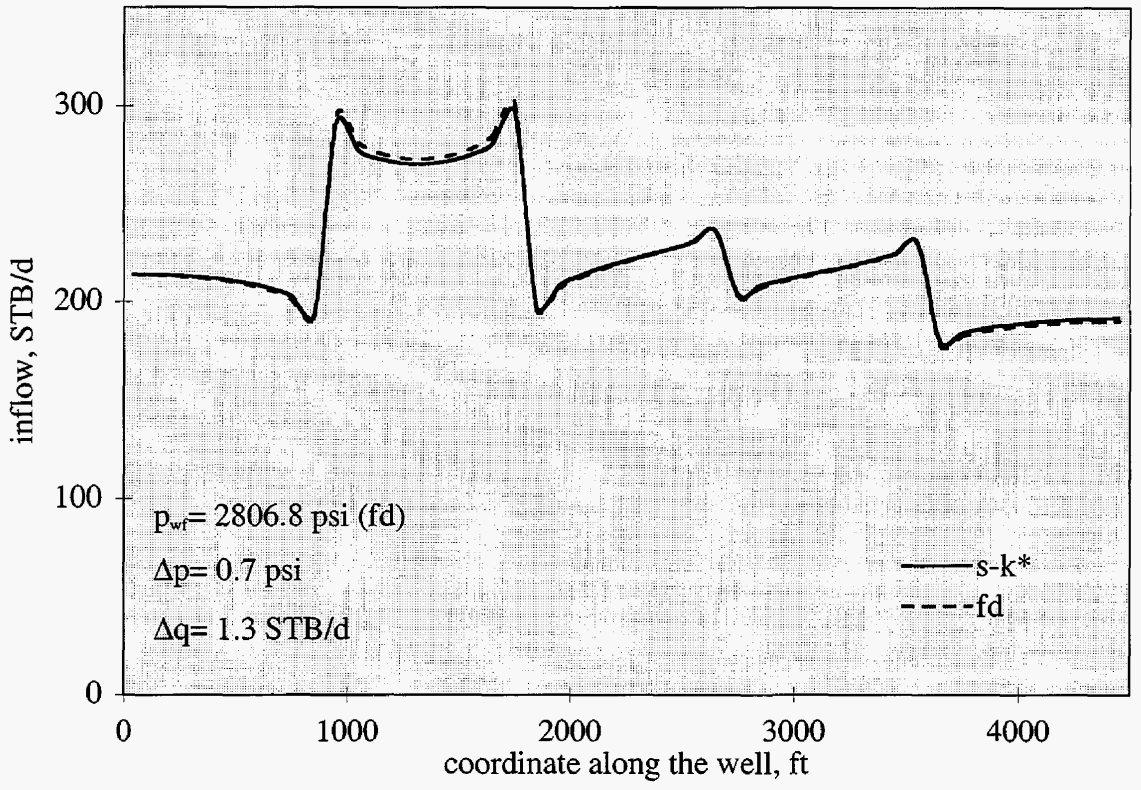

Fig. 3-4: Production profile for wellA in a homogeneous, anisotropic reservoir with skin prescribed

Because wellbore hydraulics are not included in these calculations, pressure is constant from the heel (ξ=0) to the toe (ξ =4500 ft) of the well in both calculations. The difference in the wellbore pressures for the two cases is only 0.7 psi, indicated as Δp in the figure. In this and all subsequent production plots, a measure of the difference between the inflow profiles for the semi-analytical and the finite difference results is also provided. This quantity, designated Δq, is simply the L_1 norm of the differences between the two solutions; i.e., $\Delta q = (1/n_S)\sum_i \left|q_{fd} - q_{s-k^*}\right|_i$.

We now consider several heterogeneous cases and apply the procedures described above to determine the skin profile along the well and $\mathbf{k}^*$.

3.4.2 Fixed Flow Rate Cases. Our next example involves the heterogeneous permeability realization permA and well configuration wellA. A horizontal cross section of this permeability field, through the plane containing the well, is shown in **Fig. 3-5**. Darker

regions correspond to higher permeabilities. The well is indicated in the figure by the dashed line. The typical "radius" of the correlated regions of permeability is about 30% of the system size (recall that $l_x = l_y = 0.3$ in this case). For this permeability field, the diagonal components of $\mathbf{k}^*$, obtained from a single phase simulation (Deutsch and Journel, 1998) on the fine grid, are 93.0, 91.6 and 57.2 md. This compares to 97.5, 97.5 and 52.6 obtained by the approximate homogenization method of Ababou (1990) (Eq. 3-13).

Fig. 3-6 displays the production profiles for this case for the semi-analytical and finite difference computations. The agreement between the two methods is quite good, though there are clearly larger differences between these two results than was observed in the previous example. In this example, Δq=25.3 STB/d and Δp=1.7 psi. The average inflow per segment in this case is 10,000/45=222 STB/d, so a Δq of 25.3 STB/d indicates that the error in local inflow is typically about 10%. The wellbore pressure is even more accurate; the total drawdown (defined here as the difference between the initial wellbore pressure and the wellbore pressure at a given time) is about 168 psi. Therefore, the error in pressure is only about 1%.

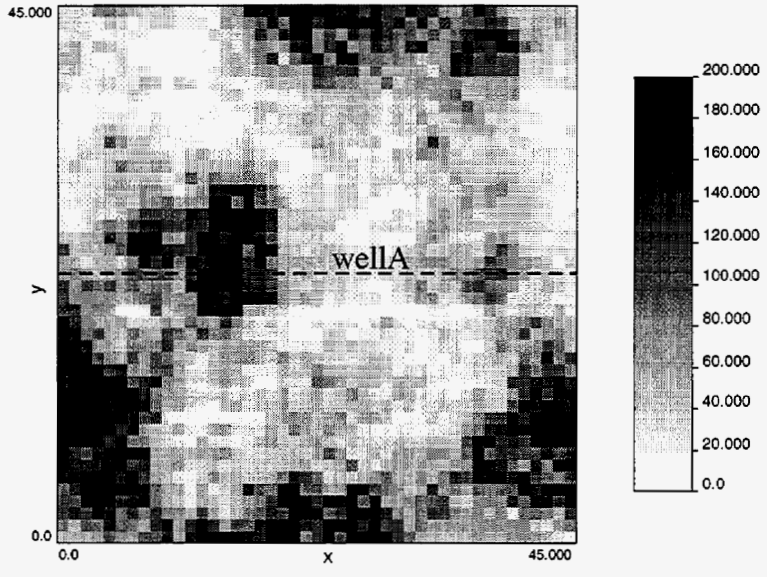

Fig. 3-5: Permeability in the horizontal cross section containing the well (permA, wellA)

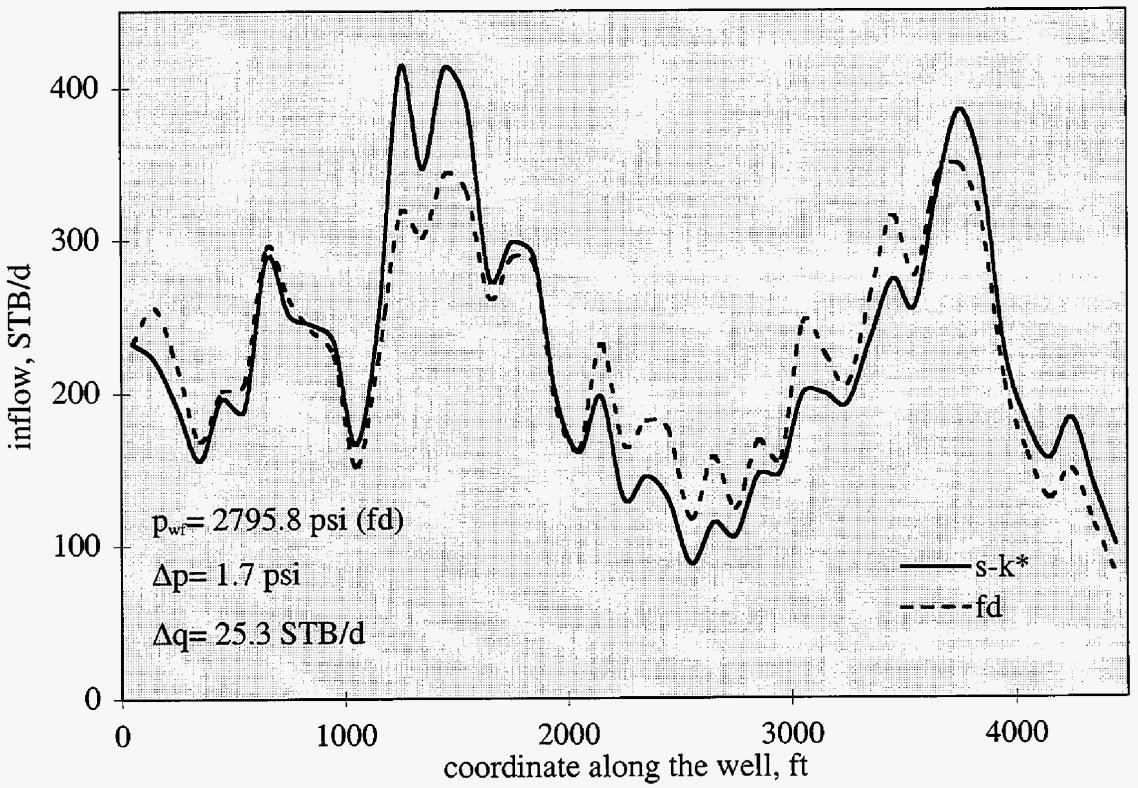

Fig. 3-6: Production profile for wellA in a heterogeneous reservoir (permA)

The variation in inflow with position along the wellbore is quite significant in this case. As is evident from Fig. 3-5, the well intersects a broad distribution of permeability values. Two major peaks can be observed at $\xi \sim 1400$ and $\xi \sim 3800$ ft. These peaks clearly correspond to high values of the permeability field (compare Figs. 3-5 and 3-6). In general the peaks in inflow are captured with reasonable accuracy by the s-$\mathbf{k}^*$ approach, though the higher peak at $\xi \sim 1400$ ft is somewhat overestimated. We note that these large variations in inflow with position could well lead to the early breakthrough of water or gas. That is of course not modeled with our method, however.

As discussed above, it is possible to determine a true skin which provides, per definition, an exact match between the finite difference and s-$\mathbf{k}^*$ productivity results. We computed this true skin for the case considered above (wellA in permeability field permA). The true skin distribution, as well as the estimated skin (which was used for the results presented in Fig. 3-6), are shown in **Fig. 3-7**. The estimated skin tracks the true

skin relatively closely, though there are clearly some differences. These differences are most important in regions of high negative skin (e.g., at $\xi \sim 1400$ ft).

Our next example (**Fig. 3-8**) is for the same well geometry but a different permeability field (permC). The agreement for the inflow distribution, Δp and Δq are again quite good for the most part. The inflow estimation deviates considerably from the finite difference result at the toe of the well ($\xi = 4500$ ft), however, which is where the major contribution to Δq originates. This error is due to an inaccurate estimate of skin (relative to the true skin) in this region. Specifically, the skin estimate is negative while the true skin is positive. It may be possible to improve the skin estimate through some tuning of the parameters in Eq. 3-12.

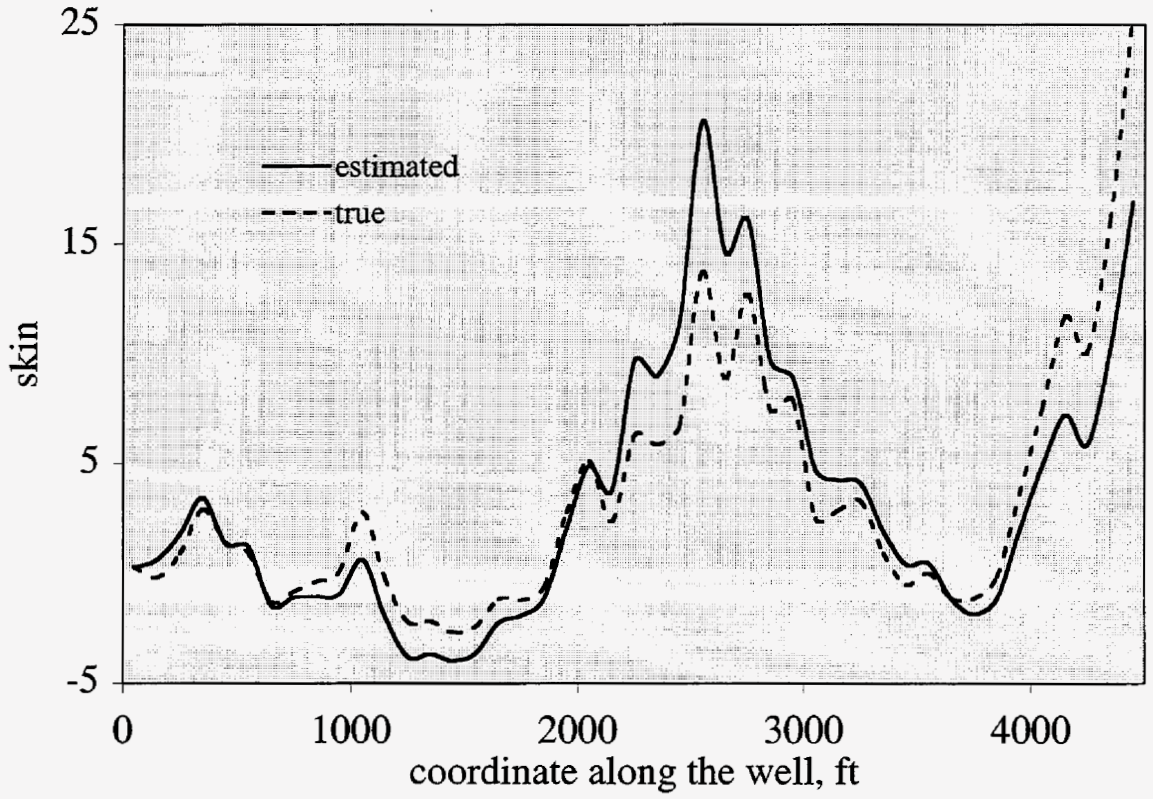

Fig. 3-7: Estimated and true skin distributions along the well (permA, wellA)

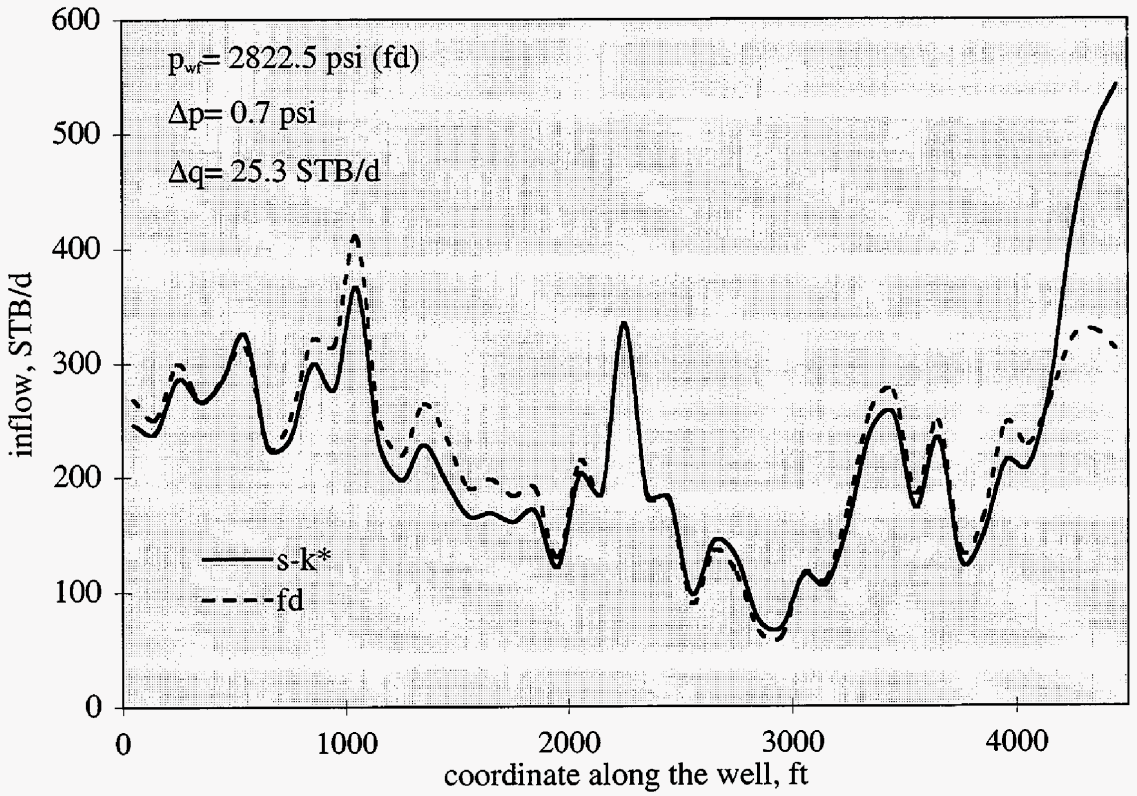

Fig. 3-8: Production profile for a different permeability field (permC, wellA)

3.4.3 Fixed Pressure Cases. For the following cases, we consider a 2100 ft partially penetrating horizontal well (wellB of Table 3-3) operating at a fixed pressure of p_W=2800 psi. The well is modeled using 21 segments in the s-$\mathbf{k}^*$ calculations. An aquifer located below the reservoir (z=175 ft) maintains the pressure at the initial value of 3000 psi. In the results presented below, we consider two different realizations of the same geostatistical model, permB and permB2. Due to finite size effects, these two realizations do not have identical statistics (cf. Table 3-2).

In **Fig. 3-9** we show the well production profile using permB. Because p_W is specified, Δp is identically zero. The total inflow rates are, however, different between the various models. For the finite difference results, Q_{fd} = 19,900 STB/d, while the s-$\mathbf{k}^*$ method gives $Q_{s\text{-}k^*}$ =17,300 STB/d, an error of about 13%. On a per segment basis, the error in inflow rate is about the same. An additional curve is also shown in the figure

(denoted as "k^* only"); this corresponds to the semi-analytical result using $\mathbf{k}^*$ but setting s=0 everywhere. Such a result might be obtained with previous semi-analytical methods that are unable to account for heterogeneity. This result is clearly unable to track the finite difference result, though it does provide an accurate estimate of the total flow (Q_{k^*} =18,700 STB/d, an error of only 6% relative to the finite difference result).

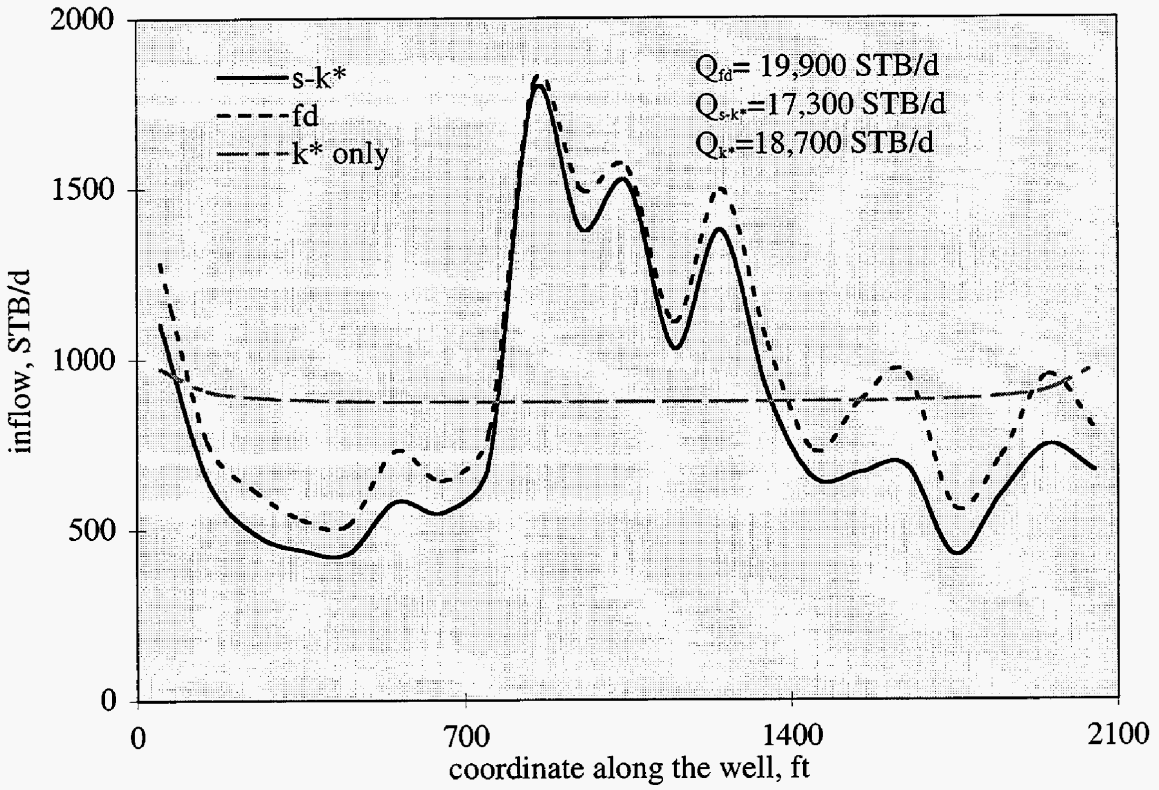

Fig. 3-9: Production profile for fixed pressure example (permB, wellB)

The next case involves permeability field permB2 (**Fig. 3-10**). Here, the agreement of the s-$\mathbf{k}^*$ results and the finite difference results is quite close. The total inflow rates are Q_{fd} =10,300 and $Q_{s\text{-}k^*}$ =10,200 STB/d, respectively, an error of about 1%. On a per segment basis, this error is also only 1%. The semi-analytical result using $\mathbf{k}^*$ with s=0 is again shown. In this case the results for total inflow using this method are poor; Q_{k^*} =18,500 STB/d, an error of 80% relative to the finite difference result. The results for Q_{k^*} are quite similar for both permB and permB2 because $\mathbf{k}^*$ is close for the two cases.

However, because the permeabilities along the well path are quite different between the two realizations, the well productivities differ considerably. The use of $\mathbf{k}^*$ alone is unable to capture this effect. This is consistent with earlier results for two dimensional systems, where the well productivity was seen to vary by orders of magnitude between realizations of the same statistics, even though $\mathbf{k}^*$ was the same between realizations (Durlofsky, 2000).

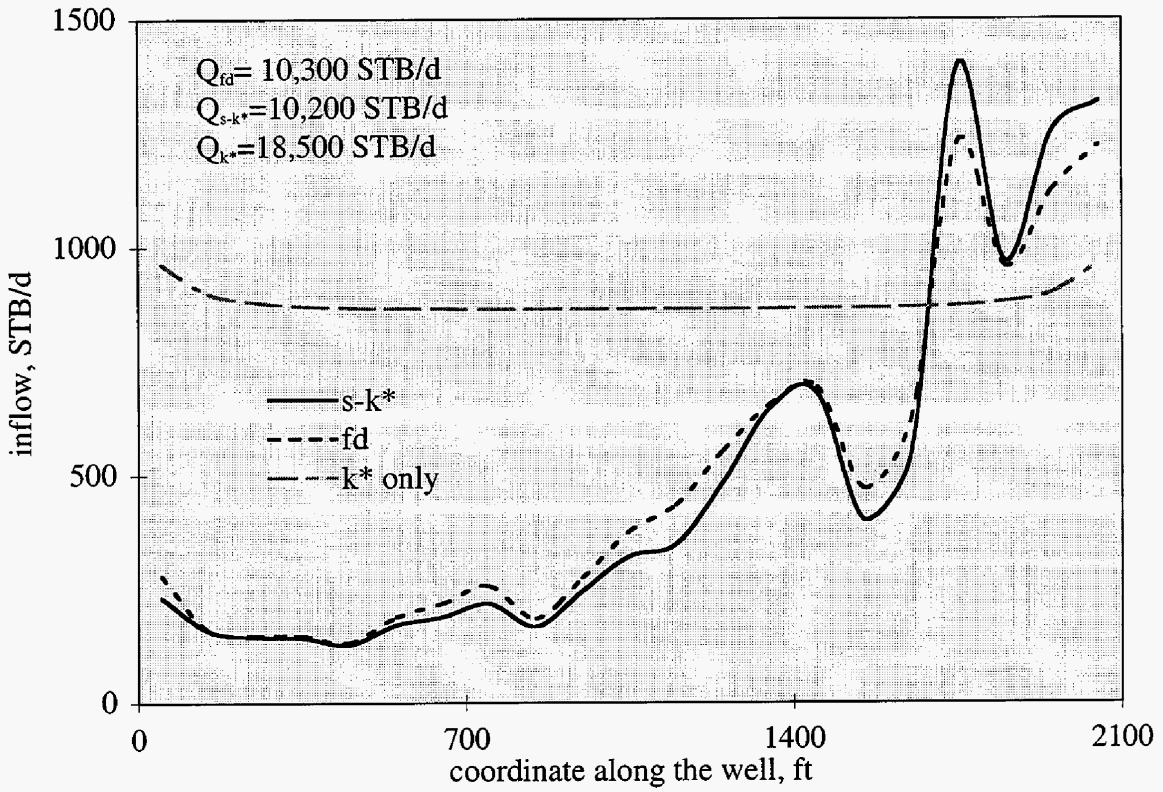

Fig. 3-10: Same as Fig. 3-9 but with a different permeability realization (permB2)

3.4.4 Multilateral Case. We now consider the multilateral configuration wellC in Table 3-3. The two horizontal sections are perforated and have a total production constraint of 10,000 STB/d. Each lateral is modeled using 18 segments. The production profiles for the upper lateral are shown in **Fig. 3-11** and those for the lower in **Fig. 3-12.** The inflow profile computed using s-$\mathbf{k}^*$ is in close agreement with the finite difference results for

both laterals. As indicated in the figures, the differences in pressure between the finite difference and s-$\mathbf{k}^*$ calculations are 4.6 psi for both laterals. The finite difference result for the total production from the upper lateral is Q_{fd} =2900 STB/d, while the s-$\mathbf{k}^*$ result gives $Q_{s\text{-}k^*}$ =2600 STB/d, representing a difference of 10%. For the lower lateral, Q_{fd} =7100 STB/d and $Q_{s\text{-}k^*}$ =7400 STB/d; an error of 4%. Differences in the contributions of the two laterals to total well inflow are likely due to gravitational effects and permeability heterogeneity.

The close agreement between the finite difference and s-$\mathbf{k}^*$ results in this case suggests that both approaches are reasonably accurate. However, in some cases, such as when the heels of the two laterals are relatively close together, the finite difference results may begin to lose accuracy. This is because the finite difference results rely on the simplified Peaceman (1983) model to compute the well index. The assumptions of that model (two dimensional radial flow due to an isolated well) are clearly violated when there is strong communication between the two laterals. In such cases, the s-$\mathbf{k}^*$ approach might well provide more accurate results than the finite difference method.

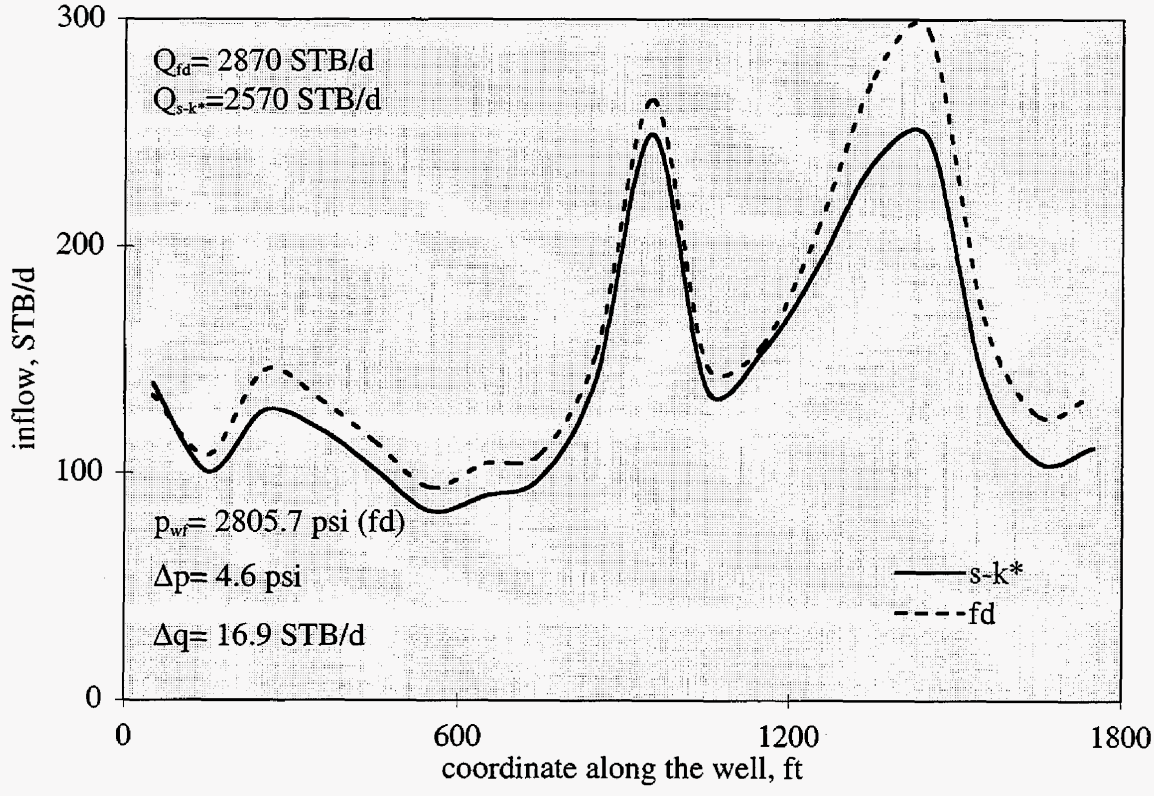

Fig. 3-11: Production profile for the upper lateral of multilateral (permC, wellC)

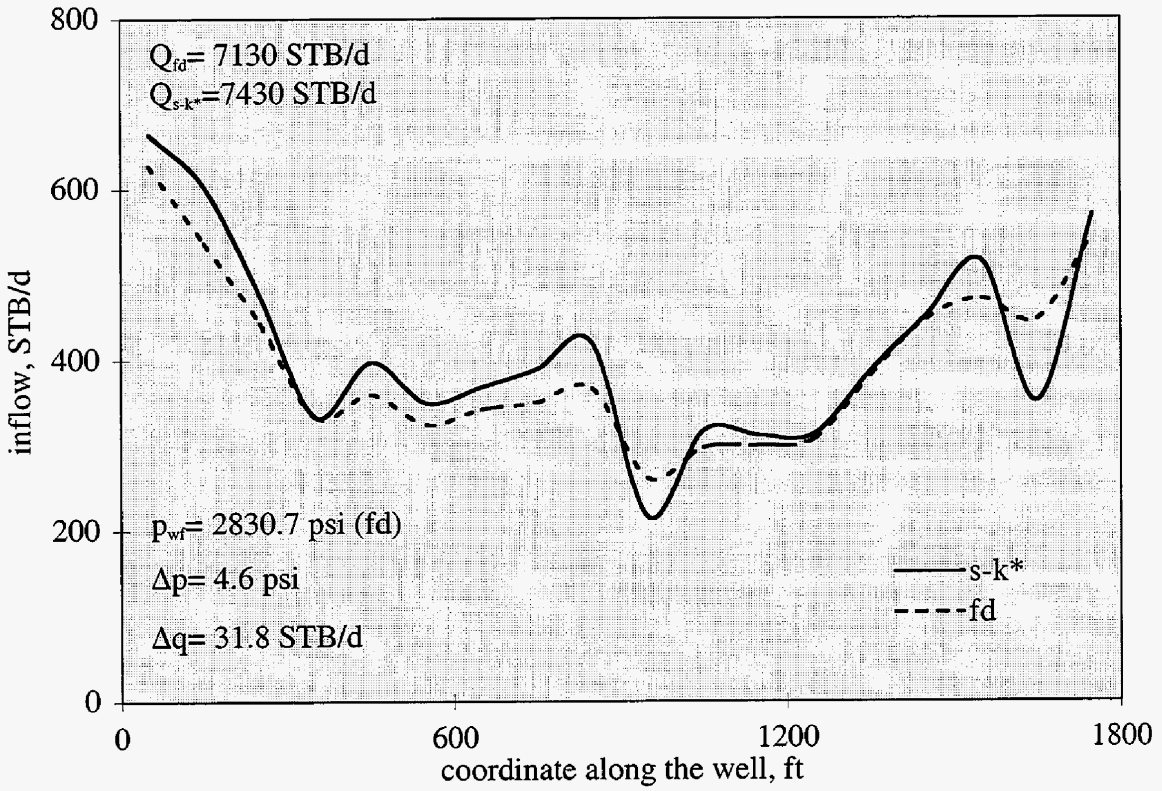

Fig. 3-12: Production profile for the lower lateral of multilateral (permC, wellC)

3.4.5 Complex Trajectory with Wellbore Hydraulics. Our final example involves wellD in a reservoir with permC. In this example, we consider the effects of wellbore hydraulics on the production profile. We do not compare our results for this case with the finite difference results because deviated wells are somewhat difficult to model using finite difference methods. The well is modeled using 23 segments and operates at a fixed total inflow rate of 10,000 STB/d. Wellbore hydraulic effects due to friction (with pipe roughness set to 0.0001 ft) and acceleration are included in the model.

We present results for both wellbore pressure (right vertical axis) and inflow rate (left vertical axis) as a function of position for this case. The solid curves in **Fig. 3-13** show the s-$\mathbf{k}^*$ results with no wellbore hydraulics and the dashed curves show results with wellbore hydraulics included. Note that, even when pressure drop due to friction and acceleration is neglected, the wellbore pressure profile is no longer uniform because

the well dips in the middle section. There are clearly some differences between the wellbore pressure profiles. Differences in the inflow profile are, however, relatively slight.

This example serves to illustrate the potentially complex interplay between wellbore hydraulics and the local permeability heterogeneity. Even though the effects of wellbore hydraulics are not dominant here, in some cases both effects must be included in the model to obtain accurate results. In the next section, we apply the s-$\mathbf{k}^*$ approach to study the combined effects of wellbore hydraulics and permeability heterogeneity on the performance of non-conventional wells.

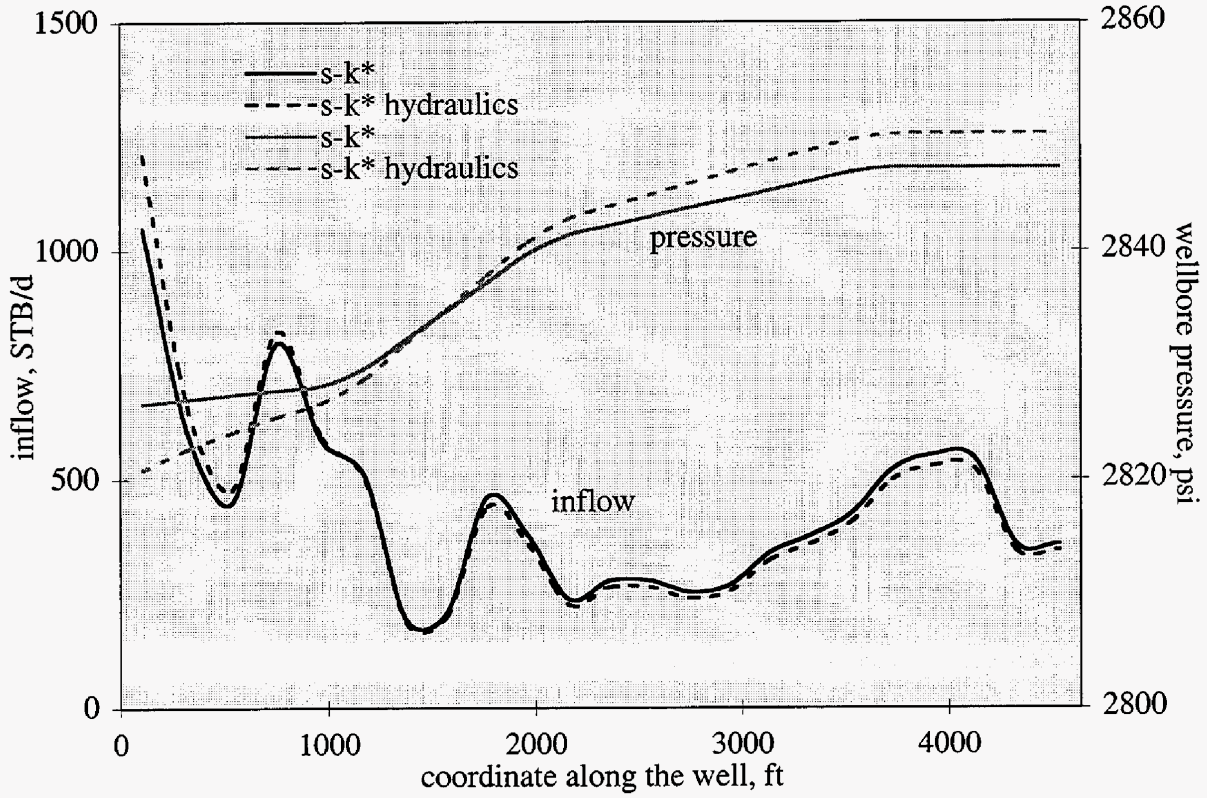

Fig. 3-13: Effect of hydraulics on production and pressure profiles of a complex trajectory well (permC, wellD)

3.5 Assessment of the Combined Effects of Heterogeneity and Wellbore Pressure Drop

In this section we apply our semi-analytical solution methodology to assess the performance of horizontal wells in heterogeneous reservoirs with wellbore pressure effects included. We consider many realizations of heterogeneous reservoirs of prescribed statistics to enable us to draw conclusions regarding average behavior and the degree of variation. We first describe our assessment procedure and then present detailed numerical results.

3.5.1 Calculation of well productivity. Well productivity, designated *PI*, is defined as the ratio of the total well production Q to the difference in pressure between the reservoir and the well Δp. At a given time, we take the reservoir pressure to be the average reservoir pressure $<p>$ and the well pressure to be the pressure at the heel of the well, $p_W(\xi=0)$. The expression for *PI* is then

$$PI = \frac{Q}{\Delta p} = \frac{Q}{< p > - p_W(0)} \quad , \tag{3-14}$$

where $<p>$ is determined from the material balance for a closed, slightly compressible system:

$$< p > = \Phi_0 - \frac{B_o}{c_t} \ln \frac{V_\phi + B_o \int Q \, dt}{V_\phi} \quad . \tag{3-15}$$

Here, Φ_0 is evaluated at the midpoint of the reservoir, B_o is the oil formation volume factor, c_t is the total system compressibility and V_ϕ is the total pore volume. The accuracy of Eq. 3-15 was verified through comparison to detailed simulation results.

These expressions define the productivity of a well in a single realization of the heterogeneous permeability field. We refer to the productivity for a single realization k as PI^k. The expected productivity for an ensemble of N such realizations of identical statistics, designated $\overline{PI}$, is given by the average of the N productivities; i.e.,

$$\overline{PI} = \frac{1}{N}\sum_{k=1}^{N} PI^k \quad . \tag{3-16}$$

Similarly, the standard deviation (designated σ_P) around $\overline{PI}$ can be computed.

This "average" productivity can be contrasted with another measure of productivity, namely the productivity computed for a single permeability field with "average" (homogeneous) permeability $\mathbf{k}^*$. This $\mathbf{k}^*$ represents the effective permeability of all of the realizations of the same prescribed statistics. We designate the productivity for a system of constant permeability $\mathbf{k}^*$ as PI^*, in contrast to the $\overline{PI}$ defined above. The quantity PI^* in a sense describes the productivity for an averaged system, as opposed to $\overline{PI}$, which describes the average productivity for an ensemble of permeability fields of prescribed statistics. For systems of finite size, the effective permeabilities for the various realizations will differ slightly. In the results for PI^* below, the $\mathbf{k}^*$ used in the calculation is the average of the $\mathbf{k}^*$'s for each of the N realizations.

In addition to heterogeneity, we wish to study the effects of wellbore pressure loss. We consider systems both with and without wellbore pressure losses in order to gauge the magnitude of the effect. We introduce the subscripts 1 and ∞ to designate calculations for wellbores of finite conductivity (wellbore losses are included) and for wellbores of infinite conductivity (no wellbore pressure losses), respectively. With this notation, the quantity PI_1^k designates the productivity for a single realization with wellbore losses included in the calculation, while PI_∞^k designates the productivity for the same realization with no wellbore losses. Similarly, the quantity $\overline{PI}_1$ designates the ensemble-average productivity for a well in a heterogeneous system with wellbore losses included, while $\overline{PI}_\infty$ designates the ensemble-average productivity for the well in a heterogeneous system with no wellbore losses. The quantities PI_1^* and PI_∞^* are defined analogously for a system of constant permeability $\mathbf{k}^*$.

Another quantity of interest is the ratio of the well productivity with wellbore pressure losses included to the productivity without pressure losses. If this ratio is very close to unity for a particular scenario, this indicates that wellbore pressure effects are not

significant in that case. We designate this productivity ratio, for a particular realization, R^k; i.e., $R^k = PI_1^k/PI_\infty^k$. The average and standard deviation of R over N realizations are designated $\overline{R}$ and σ_R. Comparison of $\overline{R}$ to the quantity $R^* = PI_1^*/PI_\infty^*$ will indicate whether or not a single calculation (using averaged properties) gives an accurate indication of the ensemble-average effect of wellbore pressure losses. The usefulness of this quantity will also depend on the magnitude of σ_R relative to $\overline{R}$. The applicability of these definitions and comparisons will become clear below when we consider results for actual systems.

3.6 Numerical Examples

We consider three different systems. Each system corresponds to a particular well geometry and a particular geostatistical correlation structure for the permeability field (Tables 3-1 to 3-3). The permeability field is specified in terms of the dimensionless correlation lengths in each coordinate direction. For each case, we generate 30 unconditioned geostatistical realizations using GSLIB (Deutsch and Journel, 1998). This corresponds to the case in which a new well is drilled in a region away from hard data, though the permeability variogram is assumed to be known. By rescaling these realizations under the assumption of log-normality, we generate systems of different overall C_v. We consider $0 \leq C_v \leq 2$; due to the finite data size of the permeability realizations, the back-calculated values of C_v differ slighly from the prescribed values.

Productivities for each realization k, both with (PI_1^k) and without (PI_∞^k) wellbore hydraulics included, are computed using our semi-analytical method. In addition, we compute productivity for a single homogeneous case, with and without wellbore hydraulics, using the average $\mathbf{k}^*$ from the corresponding 30 realizations (this gives PI_1^* and PI_∞^*). All other system parameters are fixed and do not vary between realizations. In all cases, the well is specified to produce at a constant rate of Q=20,000 STB/d. Productivity values are presented at t=100 days.

3.6.1 Long horizontal well. The first example involves a fully penetrating well (wellA in Table 3-3) and permeability model permA. The well length is large compared to the areal correlation length of the system (l_x=l_y=0.3). **Fig. 3-14** shows the $\overline{PI}_\infty$ (dark diamonds) and the corresponding PI_∞^* (white squares) as a function of the coefficient of variation of the permeability field. Error bars corresponding to one standard deviation σ_P are drawn along with the $\overline{PI}_\infty$ data. From the figure we see that, for $C_v > 0.1$, both $\overline{PI}_\infty$ and PI_∞^* decrease with increasing C_v. This is because $\mathbf{k}^*$ decreases with increasing C_v due to our method for rescaling permeability. The variation from realization to realization, quantified via σ_P (error bars), increases with increasing C_v up to $C_v \sim 1$, after which it is approximately constant. At the highest value of C_v, the productivities computed for the 30 realizations vary by a factor of about 2.8 (i.e., $PI_\infty^{max}/PI_\infty^{min} \sim 2.8$).

Also of interest is the location of the PI_∞^* results (white squares) relative to the $\overline{PI}_\infty$ results. The PI_∞^* results consistently exceed the $\overline{PI}_\infty$ results, demonstrating that the results for the "averaged" system do not necessarily agree with the ensemble-averaged results. The overprediction in this case is fairly consistent at about one standard deviation.

We next consider the same system (and the same 30 realizations) but now include the effects of wellbore hydraulics. The results for this case are shown in **Fig. 3-15**. The symbols here are the same as in Fig. 3-14. The results in Fig. 3-15 are quite analogous to those in Fig. 3-14 and the same trends are evident. However, the $\overline{PI}_1$ and PI_1^* data in Fig. 3-15 are consistently less than the $\overline{PI}_\infty$ and PI_∞^* data in Fig. 3-14. This is as expected and demonstrates the effect of wellbore losses on well productivity.

We quantify the effect of wellbore hydraulics on productivity in **Fig. 3-16**, where we plot the productivity ratios $\overline{R}$ and R^* versus C_v. There are several interesting features to Fig. 3-16. First, we note that the general magnitude of both $\overline{R}$ and R^* varies from about 0.78 at low C_v to about 0.87 at high C_v (this trend may be due to $\mathbf{k}^*$ decreasing with increasing C_v). This indicates that wellbore hydraulics reduce productivity by 13-22% on average for these cases. Further, we see very close agreement between $\overline{R}$ and R^* and

relatively small error bars (low σ_R) around the $\overline{R}$ results. This indicates that the impact of wellbore hydraulics on the productivity ratio is accurately represented by the homogeneous case. This suggests that a single simulation (of a homogeneous system) can be used to gauge the effect of wellbore hydraulics on productivity for a set of heterogeneous realizations of the same $\mathbf{k}^*$ (and other system parameters). This is an interesting observation, because as we saw above (Figs. 3-14 and 3-15), the homogeneous case does not provide a very accurate estimate for the ensemble-averaged productivity in either case. However, it does provide an accurate estimate for $\overline{PI}_1 / \overline{PI}_\infty$.

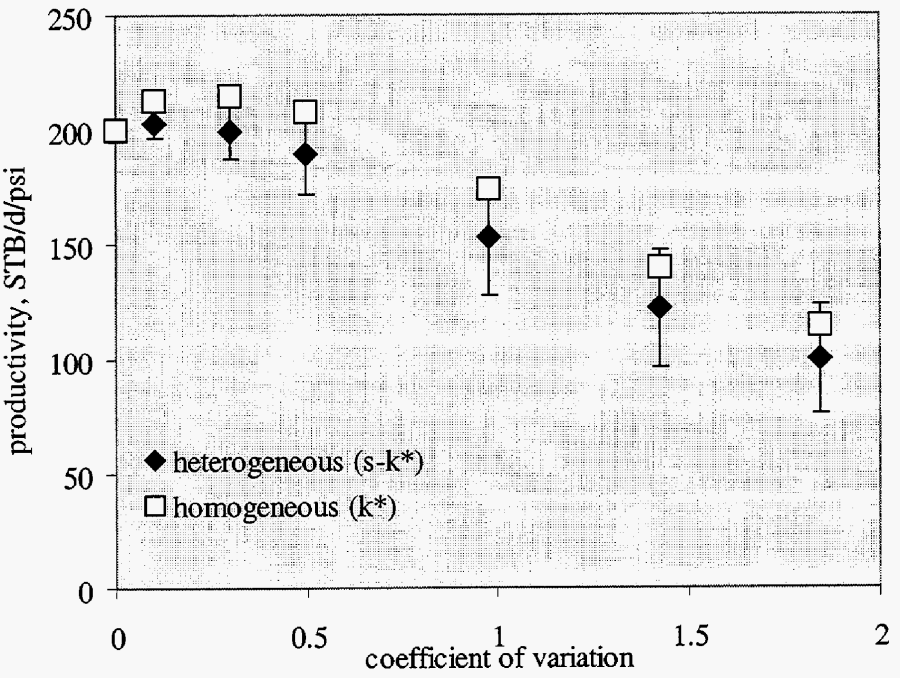

Fig. 3-14: Productivity plot (permA, wellA, infinite conductivity)

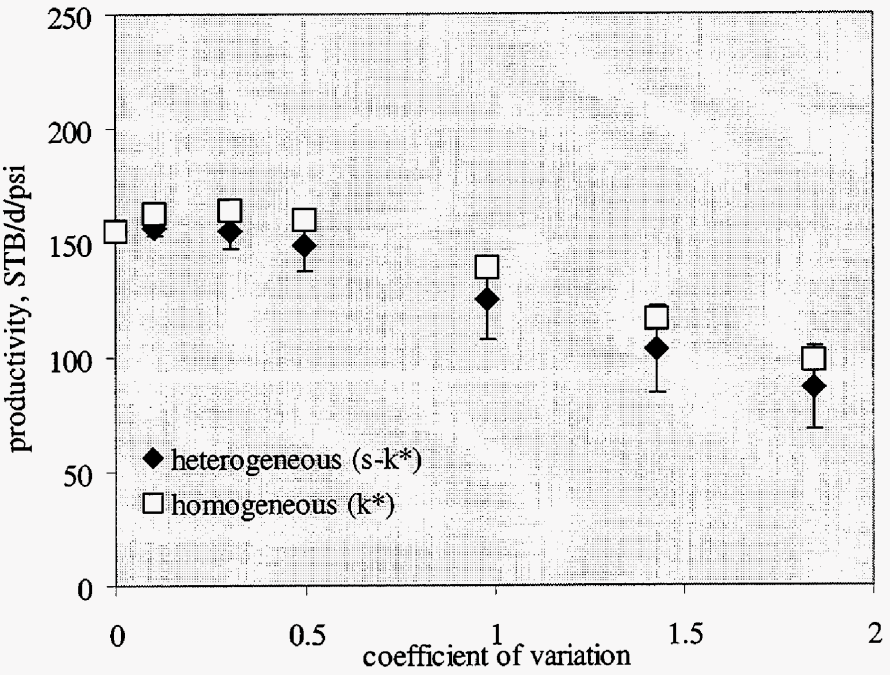

Fig. 3-15: Productivity plot (permA, wellA, finite conductivity)

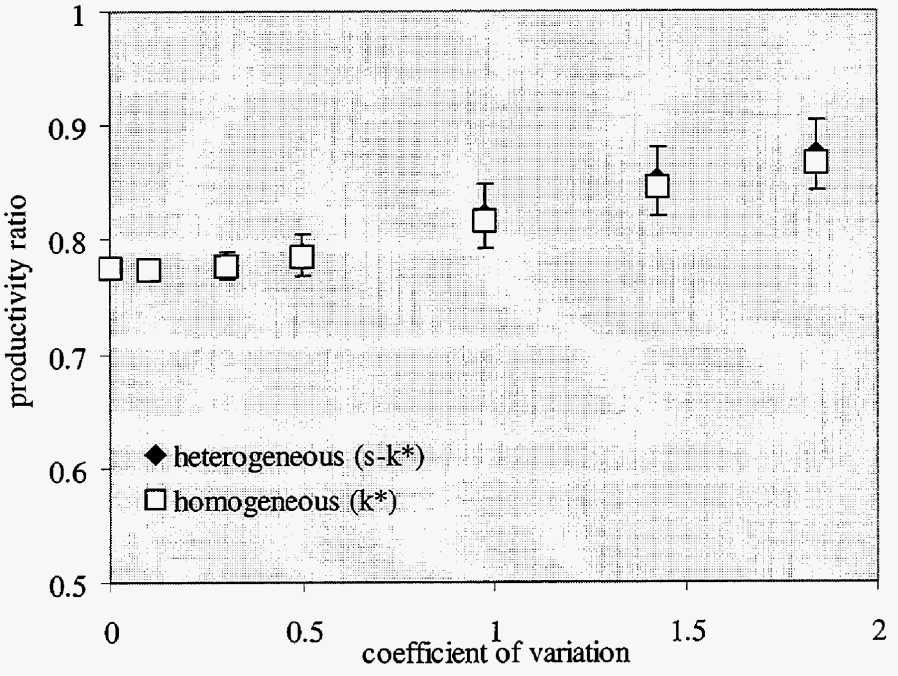

Fig. 3-16: Productivity ratio plot (permA, wellA)

3.6.2 Short horizontal well. We next consider a partially penetrating well (wellB in Table 3-3) in a permeability field (permB) of smaller vertical correlation length (l_z=0.1) than in the previous case. The well length is now only about $1.5 \times l_x$. We show productivity results in **Fig. 3-17** for the infinitely conductive case; **Fig. 3-18** displays analogous results for the case of finite conductivity. Results for the productivity ratio are shown in **Fig. 3-19**. The values for productivity in this case are about one half of the values obtained in the previous case, presumably because the well is considerably shorter here. As in the previous case, the error bars in Figs. 3-17 and 3-18 increase with increasing C_v up to $C_v \sim 1$. The ratio of the maximum to minimum productivity computed for the 30 realizations is about 8 in both figures at the maximum value of C_v. This high value probably results because the well length is comparable to the correlation length, which would be expected to lead to high variability in productivity results.

In this case, however, the average (homogeneous) realization provides an accurate estimate of the ensemble averaged results; i.e., PI_∞^* is very close to $\overline{PI}_\infty$ and PI_1^* is close to $\overline{PI}_1$. This is in contrast to the results for the previous system. The effects of wellbore hydraulics on productivity are relatively small in this case, as indicated in Fig. 3-19 (*PI* ratio ~ 0.95 or greater). Again, $\overline{R}$ is well approximated by R^*, indicating that a single simulation of a homogeneous system can be used to assess the effect of wellbore hydraulics on productivity.

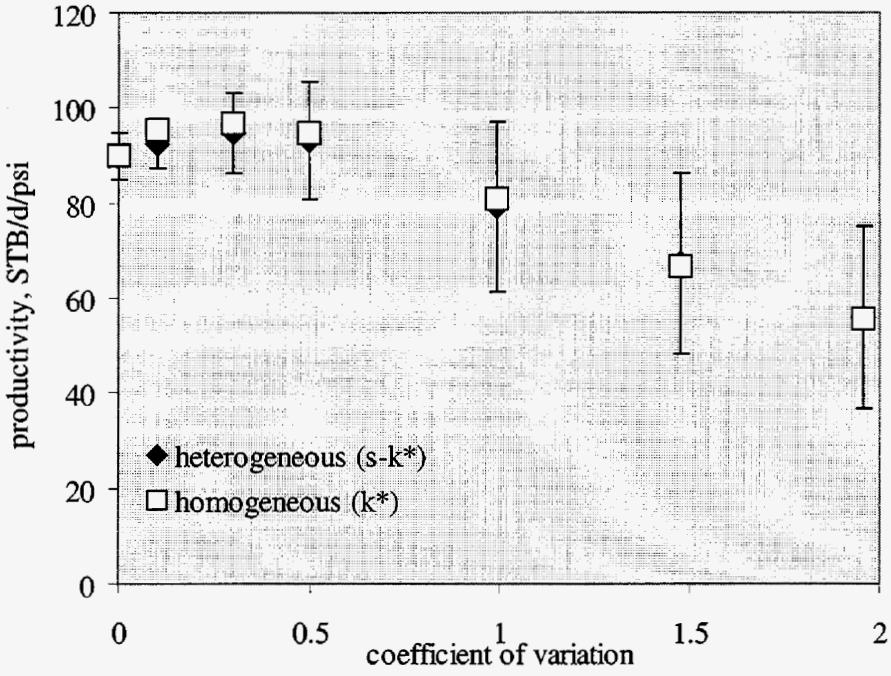

Fig. 3-17: Productivity plot (permB, wellB, infinite conductivity)

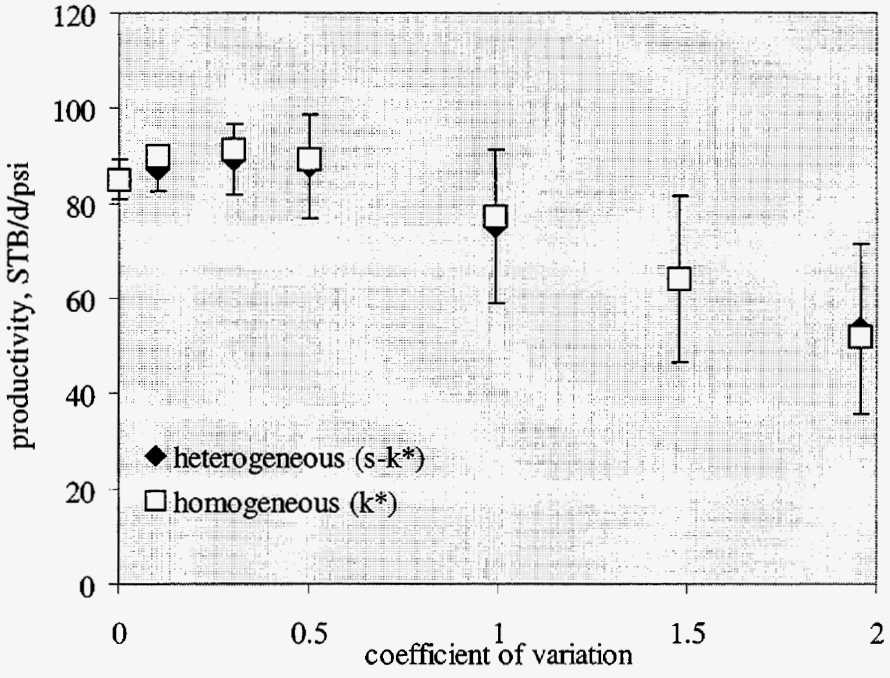

Fig. 3-18: Productivity plot (permB, wellB, finite conductivity)

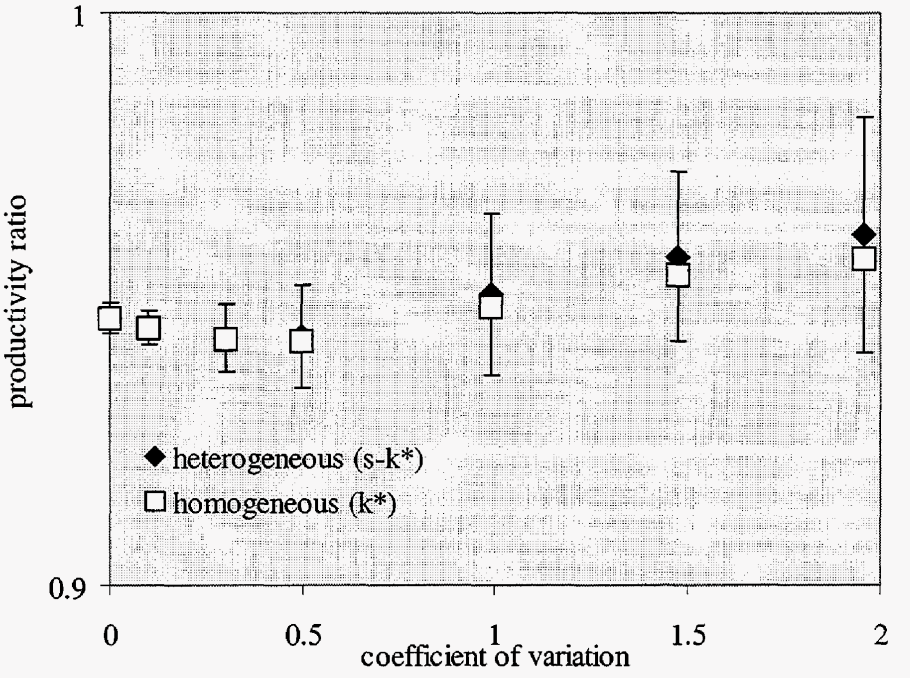

Fig. 3-19: Productivity ratio plot (permB, wellB)

3.6.3 Dual-lateral wells. Our last example involves a dual-lateral well (wellC in Table 3-3) in a permeability field of correlation structure $l_x = l_y$=0.5, l_z =0.05 (permC). In this case, the length of each lateral is slightly less than l_x. Productivity results for the dual-lateral system are shown in **Fig. 3-20** and **3-21**; productivity ratios are displayed in **Fig. 3-22**. These results again demonstrate increasing variation among the 30 realizations as C_v is increased up to $C_v \sim 1$. The ratio of the maximum to minimum productivity computed for the 30 realizations is about 3.4 in both cases at the maximum value of C_v. Even larger error bars would be expected if only one lateral were producing.

In this case, the PI_∞^* and PI_1^* results overestimate their respective $\overline{PI}_\infty$ and $\overline{PI}_1$ results, though the deviation is less than one σ_P in all cases. As in the two previous cases, the productivity ratio is accurately represented by the homogeneous case. These results, along with the results for the previous two examples, demonstrate the applicability of the overall s-$\mathbf{k}^*$ approach for studying the combined effects of wellbore hydraulics and reservoir heterogeneity on the productivity of non-conventional wells.

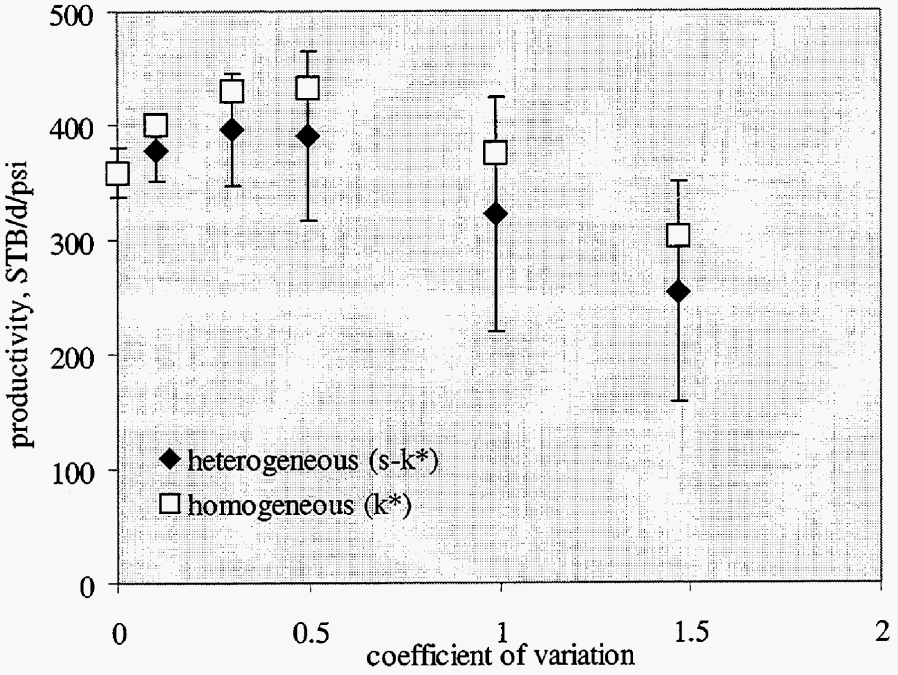

Fig. 3-20: Productivity plot (permC, wellC, infinite conductivity)

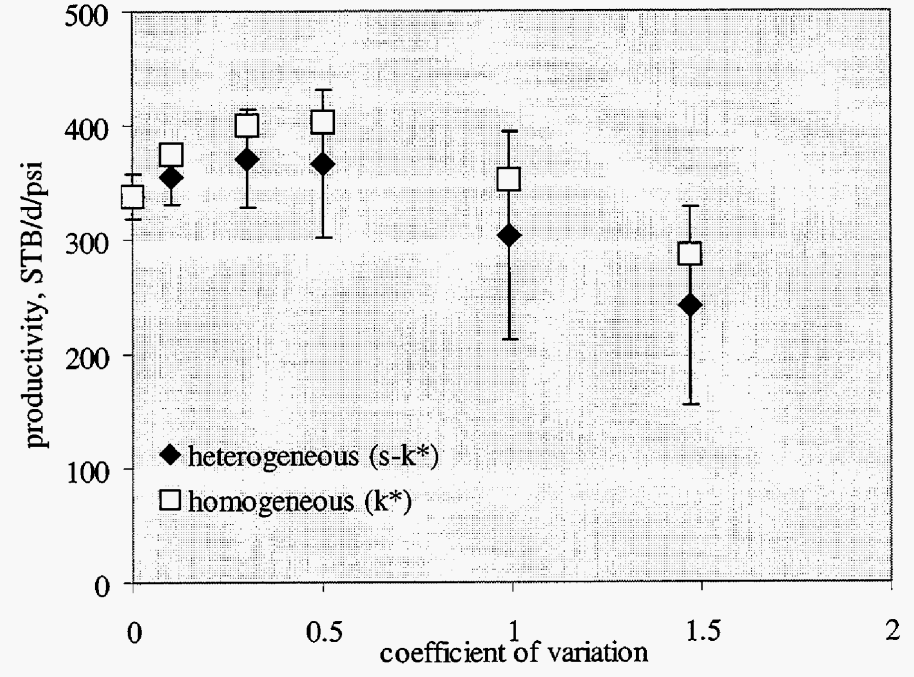

Fig. 3-21: Productivity plot (permC, wellC, finite conductivity)

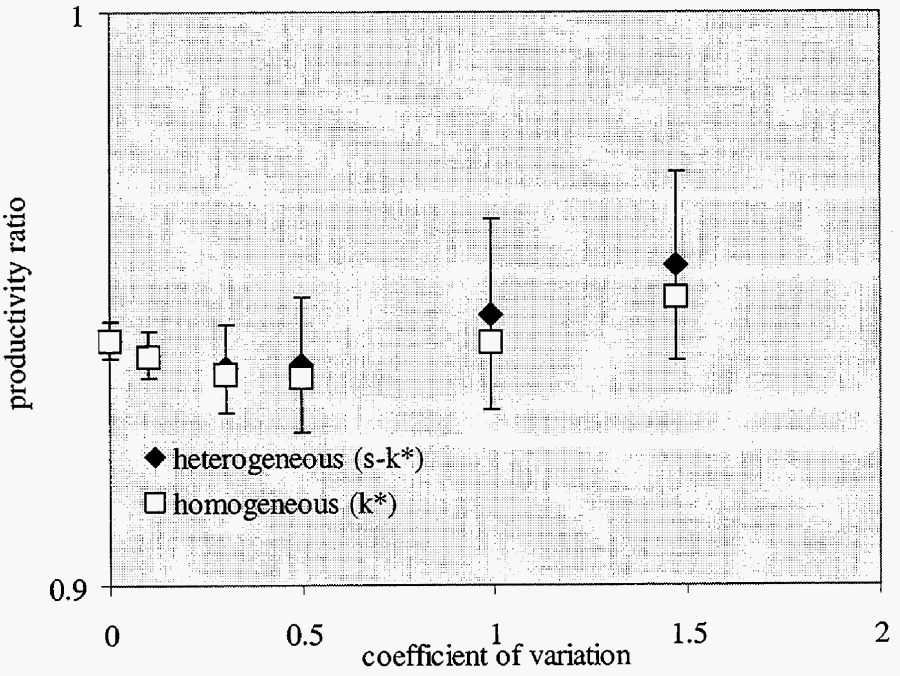

Fig. 3-22: Productivity ratio plot (permC, wellC)

3.7 Discussion and Conclusions

In this chapter, we presented an approximate method, referred to as the s-$\mathbf{k}^*$ approach, capable of providing estimates of productivity for complex wells in heterogeneous reservoirs. The method extends a previous semi-analytical approach through the introduction of a position dependent skin along the wellbore. This skin, which accounts for near-well heterogeneity, is computed from the local permeability field in the vicinity of each well segment. The background effective permeability $\mathbf{k}^*$ applied in the method accurately captures global effects. Wellbore hydraulics can also be included in the s-$\mathbf{k}^*$ model. For highly detailed permeability descriptions, the s-$\mathbf{k}^*$ approach is considerably more efficient computationally than more general methods, such as a full finite difference simulation.

The method was applied to several example cases involving various heterogeneous permeability descriptions and well geometries. Results using the new approach were shown to be of good accuracy, in terms of predicting wellbore pressure and inflow pro-

files, in comparison to reference finite difference simulation results. In addition, results using the s-$\mathbf{k}^*$ approach were seen to be considerably more accurate than those using the semi-analytical method with no skin (i.e., $\mathbf{k}^*$ only).

We applied the overall solution methodology to a study of the productivity of non-conventional wells in heterogeneous reservoirs. We computed well productivity for many realizations for a given correlation structure, enabling us to determine ensemble-averaged quantities as well as variations around these averages. Comparisons of ensemble-averaged productivities with the productivity computed from a single homogeneous field of "average" permeability $\mathbf{k}^*$ enabled us to assess the applicability of a single calculation for the determination of expected well performance. For the cases considered, this result generally overestimated the ensemble-averaged result. In some cases this overestimation was slight and in other cases it was more significant. The homogeneous permeability fields were found to be quite useful for assessing the productivity ratio of the heterogeneous realizations, where productivity ratio is defined as the productivity in the finite wellbore conductivity case to the infinite conductivity case. This indicates that a single homogeneous simulation can be used to determine the relative effect of wellbore hydraulics for multiple heterogeneous realizations.

Our data clearly show that a large variation in performance prediction is possible for the multiple realizations, even when the large scale effective permeability $\mathbf{k}^*$ is essentially the same for each realization. This finding is consistent with earlier work, particularly the study of Brekke and Thompson (1996) who additionally presented probability distributions for well performance. As has also been demonstrated in previous work, our study shows that in some cases the effects of wellbore pressure losses are significant (> 20%) while in other cases they are small (< 5%). Taken in total, our methodology and results demonstrate a clear approach for estimating the effects of wellbore pressure losses on the performance of non-conventional wells in heterogeneous reservoirs.

3.8 Future Directions

The approaches and results presented in this chapter can be extended in several important directions. Because the general method provides an efficient, semi-analytical means of

estimating well productivity, it may be well suited for use in a Simulation While Drilling capability. Simulation While Drilling, discussed in more detail in Chapter 7, requires the real time (i.e., during the actual drilling operation) estimation of well performance. Because many possible scenarios must be evaluated in order to optimize the well path and trajectory, the evaluation tool must be fast and efficient. The s-$\mathbf{k}^*$ approach is therefore a candidate for such a computation.

A second area in which the approaches described here could be applied is for the calculation of well index (*WI*), as discussed at the beginning of this chapter. This will require the linkage of the semi-analytical results with a simple single phase finite difference simulator in order to determine *WI* for each block in which the well is completed. This would then allow the direct use of the semi-analytical results in finite difference reservoir simulators.

Finally, the general approach described here can be extended to model complex wells with downhole chokes (so-called "Smart Wells"). Such wells are used to control inflow from the various zones in which the well is completed and are useful for producing from multiple reservoirs or for efficiently producing highly heterogeneous reservoirs. The extension of our method to this type of model will provide a tool capable of efficiently assessing the potential of these complex wells.

3.9 References

Ababou, R.: "Identification of Effective Conductivity Tensor in Randomly Heterogeneous and Stratified Aquifers," presented at the Fifth Canadian-American Conference on Hydrogeology, Calgary, Sept. 18-20, 1990.

Babu, D.K. and Odeh, A.S.: "Productivity of a Horizontal Well," *SPERE*, 417-21, Nov. 1989.

Basquet, R., Alabert, F.G., Caltagirone, J.P. and Batsale, J.C.: "A Semi-Analytical Approach for Productivity Evaluation of Wells with Complex Geometry in Multilayered Reservoirs," paper SPE 49232 presented at the SPE Annual Technical Conference and Exhibition, New Orleans, Sept. 27-30, 1998.

Brekke, K. and Thompson, L.G.: "Horizontal Well Productivity and Risk Assessment," paper SPE 36578 presented at the SPE Annual Technical Conference and Exhibition, Denver, Oct. 6-9, 1996.

Carslaw, H.S. and Jaeger, J.C.: *Conduction of Heat in Solids*, Oxford University Press, 510 p, 1959.

Clonts, M.D. and Ramey, H.J., Jr: "Pressure Transient Analysis for Wells with Horizontal Drainholes," paper SPE 15116 presented at the SPE California Regional Meeting, Oakland, Apr. 2-4, 1986.

Daviau, F., Mouronval, G., Bourdarot, G. and Curutchet, P.: "Pressure Analysis for Horizontal Wells," paper SPE 14251 presented at the SPE Annual Technical Conference and Exhibition, Las Vegas, Sept. 22-25, 1985.

Desbarats, A.J.: "Spatial Averaging of Hydraulic Conductivity Under Radial Flow Conditions," *Math. Geol.*, **26**, 1-21, 1994.

Deutsch, C. and Journel, A.G.: GSLIB: *Geostatistical Software Library and User's Guide*, 2nd edition, Oxford University Press, 368 p, 1998.

Durlofsky, L.J.: "An Approximate Model for Well Productivity in Heterogeneous Porous Media," *Math. Geol.*, **32**, 421-438, 2000.

Eclipse Reservoir Simulator, 96A Release, GeoQuest, Schlumberger, 1996.

Economides, M.J., Brand, C.W. and Frick, T.P.: "Well Configurations in Anisotropic Reservoirs," *SPEFE*, 257-262, Dec.1996.

Goode, P.A. and Thambynayagam, R.K.M.: "Pressure Drawdown and Buildup Analysis of Horizontal Wells in Anisotropic Media," *SPEFE*, 683-97, Dec. 1987.

Gringarten, A.C. and Ramey, H.J., Jr: "The Use of Source and Green's Functions in Solving Unsteady-Flow Problems in Reservoirs," *SPEJ*, 285-96, Oct. 1973.

Hawkins, M.F.: "A Note on the Skin Effect," Trans. AIME **207**, 356-57, 1956.

Kuchuk, F.J., Goode, P.A., Brice, B.W., Sherrared, D.W. and Thambynayagam, R.K.M.: "Pressure Transient Analysis and Inflow Performance for Horizontal Wells," paper SPE 18300 presented at the SPE Annual Technical Conference and Exhibition, Houston, Oct. 2-5, 1988.

Lee, S.H. and Milliken, W.J.: "The Productivity Index of an Inclined Well in Finite-Difference Reservoir Simulation," paper SPE 25247 presented at the SPE Symposium on Reservoir Simulation, New Orleans, Feb. 28-Mar. 3, 1993.

Maizeret, P.D.: "Well Indices for Non-Conventional Wells," Master's report, Stanford University, 1996.

Ouyang, L.-B.: "Single Phase and Multiphase Fluid Flow in Horizontal Wells," PhD thesis, Stanford University, 1998.

Ouyang, L.-B. and Aziz, K.: "A Simplified Approach to Couple Wellbore Flow and Reservoir Inflow for Arbitrary Well Configuration," paper SPE 48936 presented at the SPE Annual Technical Conference and Exhibition, New Orleans, Sept. 27-30, 1998.

Ozkan, E., Raghavan, R. and Joshi, S.D.: "Horizontal Well Pressure Analysis," *SPEFE*, 567-75, Dec. 1989.

Peaceman, D.W.: "Interpretation of Well-Block Pressure in Numerical Reservoir Simulation with Nonsquare Grid Blocks and Anisotropic Permeability," *SPEJ*, 531-43, June 1983.

Press, W.H., Teukolsky, S.A., Vetterling, W.T. and Flannery, B.P.: *Numerical Recipes in C: The Art of Scientific Computing*, 2nd edition, Cambridge University Press, 994 p, 1993.

Thomas, L.K., Todd, B.J., Evans, C.E. and Pierson, R.G.: "Horizontal Well IPR Calculations," paper SPE 36753 presented at the Annual Technical Conference and Exhibition, Denver, Oct. 6-9, 1996.

Wolfsteiner, C., Durlofsky, L.J. and Aziz, K.: "Approximate Model for Productivity of Nonconventional Wells in Heterogeneous Reservoirs, *SPEJ*, 218-226, June 2000a.

Wolfsteiner, C., Durlofsky, L.J. and Aziz, K.: "Efficient Estimation of the Effects of Wellbore Hydraulics and Reservoir Heterogeneity on the Productivity of Non-Conventional Wells," paper SPE 59399 presented at the SPE Asia Pacific Conference, Yokohama, Japan, April 25-26, 2000b.

4 Pressure Drop in the Wellbore

by Jaydeep Mahashabde, Khalid Aziz and Louis J. Durlofsky

4.1 Introduction

In many horizontal wells, particularly in high permeability reservoirs, pressure drop in the well can be important in controlling flow into the wellbore. Generally this results in higher production from zones near the heel of the well than those near the toe. In such situations it is important to be able to predict the pressure drop accurately.

This problem is different from the problem of flow in a pipe where there is no influx through the pipe wall. In horizontal and other advanced wells, fluid enters the well along its entire completed length. The well can be open-hole or it can be completed with a liner. Furthermore, the liners may or may not be cemented. The wells can have single or multiple laterals and each lateral can be several kilometers in length.

While flow in the wellbore is not always single-phase, the solution of the multiphase flow problem cannot be accomplished without first tackling the problem of single-phase flow. Almost all multiphase flow correlations employ the single-phase friction factor in one way or another.

Ouyang et al. (1998) showed that inflow causes the wall friction to increase in the laminar flow regime and decrease in the turbulent flow regime. Also, accelerational effects, which are generally neglected in pipe flow, can be significant.

A considerable amount of experimental work has been performed to study the influence of radial inflow during single-phase production. The experimental data are generally obtained by injecting fluids through perforations along the pipe wall and measuring the pressure drop at different locations along its length.

Stanford University's Horizontal Well Research Group (SUPRI-HW) has conducted experiments in collaboration with Marathon Oil Company. These experiments were carried out to study single-phase as well as two-phase flow and were performed primarily with air and water (Ouyang et al., 1998) in a 6 inch pipe with and without a liner.

Significant experimental work has also been performed at Norsk Hydro's Research Center in Porsgrunn, Norway (Schulkes and Utvik, 1998; Schulkes et al., 1999). They collected data for air, oil and water flow.

Tulsa University has also conducted a series of single-phase experiments with water as the working fluid (Yuan et al., 1999). In these experiments, pipes with different numbers of perforations were used to study the effect of perforation density.

We have previously proposed correlations based on our own and existing published data. Our objective here is to compare existing models with all available data and to improve, if necessary, the proposed models so they are in agreement with all the data. We focus here just on single-phase wellbore flow. Available models are first tested against the data. Based on these tests we have developed a simple new model which is able to provide improved predictions.

Some of this work was performed by our student, Jaydeep Mahashabde, during a summer internship at Norsk Hydro with Dr. Ruben Schulkes. The results reported in the next section are taken from the Master's report of Mahashabde (2000).

4.2 Modeling Results for Single Phase Flow in Horizontal Wells

Here we discuss the applicability of several correlations developed for single-phase wellbore flow. We first describe how pressure drop is evaluated for wellbore flow. An essential part of this calculation is the determination of friction factor for flow without influx through the pipe wall. Next we discuss friction factor correlations for pipe flow with radial influx.

The single-phase experiments conducted to collect the data used in this work are described after the calculation procedure is outlined. Then, comparisons of existing correlations with the experimental data are presented. Finally modifications to the correlations are proposed to capture the effect of perforation density.

4.2.1 Pressure Drop Calculation. For pipe flow with radial inflow, the total pressure drop along the pipe can be split into three parts, namely, gravitational, accelerational and frictional components:

$$\Delta p = \Delta p_{HH} + \Delta p_A + \Delta p_F \quad . \tag{4-1}$$

The three terms on the right hand side represent hydrostatic head, accelerational and frictional components of total pressure drop.

For the case of a horizontal pipe, the gravitational pressure drop is zero. The accelerational pressure drop arises due to wall inflow. As a result of radial inflow, the velocity of the fluid varies along the pipe length. This causes a change in the axial momentum of the fluid and the associated pressure drop is recognized as the accelerational pressure drop. For single-phase flow, Ouyang et al. (1998) suggested the following equation to calculate the accelerational pressure gradient:

$$\left(\frac{dp}{dx}\right)_A = 2\rho U \frac{dU}{dx} \quad , \tag{4-2}$$

where U is the axial velocity and ρ is the density of the fluid. This equation needs to be integrated over the length of pipe to obtain the accelerational pressure drop.

The frictional pressure drop is caused by shear stress at the pipe wall. It can be obtained by integrating the following equation

$$\left(\frac{dp}{dx}\right)_F = f_o U^2 \frac{\rho}{2D} \quad , \tag{4-3}$$

where D is the diameter of the pipe. The friction factor f_o in the above equation is a dimensionless pressure drop. If there is no inflow, this friction factor depends only on the Reynolds Number (Re) and the relative roughness (ε/D) of the internal pipe wall. This friction factor will be referred to as the *no wall inflow* friction factor, denoted by f_o. Various correlations to calculate f_o are discussed by Ouyang and Aziz (1996).

4.2.2 Friction factor with wall inflow. When steady flow in a pipe is disturbed by inflow through the pipe wall, the friction factor is altered. Furthermore, the acceleration of fluid entering the pipe requires additional energy that translates into additional pressure

drop. Additional parameters needed are the wall Reynolds Number (Re_w) and a Perforation Density Parameter (Φ):

$$\mathrm{Re}_w = \frac{\rho q}{\pi \mu} \quad , \tag{4-4}$$

where q is the volumetric inflow rate per unit length of pipe.

Since for a given inflow rate the inflow velocity will depend on the number of perforations, a perforation density parameter is defined as

$$\Phi = \frac{\omega L A_{perf}}{A_{pipe}} \quad , \tag{4-5}$$

where ω is the number of perforations per unit length and A_{perf} is the cross sectional area of an individual perforation.

Various investigators have represented data using various types of corelations. Three forms of these correlations are presented below.

Type M Correlations

Two of the correlations developed by Ouyang et al. (1998) and one developed by Schulkes et al. (1999) are similar in form. They are referred to as **M**-Type correlations:

- Correlation **M1** by Ouyang et al. (1998):

$$f = f_o\left[1 - 0.0153\,\mathrm{Re}_w^{0.3978}\right] \tag{4-6}$$

- Correlation **M2** by Ouyang et al. (1998):

$$f = f_o\left[1 - 29.03\left(\frac{\mathrm{Re}_w}{\mathrm{Re}}\right)^{0.8003}\right] \tag{4-7}$$

- Correlation **M3** by Schulkes et al. (1999):

$$f = f_o\left[1 - 26\left(\frac{\mathrm{Re}_w}{\mathrm{Re}}\right)\right] \tag{4-8}$$

The last two correlations are surprisingly similar, even though they were developed independently.

Type H Correlations

Arif (1999) used a commercial computational fluid dynamics (CFD) code to model flow with perforations. He used the results of detailed calculations to obtain friction factor correlations from regression. These correlations are presented below:

- Correlation H1 developed by Arif (1999):

$$f = f_o\left[1.9598\,\mathrm{Re}^{-0.239}\,\mathrm{Re}_w^{-0.1642}\right] \tag{4-9}$$

- Correlation H2 developed by Arif (1999):

$$f = f_o\left[1-3.34\times10^{-10}\,\mathrm{Re}^{2.25}\,\mathrm{Re}_w^{-0.1642}\right] \tag{4-10}$$

- Correlation H3 developed by Arif (1999):

$$f = f_o\left[1-\left\{-1.822+0.2246\log\mathrm{Re}+0.158\log\mathrm{Re}_w\right\}\right] \tag{4-11}$$

Type T Correlation

This correlation was developed by Yuan et al. (1999) based on experiments conducted at Tulsa University. They define a total friction factor (f_T) that includes the effects of friction and fluid acceleration:

$$\left(\frac{dp}{dx}\right) = f_T U^2 \frac{\rho}{2D} \quad . \tag{4-12}$$

The expression they obtain through regression for f_T is a polynomial of many parameters. The original reference should be consulted for details.

4.3 Experimental Data

We have used our own data (Ouyang et al., 1998) and available data from other sources. **Table 4-1** summarizes the characteristics of the data used. **Table 4-2** gives the range over which *Re* and Re_w vary in the different data sets.

Table 4-1: Sources of Data

Facility	Source	Pipe Length (m)	Diameter (m)
Liner	Stanford/Marathon (1996)	30	0.1143
PVC Pipe	Stanford/Marathon (1997a)	30	0.1574
Halliburton Liner	Norsk Hydro	6.37	0.16
Conslot Liner	Norsk Hydro	8.322	0.16
Model (Steel) Pipe	Norsk Hydro	14.03	0.15
PVC Pipe	Tulsa University	1.219	0.024

Table 4-2: Range of Flow Rates

Source	*Re*	Re_w
Stanford/Marathon	$4x10^4$-$40x10^4$	0-200
Norsk Hydro	$4x10^4$-$40x10^4$	0-250
Tulsa University	$4x10^3$-$6x10^4$	0.4-40

4.3.1 Stanford/Marathon Experiments. Stanford and Marathon Oil designed and Marathon conducted a series of experiments during the period 1993 through 1997. These experiments are described in detail by Ouyang et al. (1998). The experiments were carried out in a 100-ft long pipe at the Marathon Oil Petroleum Technology Center in Littleton, Colorado. Different combinations of axial flow and radial inflow, wellbore types, perforation types and densities, fluid types and wellbore inclination angles were considered. For comparison purposes, here we use data from 1996 and 1997 experiments (referred to as "Marathon Data" hereafter) only. The pipe used for the 1996 experiments contains twenty 5-ft sections. It contains three acrylic window sections, each about 4 ft

long, and three stainless steel pre-packed wire wrapped screen sections, each about 21 ft long. It is important to note that inflow occurs only in the liner sections so that the total inflow length is about 63 ft. The 1997 experiments were carried out using an acrylic pipe with perforation densities of 0.5, 1, 4 and 8 shots/ft. All of the perforations were aligned for experiments with perforation densities of 0.5 shots/ft and 1 shot/ft; for the other two perforation densities they were phased.

4.3.2 Norsk Hydro Experiments. Norsk Hydro has conducted wellbore flow experiments at their research center at Porsgrunn, Norway. Schulkes and Utvik (1998) and Schulkes et al. (1999) describe these experiments. The range of Reynolds numbers for these experiments is about the same as that for the Stanford/Marathon experiments. As shown in **Table 4-1**, three types of pipes were used.

The pipe with the Halliburton liner is a steel pipe with 64 perforations per meter. The diameter of each perforation is 9.5 mm. This yields a perforated area equal to 0.91% of the pipe surface area. In order to have uniform flow through each of the perforations in the liner, a ceramic insulation mat was wrapped tightly around the outside of the liner.

The pipe with the Conslot liner is constructed by wrapping a triangular wire around supporting rods which lie in a circular formation along the axis of the pipe. The base of the triangular wire is directed outwards and is typically about 3-4 mm wide. This specialized geometry imparts a very high wall roughness to the pipe and also prevents a precise estimate of the perforation density.

The model pipe has 56 radial inlets, each with a diameter of 9 mm. The spacing between adjacent inlets is 0.5 m. These radial inlets are positioned in two rows (28 inlets in each row), diagonally opposite from each other, along the length of the pipe.

4.3.3 Tulsa University Experiments. A PVC-R-4000 pipe was used in the experiments conducted at Tulsa University. The perforation densities used were 5, 10 and 20 shots/ft. The diameter of all the perforations was 3.17 mm. The perforations were uniformly distributed along the pipes with phasing of 360°, 180° and 90° respectively. Experiments were conducted for various local inflow to main flow rate ratios, ranging from 1/100 to 1/2000. More details can be found in Yuan et al. (1999).

4.4 Comparison of Correlations with Experimental Data

Figs. 4-1 to **4-6** show comparisons of the correlations presented earlier with Norsk Hydro data. Correlation **T** does not compare well against this data set, and hence we do not show the corresponding plots. This is probably because the range of Reynolds number of the Tulsa data, from which this correlation was developed, is very different from that of the Norsk Hydro data (see Table 4-2). **M**-Type correlations predict the pressure drop quite accurately (Figs. 4-1, 4-3 and 4-5). For all three pipes the data points fall within the 10% error bound using any of the three **M**-type correlations.

H-type correlations also do a good job for the model pipe (Fig. 4-2). In this case predictions fall within an error bound of 8%. A probable reason for this good match may be that these correlations were based on CFD calculations for a similar pipe. The match is not as good for the Conslot and Halliburton liners (Figs. 4-4 and 4-6). We can see that most of the predicted values are in error by about 40% for the Conslot liner and by about 80% for the Halliburton liner.

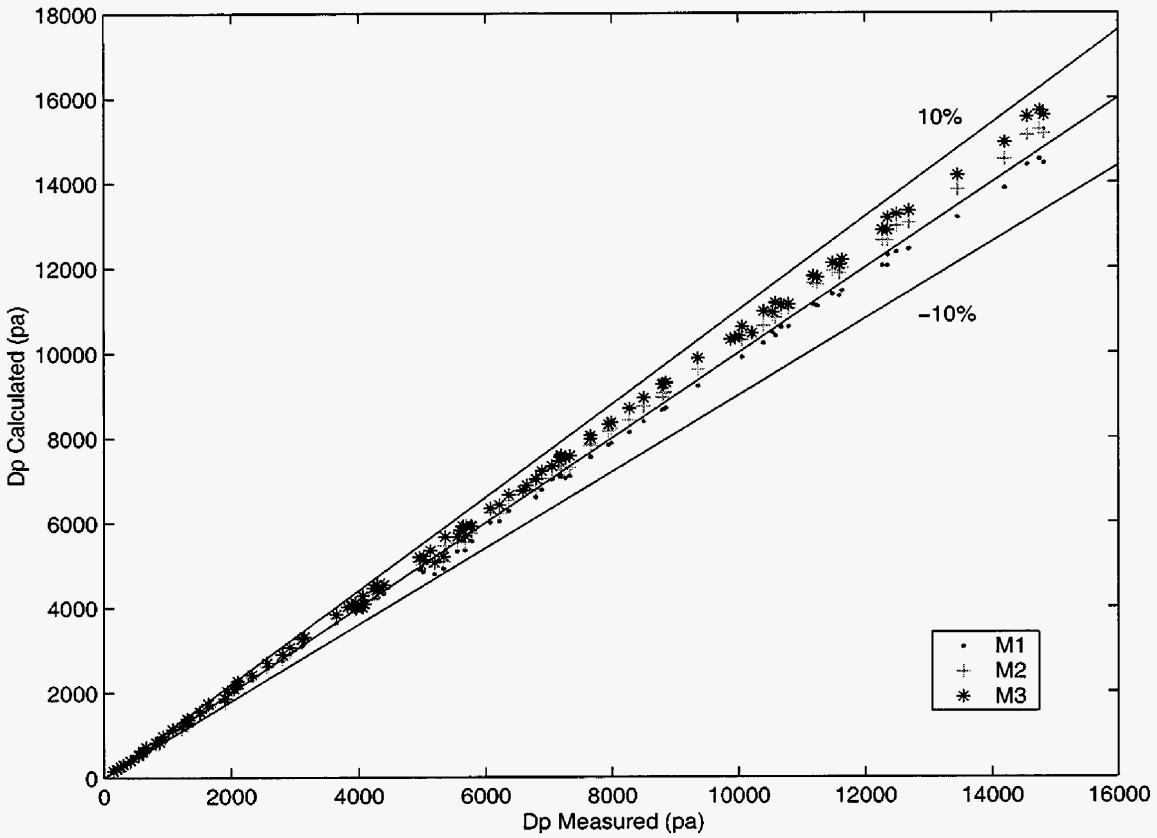

Fig. 4-1: Comparison of M-Type Correlations with Norsk Hydro Data for Model Pipe

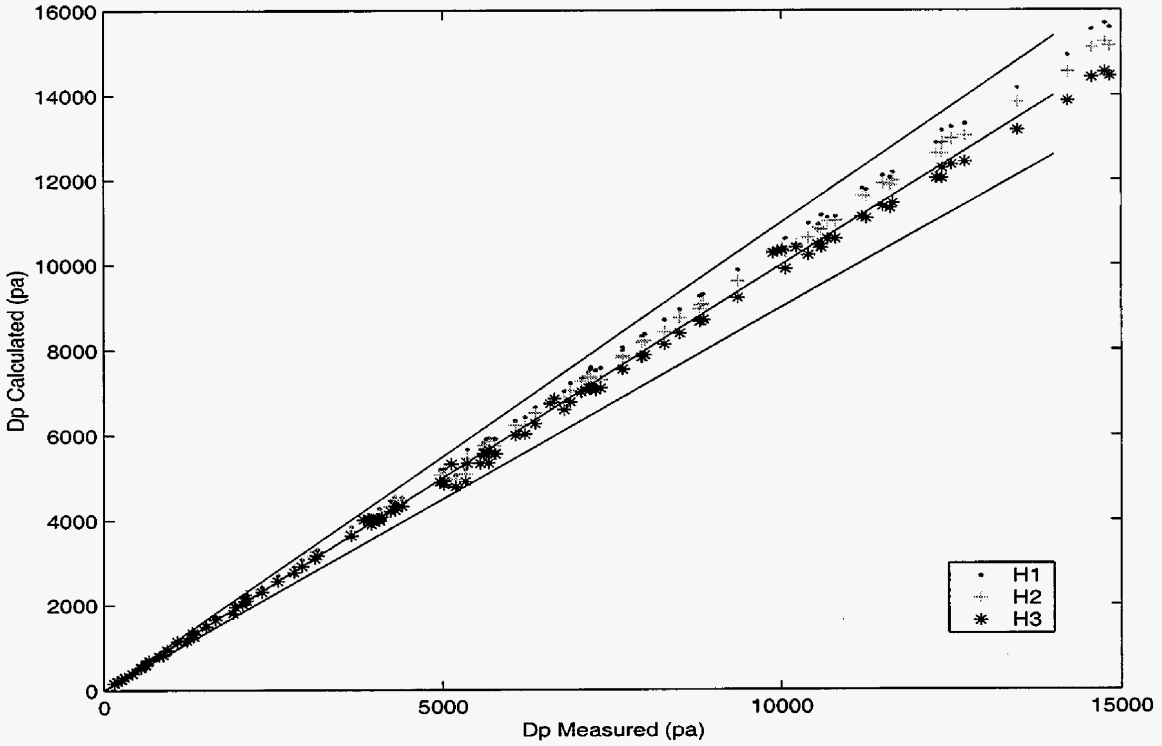

Fig. 4-2: Comparison of H-Type Correlations with Norsk Hydro Data for Model Pipe

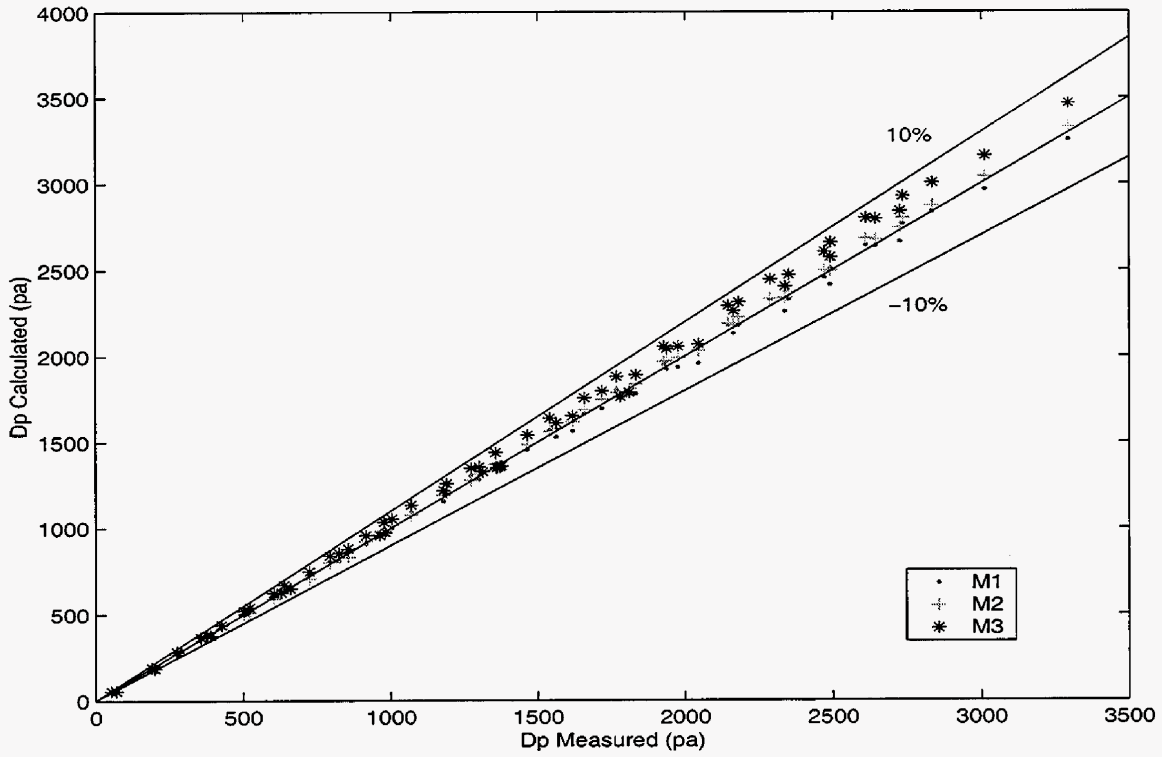

Fig 4-3: Comparison of M-Type Correlations with Norsk Hydro Data for Halliburton Liner

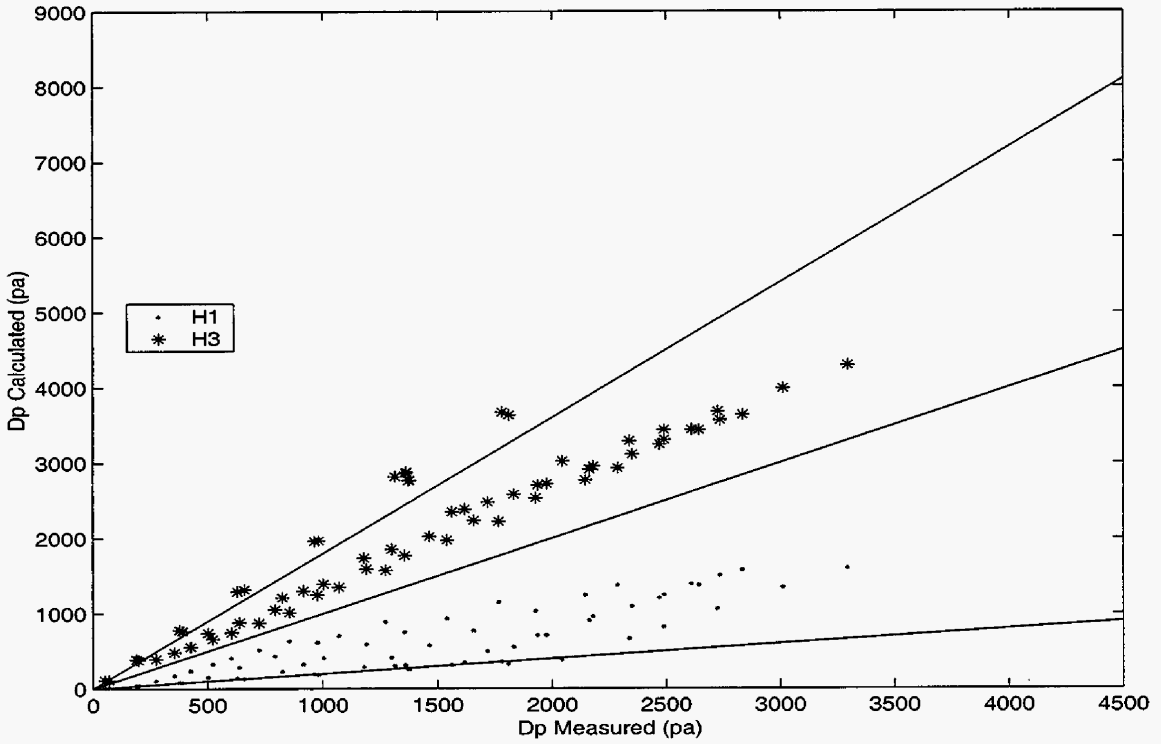

Fig 4-4: Comparison of H-Type Correlations with Norsk Hydro Data for Halliburton Liner

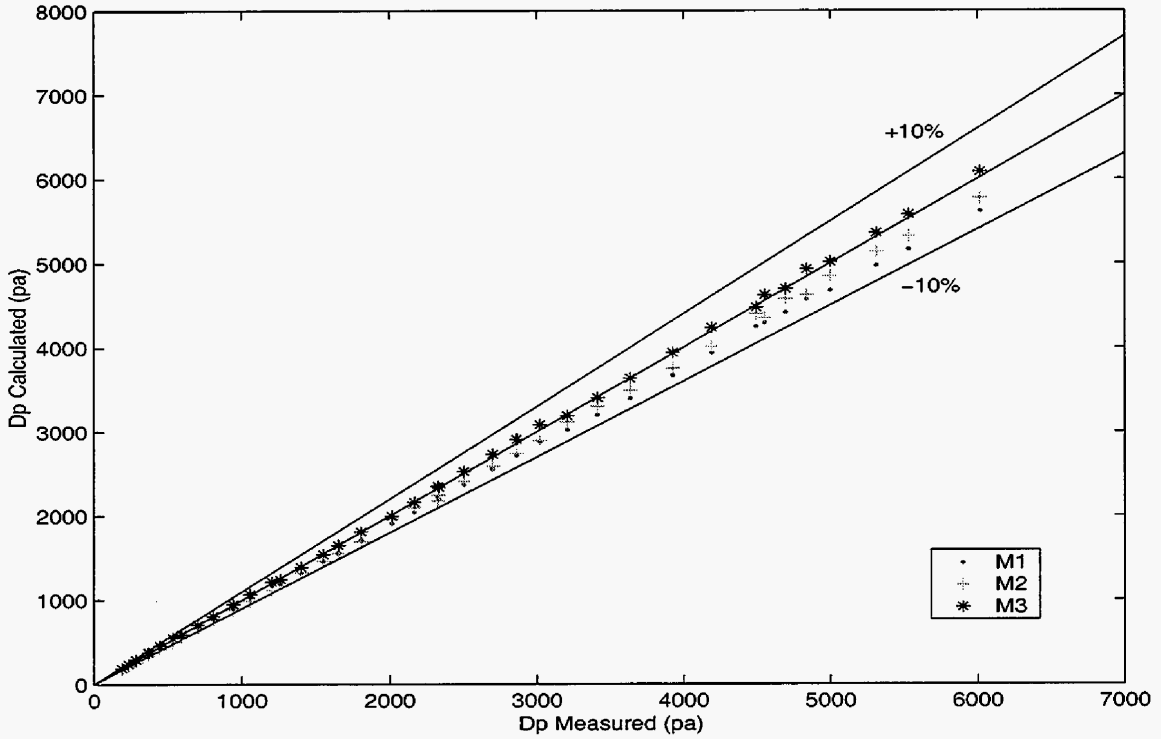

Fig. 4-5: Comparison of M-Type Correlations with Norsk Hydro Data for Conslot Liner

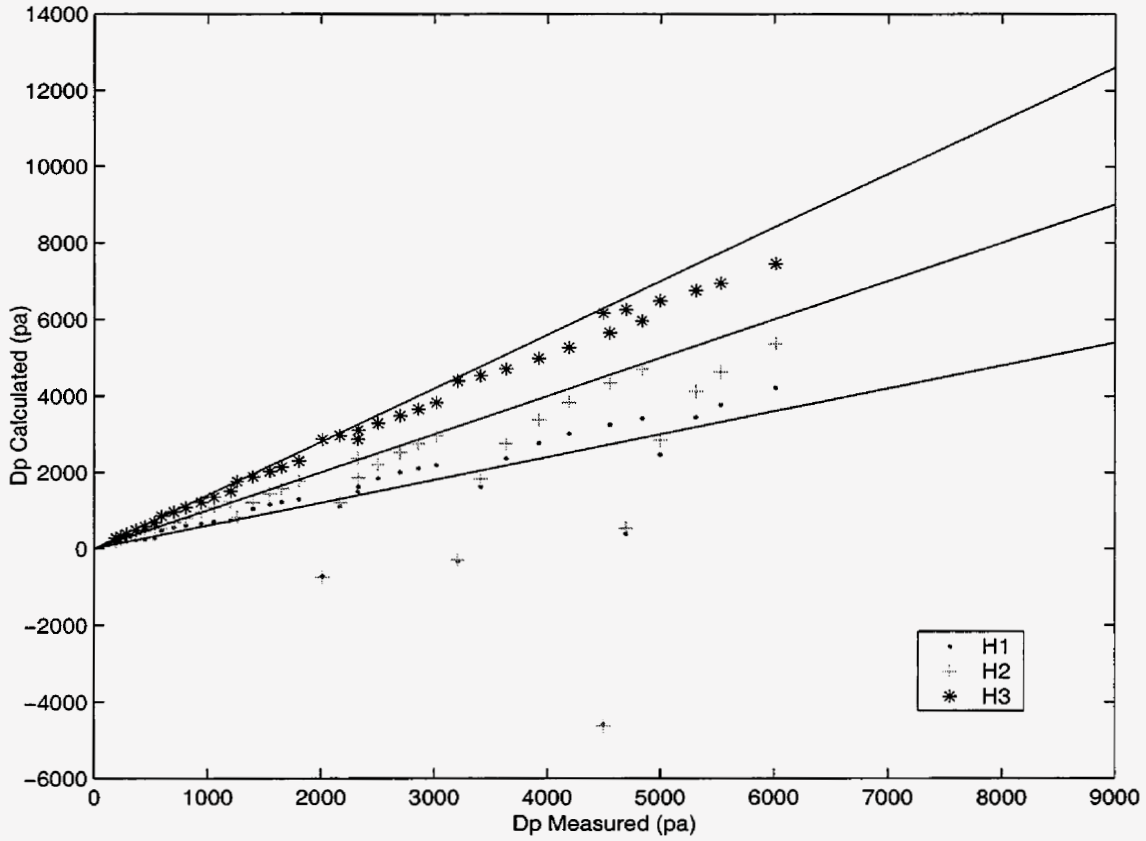

Fig. 4-6: Comparison of H-Type Correlations with Norsk Hydro Data for Conslot Liner

4.4.1 Effect of Perforation density (Φ). From the comparisons shown in the last section, we can see that correlations **M2** and **M3** compare best against the Norsk Hydro data. As stated before, these correlations represent f in the form: $f = f_o \times g(Re, Re_w)$. In fact g is a function of the ratio, Re_w/Re, referred to as γ hereafter. It was observed from Marathon and Norsk Hydro experiments that in the turbulent flow regime, $f < f_o$. This is because, with wall inflow, the time averaged velocity profile for turbulent pipe flow is altered, as discussed by Ouyang (1998). Wall inflow lifts and expands the turbulent boundary layer and thus increases the axial velocity beyond the layer, but decreases the velocity within the layer to honor mass conservation. As a consequence, the axial velocity gradient near the pipe wall, and therefore the shear stress, decrease. From this argument, we expect g to be always less than 1. Correlations **M2** and **M3**, though developed independently, are consistent with this observation. We note, however, that the correlations of **M**-Type do

not account for the perforation density. Because the Tulsa data show a strong dependency of f_T on Φ, **M1** and **M2** do not compare well against Tulsa data.

In order to account for perforation density, we studied the Tulsa University data in more detail and found that a correlation of the following type would be appropriate:

$$f = f_o\left(1 - a\Phi^b\gamma^c\right), \tag{4-13}$$

where

$$\gamma = \frac{q_{per}}{Q} \times \frac{\omega D}{4} = \frac{qD}{4Q}.$$

We see (**Fig. 4-7**) that, as expected, for all of the data from the Marathon experiments and much of the Norsk Hydro data, $f < f_o$. This condition is also satisfied for the 20 shots/ft Tulsa data. The Tulsa 10 shots/ft data show $f_o \sim f$, though the 5 shots/ft data show $f > f_o$.

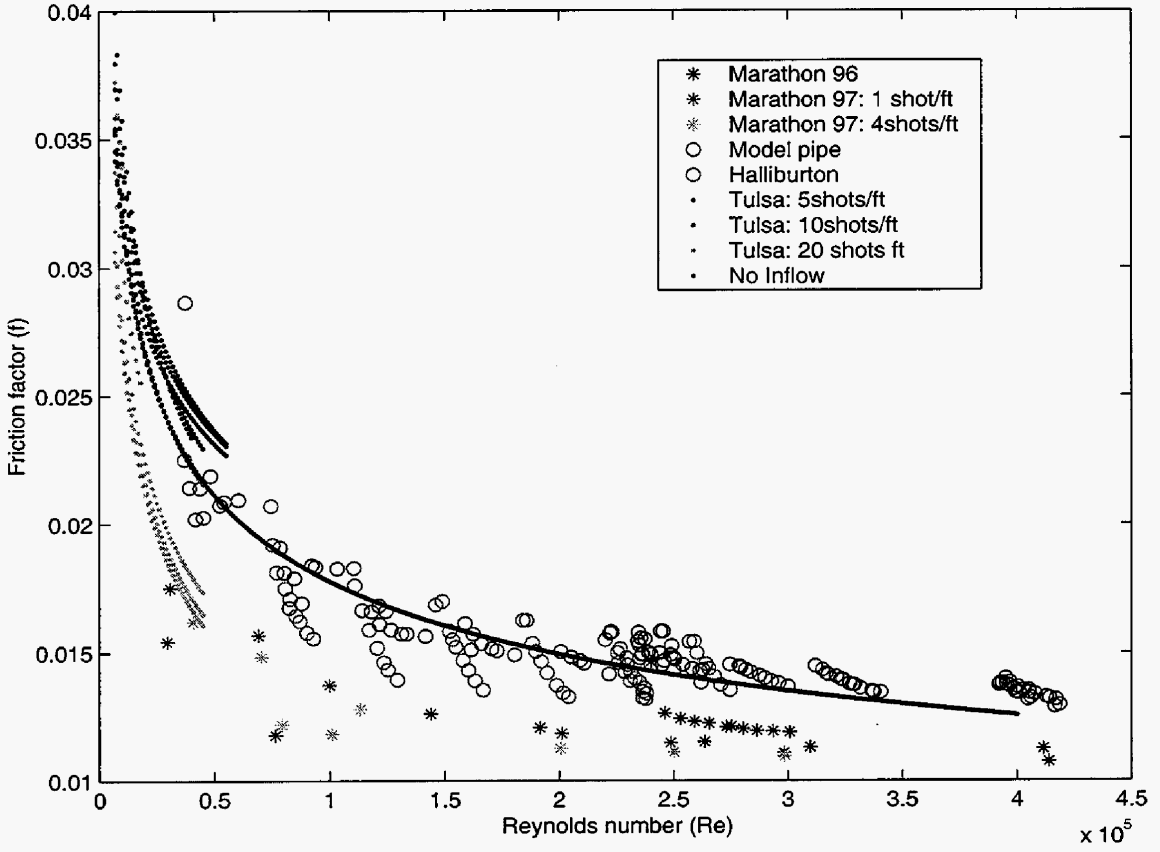

Fig. 4-7: Friction Factor for Marathon, Norsk Hydro and Tulsa Data

So, the Tulsa data for 5 shots/ft appear to be inconsistent with the other data and with theory. For this reason we only used the 10 and 20 shots/ft Tulsa data (as well as the Norsk Hydro and Stanford / Marathon data) to fit the parameters of Eq. 4-13. A very good fit was obtained with $a = 24.9$, $b = 6.5$ and $c = 0.8$.

It can be seen from **Fig. 4-8** through **Fig. 4-10** that the modified correlation compares well against the experimental data, including Marathon data. It accounts for perforation density and matches the experimental data (other than 5 shots/ft data) reasonably well. It is based on the argument that $f < f_o$ and requires only three parameters. Finally, we note that the values of parameters a and c are quite similar to the corresponding parameters in correlations **M2** and **M3**.

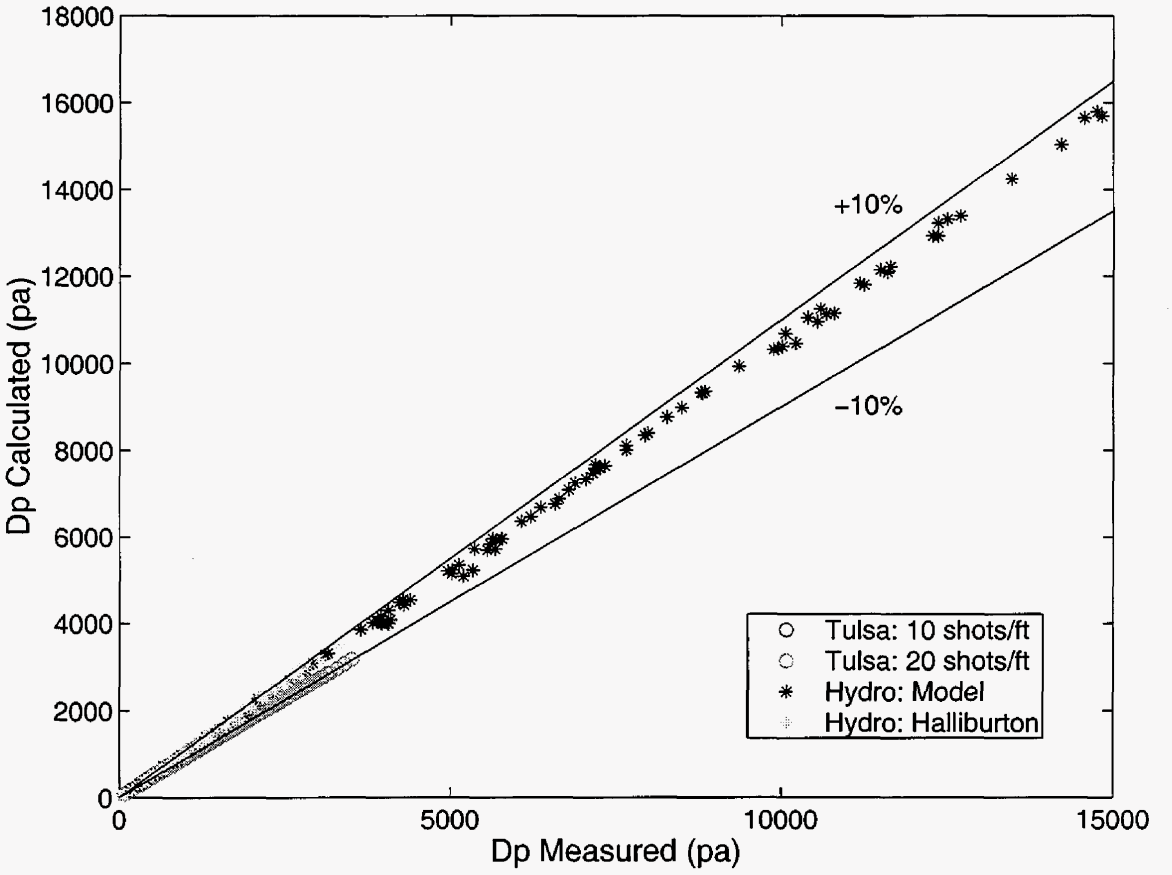

Fig. 4-8: Comparison of Eq. 4-13 with Norsk Hydro and Tulsa Data

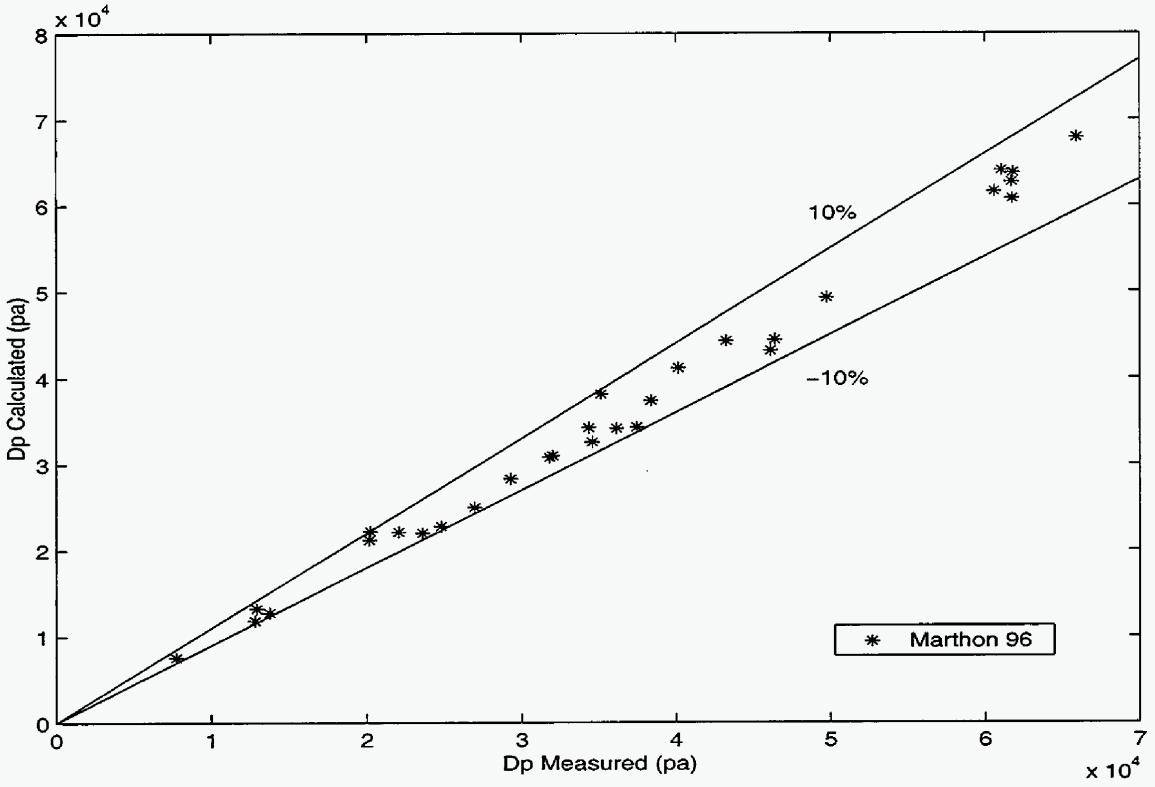

Fig. 4-9: Comparison of Eq. 4-13 with Marathon 1996 Data

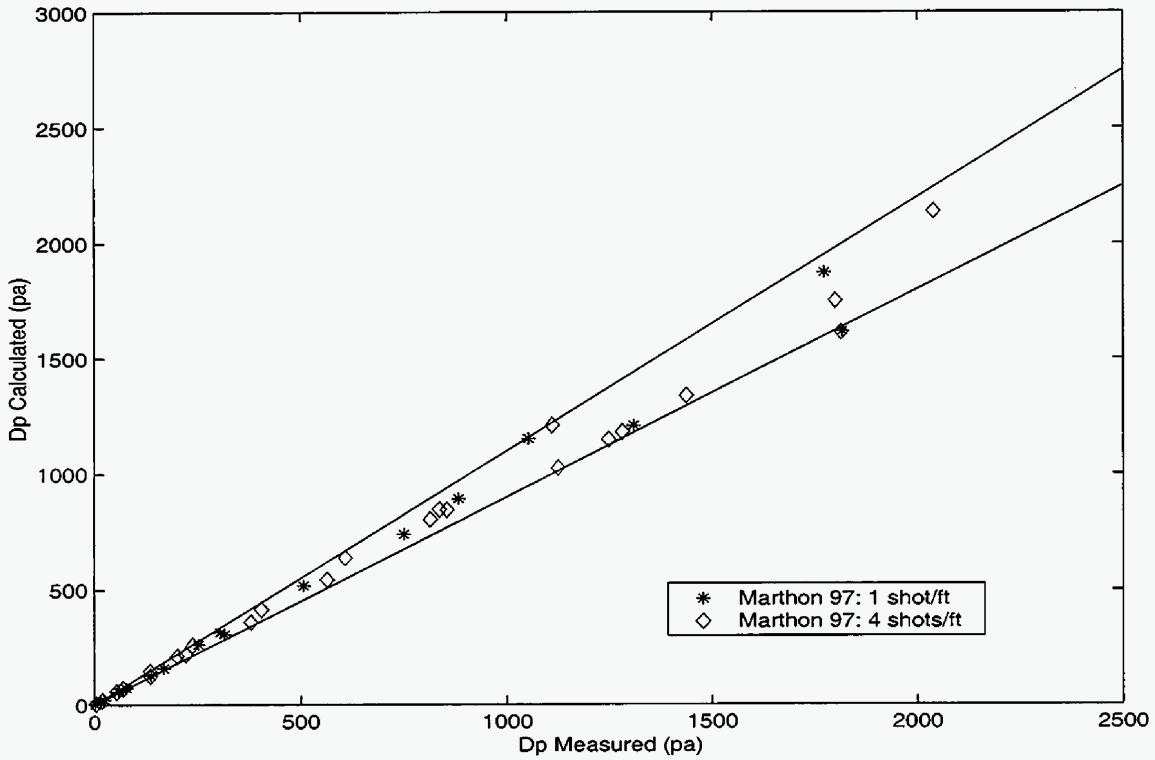

Fig. 4-10: Comparison of Eq. 4-13 with Marathon 1997 Data

4.5 Conclusions and Future Directions

Data from three different sources have been used to test existing correlations for single-phase friction factor for pipe flow with influx. Existing correlations did not fit all of the available data. A new correlation was developed. The effect of perforation density is included in the new correlation. This correlation should be suitable for calculating pressure drop in wells with influx. The correlation will be particularly useful for flow in long horizontal wells.

In the future, we plan to develop better methods for modeling two and three phase flow in horizontal and inclined wells. These approaches will be based on both mechanistic and drift-flux modeling approaches. The implementation of suitable models (i.e., accurate and computationally efficient) into a general reservoir simulator will also be addressed.

4.6 References

Arif, H.: "Application of Computational Fluid Dynamics to the Modeling of Flow in Horizontal Wells" Master's report, Stanford University, 1999.

Aziz, K. and Ouyang, L.: "Steady State Gas Flow in Pipes," *J. Pet. Sci. and Eng.*, **14**, 137-158, 1996.

Mahashabde, J. M.: "Modeling Pressure Drop in Horizontal Wells," Master's report, Stanford University, 2000.

Ouyang, L.: "Single Phase and Multiphase Fluid Flow in Horizontal Wells," PhD thesis, Stanford University, 1998.

Ouyang, L., Arbabi, S., and Aziz, K.: "A Single-Phase Wellbore Flow Model for Horizontal, Vertical and Slanted Wells," *SPEJ*, 124-133, June 1998.

Ouyang, L., Petalas, N. Arbabi, S. Schroeder, D. and Aziz, K.: "An Experimental Study of Single and Two-Phase Fluid Flow in Horizontal Wells," paper SPE 46221 presented at the 1998 SPE Western Regional Meeting, Bakersfield, CA, May 10-13.

Schulkes, R., Rinde, T., and Utvik, U.: "Pipe Flow with Radial Inflow: Experimental and Modeling Work," *J. Fluid Eng.*, 106-111, 1999.

Schulkes, R. and Utvik, U.: "Pressure Drop in a Perforated Pipe with Radial Inflow: Single Phase Flow," *SPEJ*, 77-85, March 1998.

Yuan, H., Cem, S., and Brill, J.: "Effect of Perforation Density on Single-Phase Liquid Flow Behavior in Horizontal Wells," *SPE Prod. and Facilities*, **14**, 203-209, 1999.

Nomenclature

A	Cross sectional area of pipe, m^2
A_{perf}	Cross sectional area of a single perforation, m^2
A_{pipe}	Surface area of the pipe, m^2
d	Diameter of a single perforation, m
D	Diameter of pipe, m
f	Friction factor
f_o	No wall inflow friction factor
f_T	Total friction factor
L	Pipe length, m
p	Pressure, $kg/m\text{-}sec^2$
Re	Axial Reynolds number
Re_w	Wall Reynolds number
q	Radial inflow-rate per unit length of the pipe, $m^3/m\text{-}sec$
q_{per}	Radial inflow-rate through a single perforation, m^3/sec
Q	Volumetric flow rate, m^3/sec
U	Axial velocity, m/sec
Δp_{HH}	Pressure change due to hydrostatic head
Δp_A	Pressure change due to acceleration
Δp_F	Pressure drop due to friction
γ	Ratio of inflow and axial Reynolds Numbers

Part III. Novel Approaches to Account for Heterogeneities in the Vicinity of Non-Conventional Wells

Reservoir heterogeneity can significantly affect the performance of non-conventional wells. The effects of near-well heterogeneity were clearly demonstrated for single phase flow problems (within the context of semi-analytical modeling) in the results presented in Chapter 3. To efficiently simulate general reservoir flow (e.g., multiphase flow), however, modeling approaches within a finite difference context are required.

In Chapter 5, we present a general technique for upscaling in the vicinity of horizontal wells (this work also appeared in Mascarenhas and Durlofsky, 2000). This technique is applicable to finite difference reservoir simulators and provides accurate coarse scale models that can be used to simulate one, two and three phase flow. In Chapter 6, we present a simplified approach, still within a finite difference context, for modeling the effects of near-well heterogeneity in two phase flow problems.

5 Accurate Coarse Scale Simulation of Horizontal Wells in Heterogeneous Reservoirs

by Oscar Mascarenhas and Louis J. Durlofsky

5.1 Introduction

The accurate finite difference modeling of flow due to horizontal wells continues to pose several challenges. One important aspect of horizontal well modeling is the accurate representation of fine scale reservoir heterogeneity in the near-well region in flow models. This issue arises because geological/geostatistical models typically include far more detail than can be accommodated in conventional reservoir simulation models. The disparity between the geological model (which may include $O(10^7)$ cells or more) and the simulation model (which can handle $O(10^5)$ cells) requires the use of coarsening (or upscaling) techniques.

The objective of this work is to develop and apply an upscaling approach appropriate for the generation of coarse scale simulation models of horizontal wells. This will allow for the accurate coarse scale simulation of horizontal well performance in heterogeneous reservoirs. To accom-

plish this upscaling, an appropriate local (i.e., limited domain) flow problem and boundary conditions are clearly defined. The solution of this local fine grid problem, coupled with an appropriate post-processing (averaging) of the fine grid results, provides coarse scale equivalent grid block parameters for use in the global, coarse scale simulation model. In some cases the accuracy of the coarse scale description can be further improved by 'optimizing' the coarse grid parameters. This is accomplished by applying an optimization procedure to minimize the difference between the local fine scale solution and the solution of the analogous coarse grid problem.

This work complements earlier studies directed toward the calculation of equivalent grid block permeability tensors for heterogeneous systems in regions away from flowing wells (see e.g., Durlofsky, 1991; Pickup et al., 1994 and reviews by Wen and Gomez-Hernandez, 1996 and Renard and de Marsily, 1997). Aziz et al. (1999) demonstrated the inaccuracies that can be observed when these standard coarsening techniques (i.e., no specialized upscaling in the near-well region) are applied to horizontal well problems. Specifically, they observed significant differences in primary production results between fine and coarsened simulation models of three phase flow in complex, heterogeneous reservoirs. Their work demonstrates that the use of standard upscaling procedures can be inappropriate for problems involving horizontal wells.

Previous papers addressing upscaling in the region near vertical wells (Ding, 1995; Durlofsky et al., 1999) and recent work by Muggeridge et al. (1999) on upscaling with horizontal or deviated wells, are also relevant to this study. In all of these papers, coarse grid flow models in the near-well region were developed through solution of well-driven flow problems on the fine scale and the subsequent calculation of well indexes and modified well-block transmissibilities. The details of the methods differ, though they all display significant improvement over standard techniques. Soeriawinata et al. (1997) presented an analytical approach for computing well block effective permeabilities. This approach is highly efficient, though it would be expected to be less accurate than the numerically based techniques for highly heterogeneous systems.

The present work differs somewhat from that of Ding (1995) and Ding and Urgelli (1997). Here, specific local flow problems involving a single well are defined and solved to determine the coarse grid near-well parameters. In Ding's work, by contrast, the specific local problem (or set of such problems) to be solved is not explicitly specified. In practice, the local problem would likely include the well in question and some number of neighboring wells (Lemouzy, 1997). In

this case, the method presented here specifies a smaller local problem in general, which renders the method more efficient computationally.

The local problems solved here, and the subsequent optimization, differ from the approach taken by Durlofsky et al. (1999), who considered only vertical wells and could therefore solve more limited local problems without parameter optimization. In fact, none of the earlier approaches force the detailed agreement between the local fine and coarse grid solutions as is done in the current method. Muggeridge et al. (1999) consider the solution of global fine grid problems as well as the solution of local flow problems for the calculation of the near-well parameters. Their local solution approach shares some similarities with the methodology presented here. The two approaches will be further compared following the description of the new method.

This chapter proceeds as follows. In section 5.2 the general approach for upscaling in the vicinity of horizontal wells is presented. The solution of the local fine grid problem and the post-processing and optimization to obtain coarse scale parameters are described. In section 5.3, results from coarse scale simulations of horizontal well performance, for both single and three phase flow problems, are compared to the fine scale flow results. The near-well upscaling approach is shown to improve the coarse scale models in all cases considered. In some cases, this improvement is quite substantial.

5.2 Near-Well Upscaling Methodology

The approach for upscaling in the near-well region is presented in this section. The starting point is a finely gridded, highly detailed geological model. The intent is to generate a coarsened model suitable for flow simulation that maintains the geologic realism of the fine grid model to the extent possible. The fine grid model is considered to be a single realization drawn from an ensemble of geostatistical realizations. As such, each particular realization is treated as a purely deterministic entity; i.e., there is no uncertainty associated with the fine grid permeability field. The specific objective here is in generating coarse scale models of the subsurface suitable for use in models involving horizontal wells.

5.2.1 Local Fine Grid Flow Problem. The method is developed through a consideration of single phase incompressible flow, although the approach will be applicable to more general multi-

phase problems. The governing fine scale equation is the single phase pressure equation formed by combining Darcy's law with conservation of mass (with all quantities dimensionless):

$$\nabla\cdot(\mathbf{k}\cdot\nabla p)=-q \ . \tag{5-1}$$

Here, p is pressure, $\mathbf{k}$ is the permeability tensor which is typically highly variable in space, and q is the source term. Equation 5-1 can be solved for pressure once boundary conditions and the source term are specified. From this solution the Darcy velocity ($\mathbf{u}$) is determined:

$$\mathbf{u}=-\mathbf{k}\cdot\nabla p \ . \tag{5-2}$$

Standard upscaling procedures (Durlofsky, 1991; Pickup et al., 1994; Wen and Gomez-Hernandez, 1996; Renard and de Marsily, 1997) retain the form of Eqs. 5-1 and 5-2 on the coarse grid but introduce coarse scale equivalent grid block permeability tensors ($\mathbf{k}^*$) in place of $\mathbf{k}$. The $\mathbf{k}^*$ for each coarse scale block is computed through the solution of a local flow problem over the fine scale region corresponding to the coarse grid block. This problem is usually solved subject to boundary conditions that are essentially linear in pressure (e.g., periodic or constant pressure – no flux boundary conditions). This type of approach is generally adequate in regions away from the well.

Near flowing wells, particularly when the permeability field is highly variable over small distances, the local pressure field will not be linear. Therefore, the imposition of boundary conditions linear in pressure could introduce significant inaccuracy in the coarse scale description. In the near-well region, the coarse scale parameters are, therefore, more accurately determined by the solution of a local fine scale problem with flow driven by the actual well. This is the type of fine grid problem that will be solved to generate the coarse scale model in the near-well region.

There is another distinction between the present method and standard approaches for upscaling in regions away from wells. In most upscaling methods, the local problem solved for the calculation of $\mathbf{k}^*$ contains only the fine grid blocks corresponding to the single coarse block. However, in the near-well upscaling approach presented here (and in other methods developed for this problem), the flow domain is expanded to include neighboring regions around the well. This introduces some additional computation, though the overall upscaling method still repre-

sents a very small overhead relative to the ultimate multiphase, time-dependent, global flow simulation.

A cross section (perpendicular to the axis of the horizontal well) of the flow domain for the near-well solution is shown schematically in **Fig. 5-1.** Finer grid lines correspond to the fine grid and heavier lines to the coarse grid. The domain actually used is fully three dimensional and contains the entire well in addition to surrounding regions. In the figure, the well is completed in the central grid block as shown. The domain included in the local fine grid solution includes the regions corresponding to the coarse grid well block and some number of surrounding coarse grid blocks (in x, y and z). The fine grid region is referred to as near-well[1], if one 'ring' of coarse grid cells around the well block is included (the shaded region in the figure corresponds to near-well[1]). When two rings of cells around the well block are included the fine grid region is referred to as near-well[2] (the full domain in Fig. 5-1). For a horizontal well completed in five coarse blocks (5×1×1), each of which is comprised of 3×3×3=27 fine blocks, the local fine grid problem to be solved will contain 7×3×3×27=1701 cells for near-well[1] and 9×5×5×27=6075 cells for near-well[2]. Note that, for wells completed in many coarse scale blocks, enhanced efficiency could be obtained by subdividing the local problem into two or more sub-problems. This will result in a reduction in computation but could lead to some degradation in accuracy.

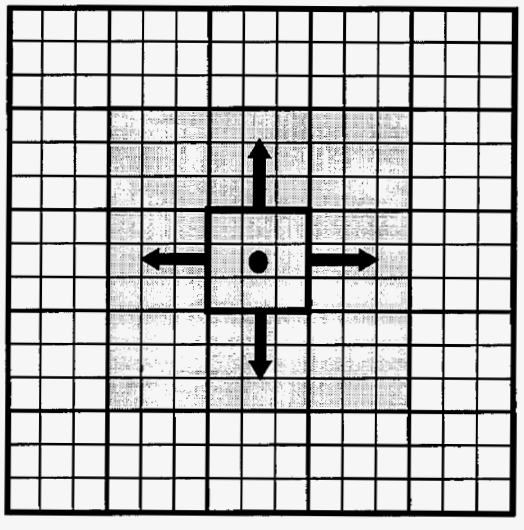

Fig. 5-1: Schematic showing cross section of the near-well[1] (shaded) and near-well[2] fine and coarse grid regions.

Equation 5-1 is solved over the fine scale region defined above. The wellbore pressure (p_{wb}) is set to 1 and the pressure on the domain boundaries to zero. This is the source and boundary specification used previously for the vertical well case by Durlofsky et al. (1999). Variation of these boundary conditions was found to have only a small effect on the coarse scale parameters computed from this solution, particularly for near-well[2]. The fine grid solution is accomplished using a standard finite difference procedure, with transmissibilities computed using harmonic averaging of the appropriate component of permeability; e.g., for the transmissibility (in the x-direction) between cells i,j,k and $(i+1,j,k)$:

$$T_{i+1/2,j,k} = \frac{2k_{i,j,k}k_{i+1,j,k}\,\Delta y\Delta z}{(k_{i,j,k}+k_{i+1,j,k})\Delta x} \quad , \tag{5-3}$$

where k here refers to the x-component of permeability and Δx, Δy, Δz are the grid block sizes in the x, y, and z-directions. Note that transmissibility relates the flow rate, from block i,j,k to block $i+1,j,k$, to the discrete pressure difference between the cells; i.e.,

$$q_{i+1/2,j,k} = T_{i+1/2,j,k}(p_{i,j,k} - p_{i+1,j,k}) \quad , \tag{5-4}$$

where $q_{i+1/2,j,k}$ is the flow rate between blocks i,j,k and $i+1,j,k$ and $p_{i,j,k}$ and $p_{i+1,j,k}$ are the grid block pressures.

Analogous expressions define $T_{i,j+1/2,k}$ and $T_{i,j,k+1/2}$. The resulting linear system can be written as **Ap=b**, where **A** is a banded matrix (seven diagonals for the three dimensional problem), **p** represents the unknown pressures and **b** is the right hand side vector.

The well flow rate, well block pressure and the wellbore pressure for the local fine grid problem are related through the well index WI; i.e.,

$$q = WI(p_{wb} - p_{i,j,k}) \quad , \tag{5-5}$$

where $p_{i,j,k}$ is the well block pressure. In the case of a well flowing at fixed pressure, inserting this representation for q in Eq. 5-1 yields a contribution to **b** and a contribution on the main diagonal of **A**. The well index for the horizontal well (on the fine grid) is computed using a standard procedure (Peaceman, 1983), though alternate procedures could also be used. Following the

solution of the local fine grid problem, the flow rates through each of the grid block faces are computed by Eq. 5-4.

5.2.2 Local Coarse Grid Flow Problem. The fine grid solution provides pressures at the grid block centers and the flow rates through each of the well block faces. The grid block pressures are then averaged from this solution over regions corresponding to coarse grid blocks. A bulk volume weighting is used in this averaging process. In addition, the flow rates are summed from the fine grid solution over regions corresponding to the faces of the coarse blocks. The average of the fine grid pressures over a coarse scale well block is designated p_c; the average of the fine grid pressures over blocks adjacent to the coarse scale well block is designated as $p_{c,n}$. The quantity q_f represents the total flow rate through the fine grid region corresponding to the face between coarse blocks c and c,n and q_0 represents the total flow rate from the well into the coarse scale well block.

The coarse scale quantities to be computed are the well index (WI^*) and the transmissibilities between the well blocks and adjacent coarse grid blocks (referred to as T_w^*). From the averaged variables defined above, these quantities can be readily calculated through equations of the form of Eqs. 5-4 and 5-5:

$$T_w^* = q_f / (p_c - p_{c,n}) \quad , \tag{5-6}$$

$$WI^* = \frac{q_0}{(p_{wb} - p_c)} . \tag{5-7}$$

More details on the calculation of WI^* and T_w^*, for the case of vertical wells, are provided by Durlofsky et al. (1999).

For the case of a horizontal well aligned along a coordinate direction, the following coarse grid quantities are calculated. For each coarse block in which the well is completed, a WI^* (linking the wellbore to the well block) and four or five T_w^* (linking the well block to all adjacent blocks not containing the well) are computed. For the other connections (which link the well block to adjacent well blocks), the appropriate component of $\mathbf{k}^*$ is used; that is, this transmissibility is not computed from the solution of the well-driven flow problem. In limited tests, the

overall coarse scale flow results did not appear to be sensitive to the specific treatment of the well block to well block transmissibility. Note that, in all cases (e.g., even when the local fine grid solution is over the near-well[2] region), only the transmissibilities linking well blocks to adjacent blocks are modified. All other transmissibilities in the coarse model are computed using the $\mathbf{k}^*$ computed from the solution of linear flow problems.

The averaging procedure described above provides accurate coarse scale simulation results in many cases. In some cases, however, an improvement in the accuracy of the coarse scale model can be obtained through use of an optimization procedure. The degradation in accuracy observed for the averaging procedure may be due to the high aspect ratios ($\Delta x/\Delta z$ or $\Delta y/\Delta z$) of the cell faces intersected by the horizontal well, coupled with the high levels of heterogeneity present (high variation over small distances in the z-direction). This can act to reduce the accuracy of the procedure used to estimate coarse grid pressures from averages of fine grid pressures. Specifically, the p_c and p_{cn} in Eqs. 5-6 and 5-7, computed from the averaging procedure, may not always agree closely with the pressures computed via solution of the corresponding coarse grid problem. This in turn can lead to some inaccuracy in the coarse grid quantities of interest, WI^* and T_w^*.

To improve the accuracy of the coarse grid model, an optimization procedure was implemented to minimize the difference between the local fine and coarse grid solutions. This is accomplished by optimizing the WI^* and T_w^* such that the differences between the coarse grid flow rates (through each well block face) and the corresponding integrated fine grid flow rates are minimized. These flow rates are indicated by the arrows pointing out of the well block in Fig. 5-1. The objective function E is defined as:

$$E = \left(\sum^{nwbs} \sum^{nfaces} \left(q_c - q_f \right)^2 \right) , \tag{5-8}$$

where q_c designates the coarse grid flow rates, q_f the fine grid flow rates (summed over the appropriate region), *nwbs* designates the number of coarse grid blocks in which the well is completed and *nfaces* the number of grid block faces in each block through which flow rate is computed (*nfaces* = 4 or 5). The objective function E is minimized over α, where α designates the WI^* and T_w^* in all coarse scale blocks containing the well and α^* represents the set of parameters

that minimizes Eq. 5-8. The minimum in E will occur when ∇E (gradient with respect to α) is driven to zero.

This fully coupled problem is solved by iterating on α using a Gauss Newton optimization algorithm. The Gauss Newton method is a gradient based procedure and derives from a Taylor series expansion of the objective function E about the previous estimate for α (designated α^k). At each iteration, an equation of the form

$$\mathbf{H}_{GN}\Delta\alpha = -\nabla E \quad , \tag{5-9}$$

is solved, where $\mathbf{H}_{GN}$ is the Gauss Newton Hessian matrix; i.e., the Hessian matrix modified to guarantee a direction of descent and eliminate the need for calculating second derivatives, and $\Delta\alpha = \alpha^{k+1} - \alpha^k$. The elements of ∇E and $\mathbf{H}_{GN}$ are computed numerically using a forward difference approximation. Each row of $\mathbf{H}_{GN}$, and each element of ∇E, requires the solution of the coarse grid near-well problem with one of the $(WI^*,\ T_w^*)$ parameters perturbed (for a total of about $5 \times nwbs$ coarse grid solutions at each iteration).

In order to minimize the number of iterations, some additional features are introduced into the optimization algorithm. These include the use of a line search to find the optimum α in the direction of descent and the use of penalty functions and step length control to constrain parameters to physically reasonable values. Scaling is also introduced to prevent $\mathbf{H}_{GN}$ from becoming ill-conditioned or singular and the Marquardt method is used to convert a semi-positive definite Hessian to one that is positive definite. Using this overall optimization procedure, the optimum is usually achieved in about 4-6 iterations of the coupled system. This is not overly time consuming (requiring about the same amount of computation time as the solution of the local fine grid problem, for the cases considered) because these iterations involve only coarse grid solutions. For further details on the construction of $\mathbf{H}_{GN}$ and the overall optimization procedure, see Gill et al. (1981), Bard (1974), and Mascarenhas (1999).

The implementation of the overall near-well scale up method can be verified through application of the method to a highly simplified problem involving a fully penetrating vertical well in a homogeneous, isotropic system of constant Δx (with $\Delta x = \Delta y$) and constant Δz on the fine scale. In this case, the near-well upscaling should provide coarse scale well indexes and transmissibilities that closely approximate those computed directly using the appropriate expressions for ho-

mogeneous systems (using the coarse grid block dimensions). Specifically, the transmissibilities should be well approximated by Eq. 5-3 and the well index should be approximately equal to the Peaceman (1983) index:

$$WI = \frac{2\pi k \Delta z_c}{\ln(r_o / r_w)}, \tag{5-10}$$

where k is the homogeneous permeability, Δx_c and Δz_c are the coarse block dimensions, $r_0 \sim 0.2\Delta x_c$ and r_w is the wellbore radius. Other, more general (e.g., layered) problems can also be used to verify the overall implementation.

Before presenting simulation results using the new near-well upscaling method, it is of interest to compare this method to the work of Muggeridge et al. (1999). Muggeridge et al. consider two approaches: the more computationally demanding requires the separate solution of the full fine grid problem for each flowing well in the reservoir and the subsequent calculation of the coarse grid WI^* and T_w^*. This procedure is shown to provide quite accurate coarse scale descriptions, though it is time consuming and may be impractical for very detailed fine grid descriptions (although presumably a smaller, sub-global, computational domain would be used in such cases). Their second approach (which they refer to as a "reduced computational domain") is, using the terminology introduced above, a near-well[1] fine scale solution with averaging (i.e., no optimization). Using this approach, they obtain results that are better than those using the standard coarse grid model (no near-well upscaling) but not as good as those obtained when the coarse scale parameters are computed from the full fine grid solution.

As shown in section 5.3, the findings of Muggeridge et al. are consistent with the results presented in this work. Specifically, clear improvement is observed in going from near-well[1] to near-well[2] in some cases (particularly in results for wellbore pressure). Further improvement can be obtained in more difficult cases through use of the optimization procedure. This suggests that most of the benefit derived from solving the full fine grid problem to compute the coarse grid parameters can be obtained through use of the near-well[2] (with optimization) procedure. This is encouraging, because the near-well[2] calculation is much more computationally efficient than solving the full fine grid model and is practical for use with highly detailed fine grid models.

5.3 Numerical Results for Flow Driven by Horizontal Wells

Detailed flow results are now presented for flow driven by horizontal wells in heterogeneous systems. Single and three phase flow scenarios are considered. In all cases, the fine grid model is a geostatistical realization of prescribed statistics. All geostatistical realizations were generated using GSLIB (Geostatistical Software Library) (Deutsch and Journel, 1998). The flow simulations were performed using a commercial reservoir simulator (Eclipse Reservoir Simulator, GeoQuest, Schlumberger).

Coarse grid models are generated by uniformly coarsening the fine grid permeability field (i.e., coarsening by a fixed factor in each coordinate direction) and computing equivalent grid block permeabilities $\mathbf{k}^*$ for each coarse grid block using the GSLIB algorithms (Deutsch and Journel, 1998). Uniform coarsening is known to be sub-optimal; e.g., Durlofsky et al. (1997) demonstrated significant improvement in coarse scale displacement results when the fine grid is nonuniformly coarsened. This nonuniform coarsening is of particular importance when the flow is strongly impacted by connected regions of high permeability (e.g., layering), as is often the case for displacement processes involving vertical wells in layered systems. For the primary production problems considered below, with flow driven by horizontal wells, reservoir performance is in general less dominated by connected regions of high permeability than in the vertical well case. Therefore, nonuniform coarsening is less essential and a uniformly coarsened grid may prove adequate. Nonetheless, nonuniform coarsening would still be expected to provide improved accuracy in displacement calculations.

For the single phase flow cases discussed below, results are presented in terms of well productivity ($q/\Delta p$) at steady state and flow profiles along the horizontal well (i.e., inflow versus normalized position along the well). In all cases, the fine grid results are compared to the coarse grid results with no near-well upscaling (the standard approach) and to coarse grid results with the near-well upscaling procedure described above. In computing results using the standard approach, $\mathbf{k}^*$ is calculated for each grid block (including well blocks) and then the coarse scale well index is computed using the Peaceman (1983) method as applied to the grid block $\mathbf{k}^*$. All transmissibilities are computed directly from the $\mathbf{k}^*$. In some of the cases discussed below, results are presented using both near-well[1] and near-well[2] upscaling (see the discussion above for de-

scriptions of these terms). Unless otherwise stated, the coarse scale models are generated using the optimization procedure described above. For clearer comparisons between fine and coarse grid results, the fine grid inflow profiles are summed over regions corresponding to the coarse grid blocks.

It is important to note that, in this work, the near-well upscaling method is assessed by comparing coarse scale results to the reference fine grid results. For present purposes, therefore, the fine grid results are considered to be "correct." However, the fine grid model itself may not always provide numerical results that are converged (or nearly so). This might be the case when, for example, shales are represented by a single grid block. In such instances the coarsened model, even if it matches the fine grid result exactly, will still reflect the error inherent in the fine grid solution. This potential source of error can be minimized through the use of higher levels of resolution in the fine grid model.

5.3.1 Single Phase Flow Results. In the first two examples, the permeability fields are log-normally distributed, with the logarithm of permeability specified to be of a prescribed variance (σ^2) and correlation structure. The correlation structure is specified in terms of the dimensionless correlation lengths l_x, l_y and l_z, where each correlation length is nondimensionalized by the system length in the corresponding direction. A single horizontal well of length 2100 ft centered in a formation of physical dimensions 5100 ft $\times$ 5100 ft $\times$ 225 ft is considered. The total production rate is set to 50,000 bbl/d. The top and bottom of the system are maintained at a fixed pressure (the average reservoir pressure is about 3000 psi) and there is no flow through the sides. These boundary conditions are meant to qualitatively represent a reservoir underlain by a large aquifer (and overlain by a large gas cap) that act to approximately maintain pressure above and below the oil region. After a brief transient period, the system achieves a steady state and the wellbore pressure reaches a constant value.

The fine scale model is of dimension (NX $\times$ NY $\times$ NZ) 51 $\times$ 51 $\times$ 45 (a total of 117045 cells) and the coarse grid (coarsened by a factor of 3 in each direction) is of dimension 17 $\times$ 17 $\times$ 15 (4335 cells). We first set $l_x = l_y = 0.25$, $l_z = 0.05$ and σ=1. Inflow profiles for the fine and coarsened models are shown in **Fig. 5-2**. The standard coarse grid model shows considerable deviation from the fine grid results. However, both the near-well[1] and near-well[2] coarse grid re-

sults are in excellent agreement with the fine grid flow profile. Results for normalized well productivity $(q/\Delta p)_n$ (normalized by $(q/\Delta p)$ for the fine grid model), are shown in **Fig. 5-3**. The standard coarse model shows an error of about 13%; the results using near-well[1] (designated NW[1] in the figure) are in error by about 8% while results using near-well[2] (NW[2] in the figure) are in error by only 3%.

The next case considered is for a more highly correlated (in x and y) permeability field; $l_x = l_y = 0.5$, $l_z = 0.05$, with more overall variability, σ=2. This type of permeability field corresponds to an incompletely layered system. The inflow profiles for this case are shown in **Fig. 5-4**. Results using standard coarsening for this more highly heterogeneous case are in considerable error relative to the fine grid results, while those using the near-well upscaling are in very close agreement. The productivity results (**Fig. 5-5**) show that standard coarsening gives an error of about 32%; near-well[2] upscaling reduces this error to about 3%. This example illustrates that, in some cases, near-well upscaling is necessary both to capture the correct inflow profile and to provide the correct wellbore pressure for a prescribed flow rate. For both this and the previous case, the near-well upscaling results with averaging (rather than optimization) are very close (within a few percent) to the results presented here, so the optimization procedure is not essential for these examples.

The results in Figs. 5-2 to 5-5 are typical of many of the other results obtained (but not shown) for single horizontal wells in log-normal permeability fields. Specifically, the standard coarse grid results show considerable errors in the inflow profile, while the results using near-well upscaling (either near-well[1] or near-well[2]) show close agreement between the fine and coarse models. Results for well productivity using near-well[1] upscaling show improvement over the coarse grid results; near-well[2] upscaling results in turn display improvement over the near-well[1] results.

The next examples are more demanding and involve a single horizontal well in sand-shale permeability fields. The reservoir is now of dimensions 10,000 ft $\times$ 5000 ft $\times$ 100 ft and the well (centered in the reservoir) is of length 2000 ft. The permeability descriptions used here are realizations previously generated by Aziz et al. (1999). This field, described in detail by Aziz et al. (1999), represents a fluvial sandstone reservoir with a net to gross ratio of 70%. Sequential indicator simulation was applied to generate the lithofacies model. Shales typically extend over a

range of about 100 ft × 100 ft × 10 ft and are of permeability 1 mD. In the sandstone, porosity and permeability are correlated over O(2000 ft) areally and O(1-10 ft) vertically. Sandstone permeability is centered at about 500 mD. As discussed in the Introduction, Aziz et al. (1999) observed significant inaccuracy in coarse scale models generated from these permeability fields.

The fine scale model is of dimension 100 × 50 × 32 (160,000 cells) and the coarse grid is of dimension 20 × 10 × 12 (2400 cells). The coarse grid is generated from the fine grid via a uniform coarsening (by a factor of five in x, five in y and three in z, with additional layers at the top and bottom of the model to provide pressure support). As in the previous examples, well flow rates are specified and the simulations are run until steady state is achieved. In this case, we compare the optimization procedure with the averaging approach described in section 5.2. In both cases, the near-well[2] region is used in the upscaling procedure.

Production profiles for the four cases are shown in **Fig. 5-6**. The standard coarse grid results are in considerable error relative to the fine grid results. The near-well[2] scale up results, using either averaging or optimization, are in relatively good agreement with the fine grid results, though the agreement here is not of the level achieved in the log-normal permeability cases. Interestingly, the production peak is captured slightly more accurately using averaging than it is using optimization. The normalized well productivity results are shown in **Fig. 5-7**. The standard coarse grid model significantly overpredicts the well productivity; the error in $(q/\Delta p)_n$ is about 85%. Results using either of the near-well upscaling methods are in closer agreement with the fine grid model. The near-well[2] with optimization results (NW(o) in the figure) are, in this case, more accurate than the near-well[2] with averaging results (NW(a) in the figure). Specifically, the error in $(q/\Delta p)_n$ is reduced from 32% (with averaging) to 18% (with optimization).

Results using another sand/shale realization of the same statistics are shown in **Figs. 5-8** and **5-9**. These results display the same trends as observed in Figs. 5-6 and 5-7. In this case, however, the productivity computed from the standard coarse model is in error by over 100%. The near-well[2] with averaging upscaled model reduces this error to 9.4%; the near-well[2] with optimization upscaling further reduces the error to only 2.5%. The simulation results using the sand/shale realizations demonstrate the significant gains in accuracy that can be obtained through

use of near-well upscaling and the additional advantage that can be derived by using the parameter optimization approach.

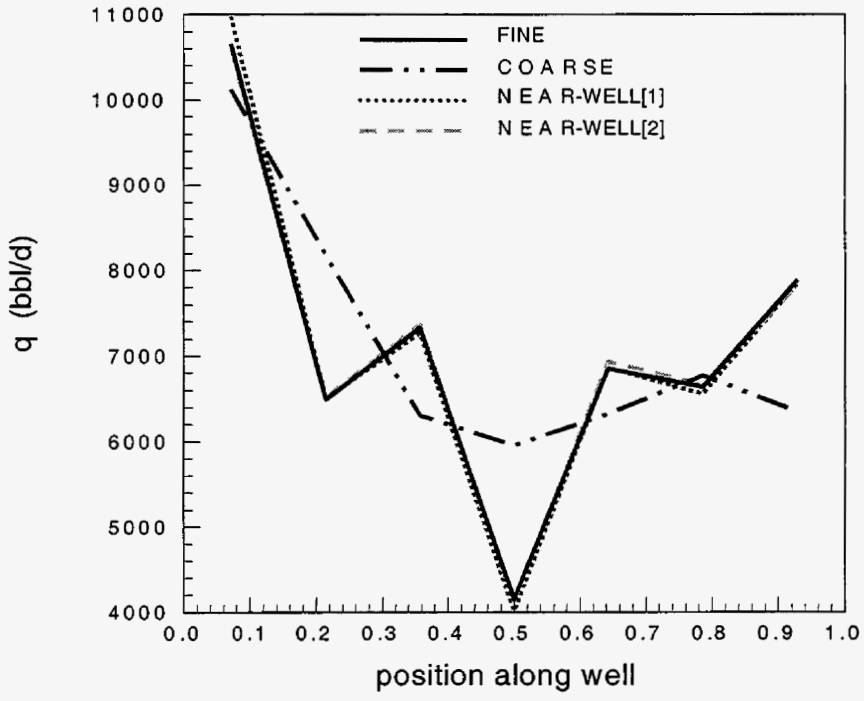

Fig. 5-2: Inflow profiles along the well for $l_x = l_y = 0.25$, $l_z = 0.05$, $\sigma = 1$.

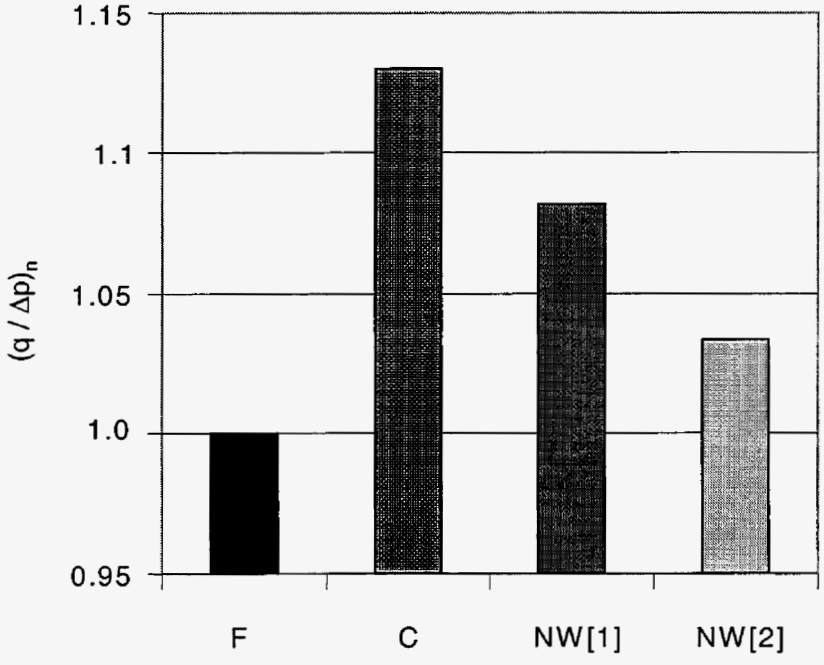

Fig. 5-3: Normalized well productivity for $l_x = l_y = 0.25$, $l_z = 0.05$, $\sigma = 1$.

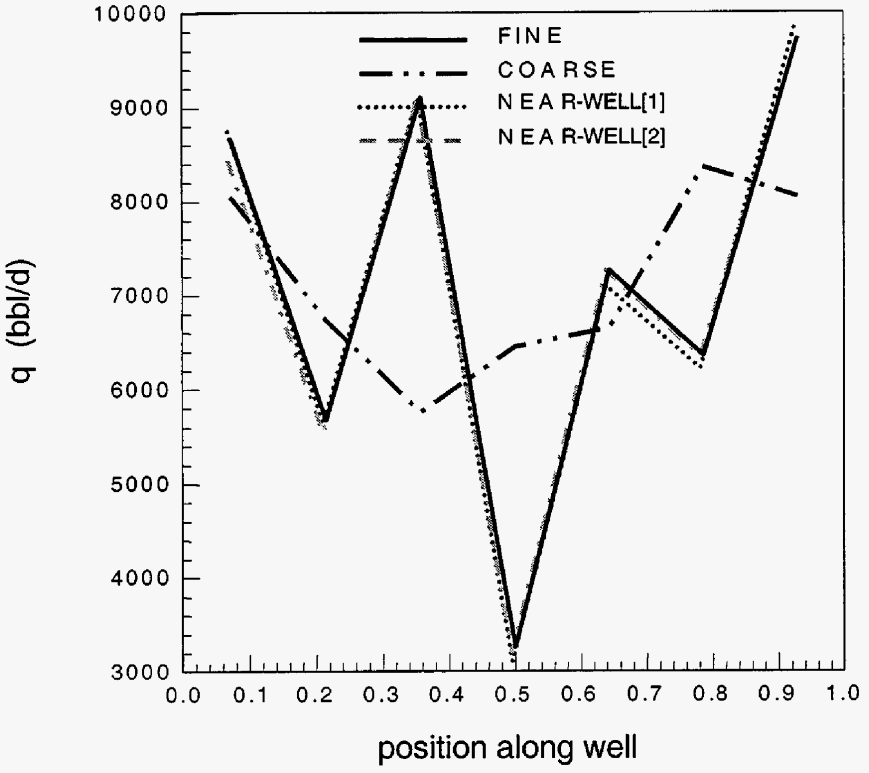

Fig. 5.4: Inflow profiles along the well for $l_x = l_y = 0.5$, $l_z = 0.05$, $\sigma = 2$.

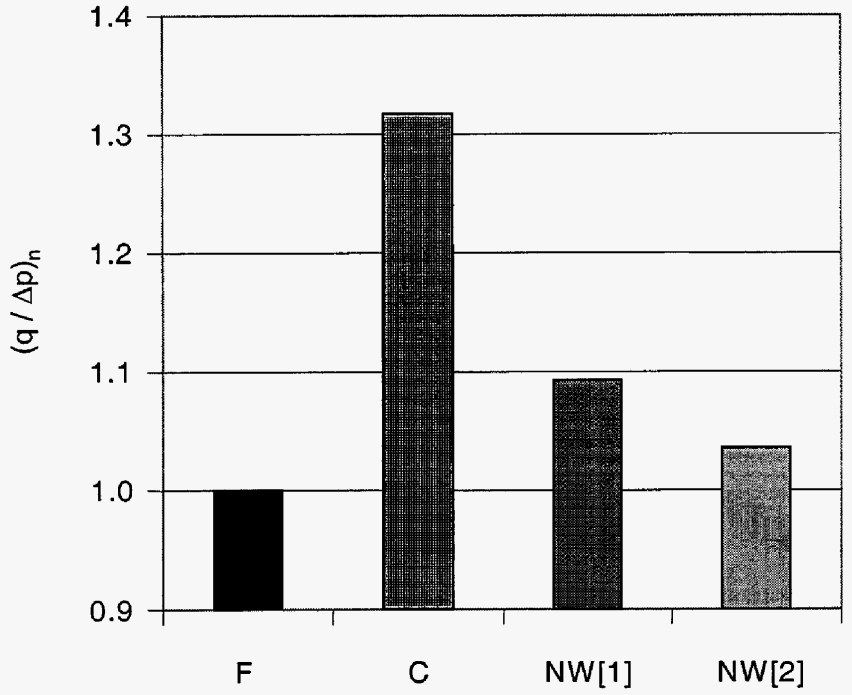

Fig. 5-5: Normalized well productivity for $l_x = l_y = 0.5$, $l_z = 0.05$, $\sigma = 2$.

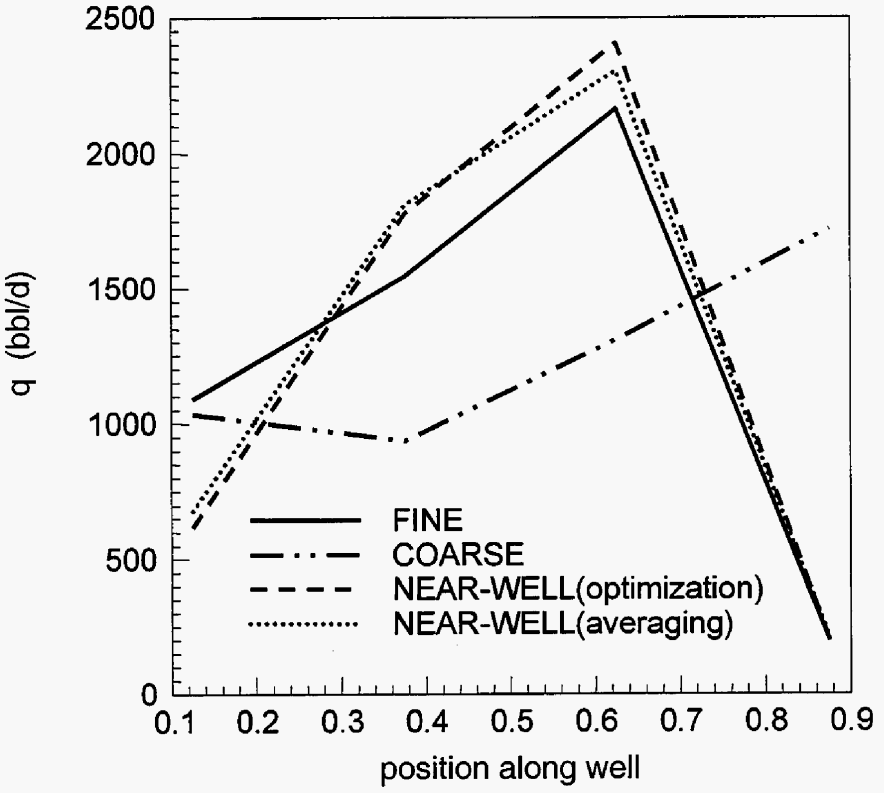

Fig. 5-6: Inflow profiles along the well for sand/shale system.

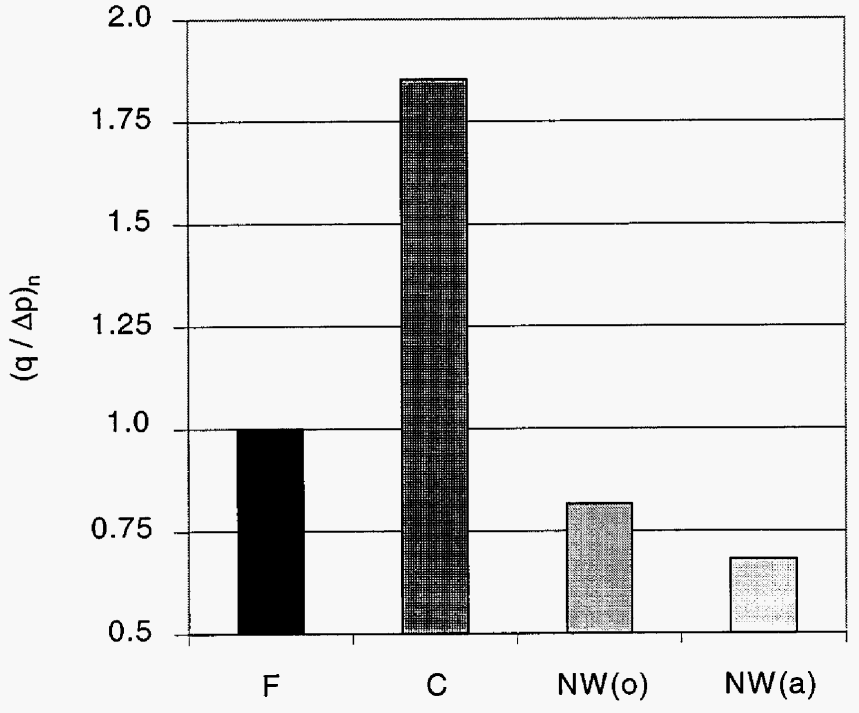

Fig. 5-7: Normalized well productivity for sand/shale system.

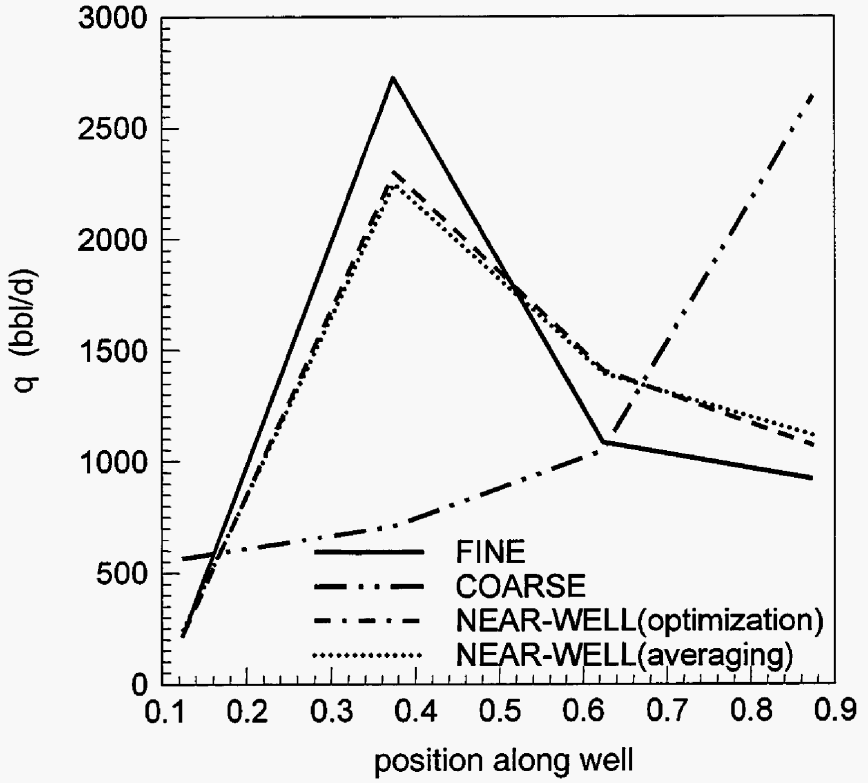

Fig. 5-8: Inflow profiles along the well for a second realization of the sand/shale system.

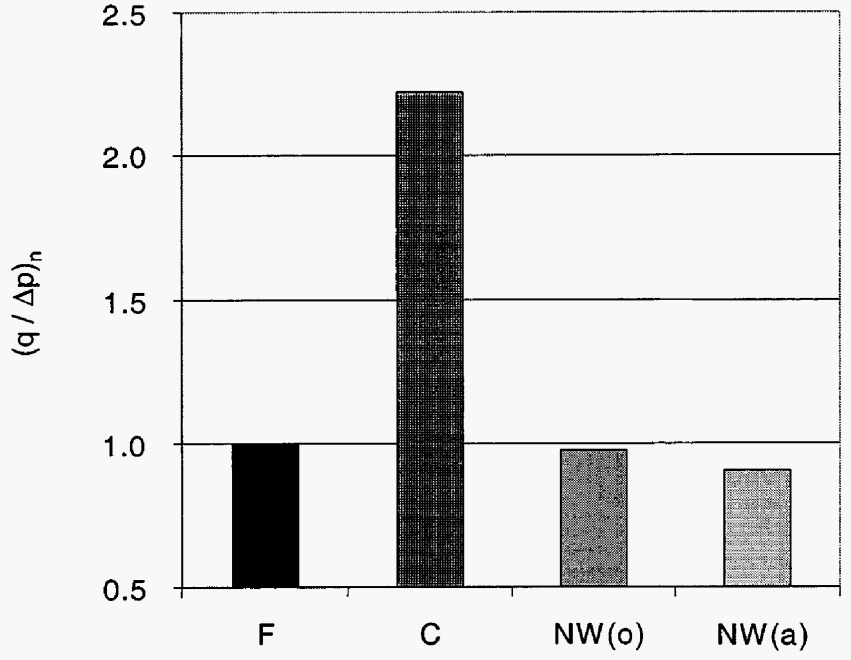

Fig. 5-9: Normalized well productivity for a second realization of the sand/shale system.

5.3.2 Three Phase Flow Results. The final case involves a single horizontal well in the oil zone of a sand/shale reservoir containing a large aquifer and a large gas cap. This case was previously considered by Aziz et al. (1999), who showed that standard upscaling techniques could lead to significant error in simulation predictions. The reservoir description here is the same as that in the sand/shale case considered above (Figs. 5-6 and 5-7).

The well is prescribed to produce at 5000 bbl/d, with a minimum bottom hole pressure constraint of 1500 psi. The reservoir boundaries are all specified to be no-flow (refer to Aziz et al. (1999) for a more detailed description of the reservoir and fluid properties). The fine scale model is of dimension $100 \times 50 \times 32$ (160,000 cells) and the coarse grid is of dimension $25 \times 25 \times 12$ (7500 cells). The coarse grid is generated from the fine grid via a uniform coarsening (by a factor of four in x, two in y and three in z, with an additional layer in both the aquifer and the gas cap).

Simulation results for oil production rate and wellbore pressure, for the fine model, standard coarse model, and coarse model with near-well[2] upscaling (with optimization), are shown in **Figs. 5-10** and **5-11**. The well in the fine grid simulation model reaches the minimum bottom hole pressure constraint relatively early in the run (after about one year) and the well produces at this pressure for the remainder of the simulation. Production clearly declines once the well reaches the minimum bottom hole pressure. The standard coarse model is in considerable error, continuing to produce at the initial rate for about 3000 days (a factor of nearly ten too long). The coarse model with near-well upscaling, by contrast, is in reasonably close agreement with the fine scale result, though the differences are clearly greater than in the single phase flow examples presented above. Nonetheless, the coarse model with near-well upscaling provides results that are substantially better than those obtained using the standard coarse grid model.

The next results, shown in **Fig. 5-12**, are for water cut (fraction of water in the produced fluid) for the three models. Again the results with near-well upscaling track the fine grid results much closer than the standard coarse grid results, which show delayed water breakthrough (relative to the fine grid model) and an inaccurate post-breakthrough trend. Results for gas-oil ratio (GOR) are shown in **Fig. 5-13**. Here, though the results with near-well upscaling are much closer to the fine grid results than the standard coarse grid results, they do overpredict GOR significantly. It is possible that the high gas production in the coarse model with near-well upscaling

is due to other aspects of the upscaled model, not related to the near-well treatment. It is therefore quite possible that this result could be improved through application of a nonuniform coarsening procedure in conjunction with near-well upscaling.

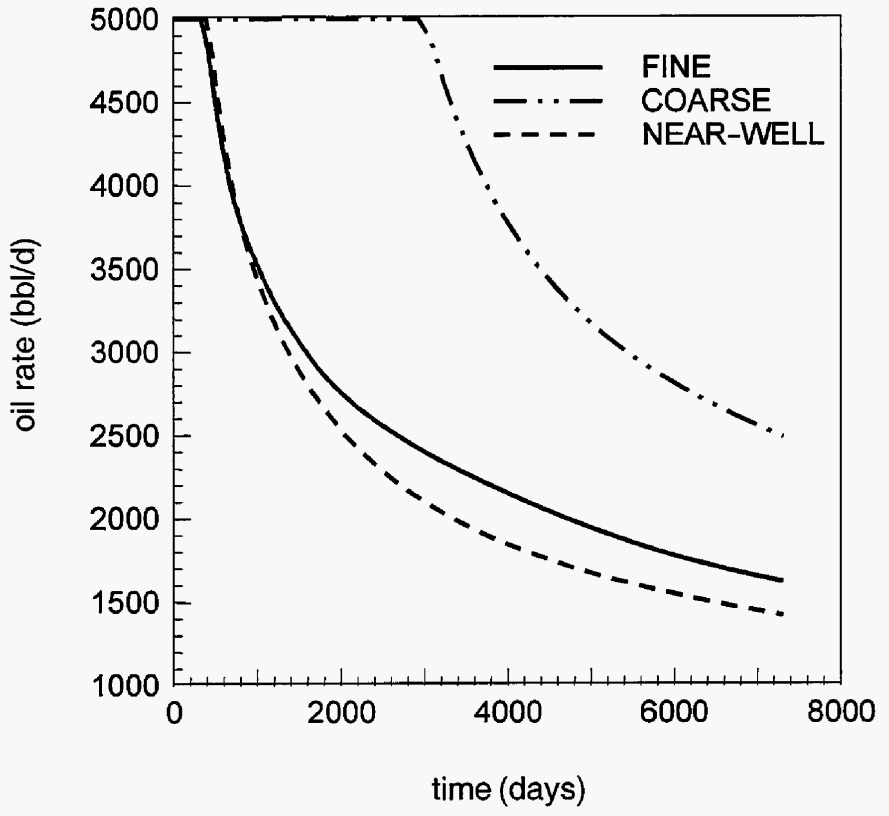

Fig. 5-10: Oil production rate (three phase flow) for sand/shale system.

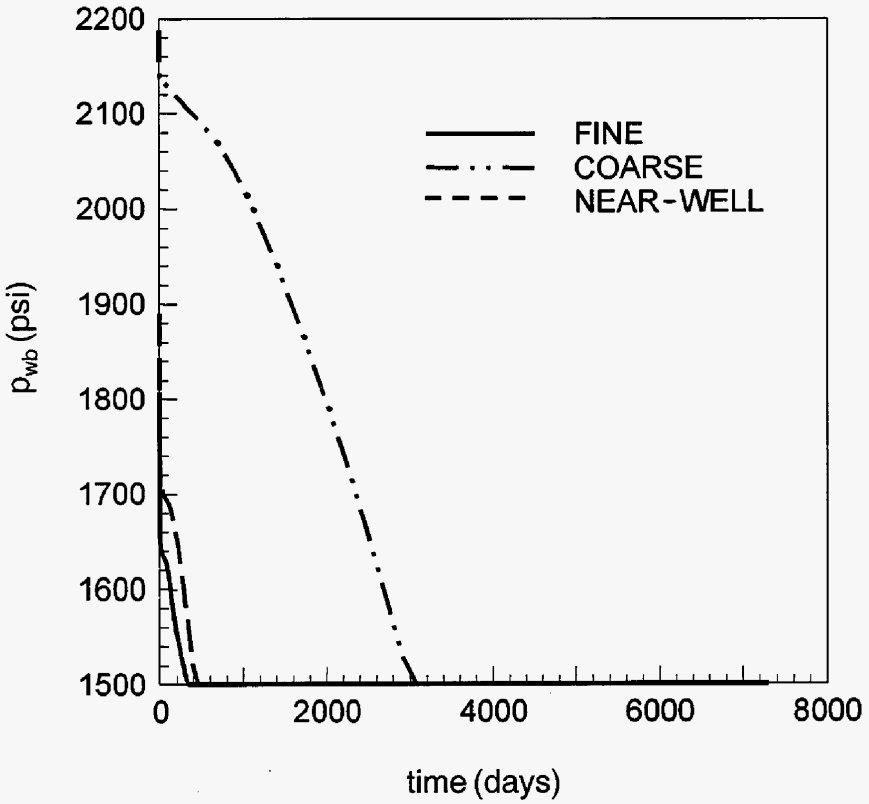

Fig. 5-11: Wellbore pressure for sand/shale system.

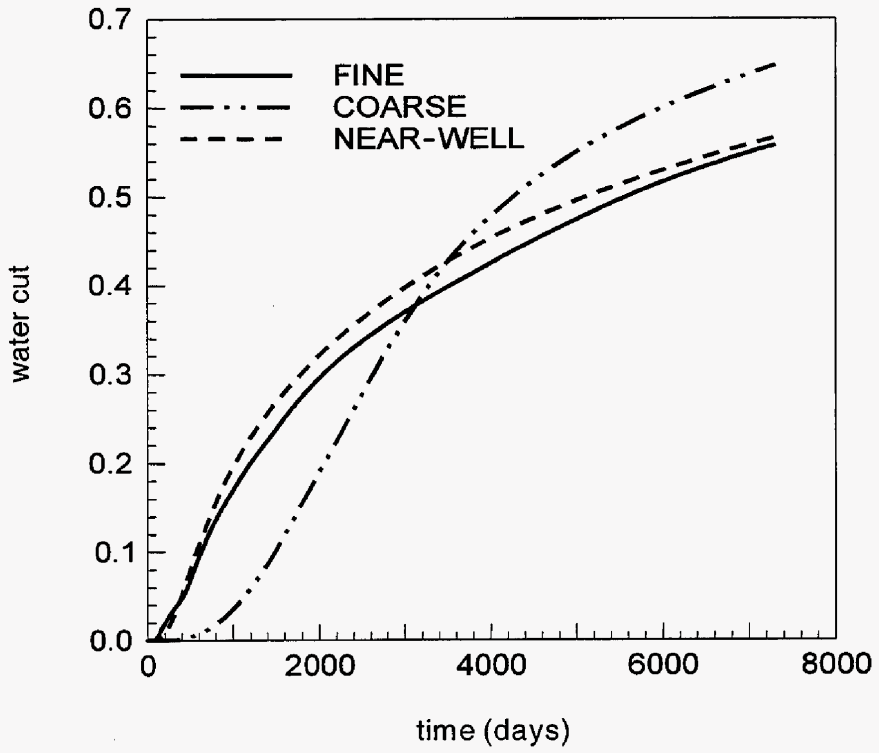

Fig. 5-12: Water cut for sand/shale system.

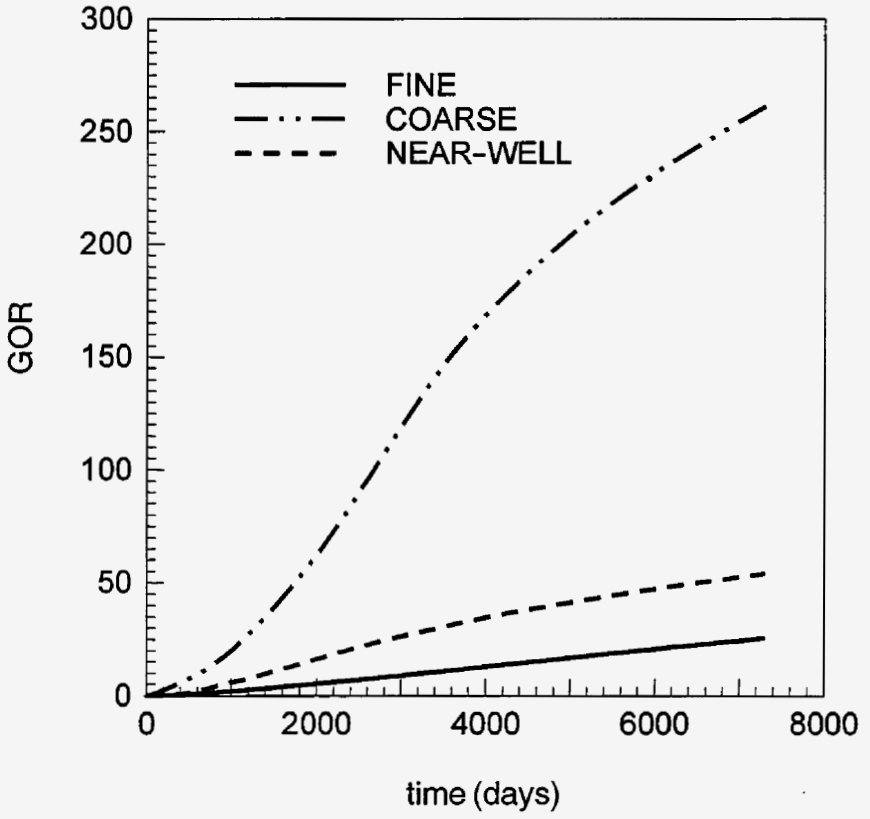

Fig. 5-13: Gas-oil ratio for sand/shale system.

5.4 Conclusions and Future Directions

In this chapter, a method was presented for upscaling in the region near flowing horizontal wells. The method represents a generalization of previous techniques applicable for vertical wells. The approach entails the solution of a local well-driven flow problem and the subsequent calculation of coarse grid parameters (transmissibilities and well indexes). Higher levels of accuracy in the coarse scale model are obtained through an optimization of the near-well parameters. The local fine scale problems that were solved to compute the coarse grid parameters include the fine scale description of the formation over a region corresponding to one or two 'rings' of coarse scale grid blocks around the well blocks. Although this region itself may contain several thousand grid blocks, it is still much smaller than the full global domain (which may contain $O(10^7)$ cells). This renders the method more computationally efficient than other methods that require the solution of global flow problems to determine the coarse scale description in the near-well region.

Results using the new method were shown to agree much more closely with the reference fine grid solutions than results using standard coarse scale models with no near-well upscaling. In some cases (e.g., sand/shale systems), the parameter optimization was shown to provide improved coarse scale descriptions compared to those obtained using the near-well averaging procedure. The overall near-well upscaling approach should generalize to other, more complicated well configurations (e.g., deviated or multilateral), though issues of the size of the local flow problem and the appropriate boundary conditions to be imposed must be addressed. The method could also be applied to vertical wells and might provide more accurate coarse grid results than previous near-well upscaling methods. Finally, the full linkage of this approach to the overall nonuniform coarsening methodology can be expected to provide even better accuracy in coarse scale simulations of horizontal wells.

In future work, we plan to extend the approach presented here to handle more complex non-conventional wells (e.g., multilaterals). This will entail the use of more complicated gridding and discretization approaches (along the lines of those described in Chapter 2) for the solution of the local fine scale problem. The coarse models in this case might be either Cartesian (as in the approach presented in this chapter) or modular (as in the examples in Chapter 2). Successful developments in these directions will provide a very general capability for the accurate coarse scale modeling of non-conventional wells in general reservoir simulators.

5.5 References

Aziz, K., Arbabi, S. and Deutsch, C.V.: "Why is it so Difficult to Predict the Performance of Horizontal Wells?" *JCPT*, 37-45, Oct. 1999.

Bard, Y.: *Nonlinear Parameter Estimation*, Academic Press, New York, 341 p, 1974.

Deutsch, C. and Journel, A.G.: *GSLIB: Geostatistical Software Library and User's Guide*, 2nd edition, Oxford University Press, 368 p, 1998.

Ding, Y.: "Scaling-up in the Vicinity of Wells in Heterogeneous Field," paper SPE 29137 presented at the 1995 SPE Symposium on Reservoir Simulation, San Antonio, Texas, Feb. 12-15.

Ding, Y. and Urgelli, D.: "Upscaling of Transmissibility for Field Scale Flow Simulation in Heterogeneous Media," paper SPE 38016 presented at the 1997 SPE Symposium on Reservoir Simulation, Dallas, Texas, June 8-11.

Durlofsky, L.J.: "Numerical Calculation of Equivalent Grid Block Permeability Tensors for Heterogeneous Porous Media," *Water Resour. Res.*, **27**, 699-708, 1991.

Durlofsky, L.J., Jones, R.C. and Milliken, W.J.: "A Nonuniform Coarsening Approach for the Scale Up of Displacement Processes in Heterogeneous Porous Media," *Adv. Water Resour.*, **20**, 335-347, 1997.

Durlofsky, L.J., Milliken, W.J. and Bernath, A.: "Scaleup in the Near-Well Region," *SPEJ*, 110-117, March 2000.

Gill, P.E., Murray, W. and Wright, M.H.: *Practical Optimization*, Academic Press, New York, 401 p, 1981.

Lemouzy, P.: "Quick evaluation of multiple geostatistical models using upscaling with coarse grids: A practical study," presented at the Fourth International Reservoir Characterization Technical Conference, Houston, Texas, March 2-4, 1997.

Mascarenhas, O., 1999. Accurate Coarse Scale Simulation of Horizontal Wells. Master's report, Stanford University.

Mascarenhas, O. and Durlofsky, L.J.: "Coarse Scale Simulation of Horizontal Wells in Heterogeneous Reservoirs," *J. Pet. Sci. and Eng.*, **25**, 135-147, 2000.

Muggeridge, A.H., Cuypers, M., Bacquet, C. and Barker, J.W.: "Scale-up of Well Performance for Reservoir Flow Simulation," presented at the 1999 European Symposium on Improved Oil Recovery, Brighton, UK, Aug. 18-20.

Peaceman, D.W.: "Interpretation of Well-Block Pressures in Numerical Reservoir Simulation with Nonsquare Grid Blocks and Anisotropic Permeability," *SPEJ*, 531-543, June 1983.

Pickup, G.E., Ringrose, P.S., Jensen, J.L. and Sorbie, K.S.: "Permeability Tensors for Sedimentary Structures," *Math. Geol.*, **26**, 227-250, 1994.

Renard, Ph. and de Marsily, G.: "Calculating Equivalent Permeability: A Review. *Adv. Water Resour.*, **20**, 253-278, 1997.

Soeriawinata, T., Kasap, E. and Kelkar, M.: "Permeability Upscaling for Near-Wellbore Heterogeneities," *SPEFE*, 255-262, Dec. 1997.

Wen, X.-H. and Gomez-Hernandez, J.J.: "Upscaling Hydraulic Conductivities in Heterogeneous Media: An Overview," *J. Hydrol.*, **183**, ix-xxxii, 1996.

6 Approximate Finite Difference Modeling of the Performance of Horizontal Wells in Heterogeneous Reservoirs

by Burak Yeten, Christian Wolfsteiner, Louis J. Durlofsky and Khalid Aziz

6.1 Introduction

The detailed scale up of fine grid heterogeneity fields can be accomplished using the approach described in Chapter 5. This approach provides accurate coarse scale descriptions of heterogeneity in the near-well region and is best suited for cases in which detailed reservoir flow predictions are required. In cases when many geostatistical realizations and well placement scenarios are to be investigated, however, the detailed models generated using the methodology described in Chapter 5 may be overly time consuming to generate and run. In such cases, a more efficient and more approximate approach may be appropriate. The method described in this chapter falls into this category.

In Chapter 3, we described a semi-analytical technique for modeling non-conventional well performance (this work is also described in Ouyang and Aziz, 1998 and Wolfsteiner et al., 2000a, 2000b). The approach is based on Green's functions and requires that only the well, rather than the reservoir, be discretized. The method accounts approximately for the effects of reservoir heterogeneity and wellbore hydraulics. Like other semi-analytical techniques, this method is applicable for a limited set of problems; e.g., for single phase flow in slightly compressible systems.

A novel aspect of this semi-analytical approach is the way in which reservoir heterogeneity is represented. Specifically, we model highly variable permeability fields in terms of an effective near-well skin s and a constant background permeability $\mathbf{k}^*$. The near-well skin varies as a function of position along the well and is computed from the permeability field in the vicinity of each well segment. The background permeability represents an effective, large scale, linear flow effective permeability. We refer to the overall semi-analytical approach as the s-$\mathbf{k}^*$ method because of the way heterogeneity is modeled. The accuracy of this approach was established through extensive comparisons with detailed single phase finite difference calculations, as presented in Chapter 3.

In many cases, two phase flow effects can significantly impact the performance of non-conventional wells (e.g., aquifer coning). Because these effects are not included in existing semi-analytical approaches, some type of finite difference modeling is generally required for problems of this type. The approach described in Chapter 5 represents a highly accurate approach for this problem. In this chapter, we explore an alternate, simpler and more computationally efficient method. We represent reservoir heterogeneity in the finite difference models in terms of s and $\mathbf{k}^*$, just as in our semi-analytical model of single phase flow. The finite difference model then contains a homogeneous (but anisotropic) permeability field and a skin specified in each of the well blocks. This permeability representation is much simpler and can be simulated on a coarser grid than the generally heterogeneous representation. We show that this approach is efficient and reasonably accurate relative to the reference (heterogeneous) fine grid solution for many (but not all) flow quantities of interest.

Our goal in this work is to incorporate approximately the effects of reservoir heterogeneity into simplified finite difference simulation models of non-conventional wells. Our specific interest is in capturing two phase flow effects. We are not aware of any previous studies directly along these lines. However, as described in Chapter 3, previous studies have been directed at the development of approximate methods for modeling the effects of heterogeneity on vertical (Durlofsky, 2000) and horizontal (Brekke and Thompson, 1996) wells operating under single phase flow. Other work targeted the modeling of horizontal or deviated wells in layered formations (Lee and Milliken, 1993; Basquet et al., 1998). These studies all applied approximate or semi-analytical (based on Green's functions) solution techniques. Previous work geared toward assessing the effects of heterogeneity on horizontal well performance (for one, two and three phase flow) has also been performed within a general finite difference context (Yamada and Hewett, 1995; Gharbi et al., 1997; Aziz et al., 1999; also see the references in Chapter 5). These studies, as well as the results of Chapter 5, highlighted the important effects of reservoir heterogeneity and demonstrated the difficulty of capturing these effects in standard coarse finite difference models.

This chapter proceeds as follows. We first briefly review our simplified representation of heterogeneity in terms of s and $\mathbf{k}^*$. We then describe our approach for simplified finite difference modeling. Next, we present extensive simulation results using this approach and compare these

results to those obtained from the full heterogeneous permeability field. We demonstrate that certain quantities, such as well productivity and the expected water breakthrough time, are well approximated by our proposed methodology. Other quantities, such as water cut at late time, are less accurately represented. We conclude with a discussion of other possible applications for our simplified representation of reservoir heterogeneity.

6.2 Permeability Representation with s and $\mathbf{k}^*$

Our representation of permeability in terms of a near-well effective skin s and a background effective permeability $\mathbf{k}^*$ was described in detail in Chapter 3 and in previous papers (Durlofsky, 2000; Wolfsteiner et al., 2000a, 2000b) so our description here will be brief and will be with reference to a finite difference simulator. We assume that detailed, heterogeneous permeability realizations, generated geostatistically, are available. For each particular realization, we compute s and $\mathbf{k}^*$ for use in the finite difference simulator as follows.

The skin s accounts for near-well heterogeneity and varies with position along the well. We designate the skin for the portion of a well in grid block i as s_i. This skin is a function of the local near-well permeability, designated $k_{a,i}$, the background permeability $\mathbf{k}^*$ and the effective radius of the region over which the near-well permeability is computed, r_a. The skin for each well segment is then computed as:

$$s_i = \left(\frac{k_s^*}{k_{a,i}} - 1 \right) \ln \frac{r_a}{r_w} \quad , \tag{6-1}$$

where r_w is the wellbore radius and k_s^* is the geometric average of the diagonal components of $\mathbf{k}^*$. This representation derives from the standard definition of skin (Hawkins, 1956), with appropriate modification to account for the heterogeneous permeability field.

The effective permeability $\mathbf{k}^*$ can be computed either numerically via steady state single phase flow calculations over the entire domain or through the use of approximate analytical expressions (Ababou, 1990). In either case this computation represents a minor overhead relative to solving the full two phase fine grid problem. The local near-well permeability is a weighted aver-

age of $\mathbf{k}$ in the near-well region a. It is computed by integrating over the region a, an elliptic cylinder of size and shape as determined from the correlation structure of the permeability field:

$$k_{a,i}^{\omega} = \frac{1}{\Gamma_a} \int_a \frac{k^{\omega}(\mathbf{x})}{r^n} d\mathbf{x} \ , \tag{6-2}$$

where Γ_a is a normalizing factor as defined in Chapter 3. The quantity ω is the permeability weighting exponent. Values of ω = -1, 0, 1 correspond to a harmonic, geometric (i.e., logarithmic) and arithmetic average respectively and n is a spatial weighting parameter. In this work we take ω =0 and n=2, which corresponds to a generalized geometric weighting.

The skin for well segment i as computed from Eqs. 6-1 and 6-2 is then input directly into the finite difference simulator. All grid block permeabilities are specified to be $\mathbf{k}^*$, which is in general anisotropic. The usual two phase flow quantities (e.g., relative permeabilities) and other parameters must also be input into the simulator.

Before presenting two phase flow results using this approach, we note that the general level of accuracy of the s-$\mathbf{k}^*$ permeability representation for single phase flow problems was demonstrated in Chapter 3. These results demonstrate the strong effect of near-well heterogeneity and the ability of the s-$\mathbf{k}^*$ approach to adequately capture it.

6.3 Simplified Finite Difference Modeling of Horizontal Wells in Heterogeneous Reservoirs

We now demonstrate the accuracy and limitations of the s-$\mathbf{k}^*$ representation of heterogeneity for two phase flow problems with horizontal wells. The detailed permeability descriptions (denoted as "detailed $\mathbf{k}$" or "d$\mathbf{k}$" in the following) were generated using GSLIB (Deutsch and Journel, 1998). The effective permeability and skin in each well block were computed as described above. In all cases, the simplified finite difference results (using the s-$\mathbf{k}^*$ permeability representation) are compared to finite difference results using the detailed heterogeneous permeability fields. We also present results using homogeneous models; i.e., using only the effective permeability $\mathbf{k}^*$ with no skin.

The permeability fields and reservoir and production parameters considered are described in **Table 6-1**. In all cases we model a single, fully penetrating horizontal well in the middle of the oil zone. The compressibility of the system is dominated by the rock compressibility, c. We consider three different statistical permeability descriptions, as indicated in the table. These fields differ in terms of their correlation lengths l_x, l_y and l_z. The permeability for all three fields is log-normally distributed, with a mean of 100 md and a coefficient of variation (σ_k/m) of about 1. In the results presented below, we simulated 15 realizations of each permeability description. Though more realizations would generally be required to obtain converged ensemble statistics, this number of realizations is sufficient to illustrate the capabilities and limitations of the s-$\mathbf{k}^*$ heterogeneity representation. Most of the detailed results presented below are for permeability field permB. Results for the other permeability fields are summarized in tables.

Table 6-1: Reservoir, Fluid and Well Properties

drainage area		4500 x 4500 ft^2
thickness		175 ft
porosity ϕ		0.25
correlation	permA	$l_x=l_y=0.3$, $l_z=0.3$
structure	permB	$l_x=l_y=0.3$, $l_z=0.1$
	permC	$l_x=l_y=0.5$, $l_z=0.05$
rock compressibility c		3.0×10^{-5} psi^{-1}
densities $\rho_o=\rho_w$		63 lb_m/ft^3 at 14.7 psi
viscosity μ_o		1.00 cp
rel. perm k_{ro}		1.0 at $S_{wc}=0.25$
viscosity μ_w		0.38 cp
rel. perm k_{rw}		0.13 at $S_{or}=0.25$
well radius r_w		0.2 ft

In all cases the detailed permeability fields were simulated on a grid of 45×45×35. In the first sets of results below, the s-$\mathbf{k}^*$ and homogeneous ($\mathbf{k}^*$ only) permeability descriptions were also simulated on a grid of the same size. Following these demonstrations of the general capabilities of the s-$\mathbf{k}^*$ permeability representation, we present results using s-$\mathbf{k}^*$ for simulations on coarser grids.

6.3.1 Fixed total liquid rate cases. We first consider a well specified to produce at a fixed total liquid flow rate Q_l of 20,000 STB/d. The reservoir is underlain by a strong aquifer, with a pore

volume of about 5000 times the reservoir pore volume and a total compressibility of 3×10^{-5} psi^{-1}, which maintains a high degree of pressure support. For this case, we define the productivity index P_l (based on the total liquid flow rate) as the ratio of Q_l to the difference in pressure between the reservoir and the wellbore; i.e.,

$$P_l = \frac{Q_l}{< p > - p_w} \quad , \tag{6-3}$$

where $<p>$ is the average reservoir pressure and p_w is the wellbore pressure. The productivity index changes with time as the reservoir and wellbore pressures change.

In **Fig. 6-1** we plot P_l versus time for the 15 realizations of permeability field permB. There is a fair degree of variation between the realizations, though some consistent trends are apparent. The relatively rapid decline at approximately 100 days corresponds to water breakthrough; from this time on, the productivity index declines more slowly as water from the aquifer fills the reservoir. We plot productivity index profiles for the same 15 realizations using the s-$\mathbf{k}^*$ permeability representation in **Fig. 6-2**. The results for each realization are plotted using the same line styles in both figures, so a direct comparison for a given realization is possible. From the figures, it is apparent that the results using the s-$\mathbf{k}^*$ representation are in relatively close agreement with the results using the detailed permeability field. This is true both in terms of ensemble average results (i.e., results averaged over all of the realizations) and variation around this average. This is quite encouraging and demonstrates the accuracy of the s-$\mathbf{k}^*$ permeability representation for the calculation of productivity index. We will further quantify the level of agreement between the detailed permeability results and the s-$\mathbf{k}^*$ results below.

Results using a homogeneous permeability description ($\mathbf{k}^*$ only, s=0) are shown in **Fig. 6-3**. Because $\mathbf{k}^*$ varies only slightly from realization to realization, there is very little variation between the 15 curves. These results are clearly inferior to the results using the s-$\mathbf{k}^*$ permeability representation, both in terms of "average" results and variation around the average. This demonstrates the importance of capturing not only the global, overall permeability $\mathbf{k}^*$ but also the variation of permeability in the near-well region.

In **Table 6-2** we present results for the ensemble average productivity index $\overline{P_l}$ and the variation around this average σ_P for the three modeling approaches: detailed $\mathbf{k}$, s-$\mathbf{k}^*$, and $\mathbf{k}^*$ only representation. These results were computed at a time of 610 days (this time is well after water breakthrough). Results are shown for all three permeability descriptions (permA, permB and permC). It is evident from these results that both the average and the variation in the detailed results are captured with reasonable accuracy by the s-$\mathbf{k}^*$ method. The use of $\mathbf{k}^*$ only, by contrast, shows more error for $\overline{P_l}$ and is unable to capture the variation between the realizations. These observations are consistent for all three sets of permeability statistics. Qualitatively similar results are also obtained at early time (10 days).

Fig. 6-4 displays a scatter plot of P_l estimated using the s-$\mathbf{k}^*$ approach (designated $P_l^{s\text{-}\mathbf{k}^*}$) plotted against P_l computed from the detailed $\mathbf{k}$ field (designated $P_l^{d\mathbf{k}}$). Each point represents the productivity index for a particular realization evaluated at a time of 10 days (this time is significantly before water breakthrough). Data from all three permeability descriptions are presented; the circles correspond to permeability field permA, the asterisks to permB and the triangles to permC. The clear grouping of the points around the line of unit slope indicates that there is a close correspondence between the productivity index estimate using the s-$\mathbf{k}^*$ approach and the detailed finite difference result for any given realization. Taken in total, the results in Figs. 6-1 to 6-4 and Table 6-2 demonstrate that the s-$\mathbf{k}^*$ permeability representation is able to accurately model the productivity index of a horizontal well, at least for the systems considered.

The accuracy of the s-$\mathbf{k}^*$ permeability representation degrades somewhat if we consider a more local quantity such as water cut or water breakthrough time. This is illustrated in **Figs. 6-5** to **6-7**, where we plot water cut versus time for the detailed $\mathbf{k}$, s-$\mathbf{k}^*$, and $\mathbf{k}^*$ only simulations. These results are for the same 15 realizations of permeability field permB as presented above. These plots show that, although the variation in breakthrough time t_b is captured to some extent by the s-$\mathbf{k}^*$ representation, at later time the variation is significantly underestimated. The homogeneous permeability representation captures even less of the variation between realizations, as would be expected.

These observations are quantified in **Table 6-3**, where we present the average $\overline{t_b}$ and standard deviation σ_t of breakthrough time for the three types of models. Results for all three sets of permeability statistics are displayed. In these results, breakthrough time is defined as the time at which the water cut is 5%. It is clear from the table that the s-$\mathbf{k}^*$ calculations accurately capture the ensemble average breakthrough time. In addition, σ_t is captured with reasonable accuracy (particularly for permeability descriptions permB and permC), though not as accurately as $\overline{t_b}$. The homogeneous representation, by contrast, significantly overestimates (by 40% in the case of permA) and significantly underestimates σ_t.

Fig. 6-8 displays a scatter plot of the breakthrough times estimated using s-$\mathbf{k}^*$ ($t^{s\text{-}\mathbf{k}^*}$) against breakthrough times computed using the detailed permeability descriptions. Though some degree of correlation is evident, there is significantly more scatter in this plot than in the analogous plot for productivity index (Fig. 6-4). This illustrates that, although the average and variation in t_b are captured with reasonable accuracy by the s-$\mathbf{k}^*$ model, there is less of a one to one correspondence between results for a particular realization than was observed for P_l.

Table 6-4 presents statistics for water cut F_w at late time (610 days) for all of the cases. As is evident from Figs. 6-5 to 6-7, the variation in this quantity is significantly underestimated by the s-$\mathbf{k}^*$ method. However, average behavior is predicted very well by both the s-$\mathbf{k}^*$ method and by the homogeneous model. These results indicate some of the potential limitations of the s-$\mathbf{k}^*$ permeability representation; namely the tendency to underestimate variability in water cut at late times.

Table 6-2: Productivity Index Summary Statistics (610 Days)

	permA		permB		permC	
	P_l	σ_p	P_l	σ_p	P_l	σ_p
dk	91.8	37.2	86.6	22.7	92.7	35.6
s-$\mathbf{k}^*$	89.6	32.5	90.7	29.6	98.4	46.0
$\mathbf{k}^*$	82.2	2.9	82.5	0.7	84.2	0.4

Table 6-3: Breakthrough Time Summary Statistics

	permA		permB		permC	
	t_b	σ_t	t_b	σ_t	t_b	σ_t
dk	104.6	21.3	127.6	14.7	145.5	17.0
s-**k***	110.5	10.4	129.5	14.6	143.2	11.4
k*	146.2	4.6	160.0	1.6	165.2	1.1

Table 6-4: Water Cut Summary Statistics (610 Days)

	permA		permB		permC	
	F_w	σ_F	F_w	σ_F	F_w	σ_F
dk	0.625	0.048	0.609	0.037	0.573	0.034
s-**k***	0.623	0.012	0.592	0.013	0.576	0.010
k*	0.596	0.008	0.571	0.003	0.561	0.003

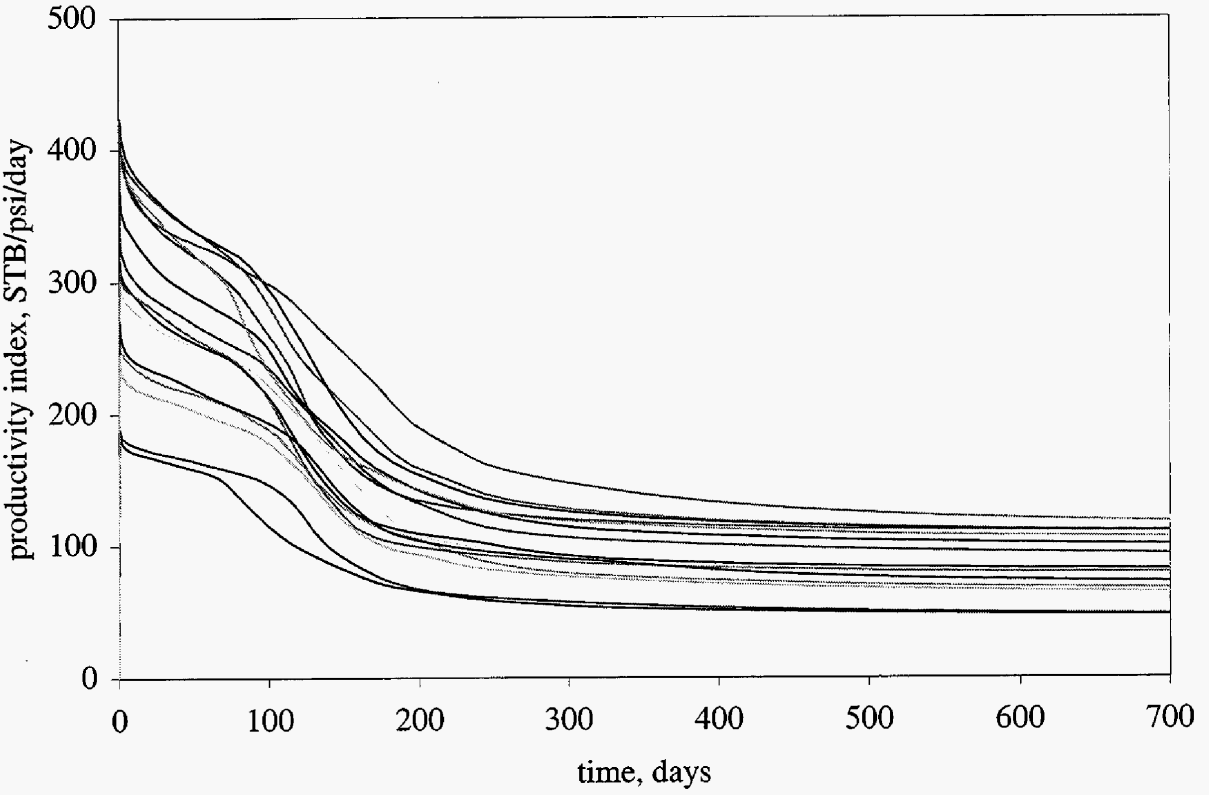

Fig. 6-1: Productivity index profiles (detailed **k**, permB)

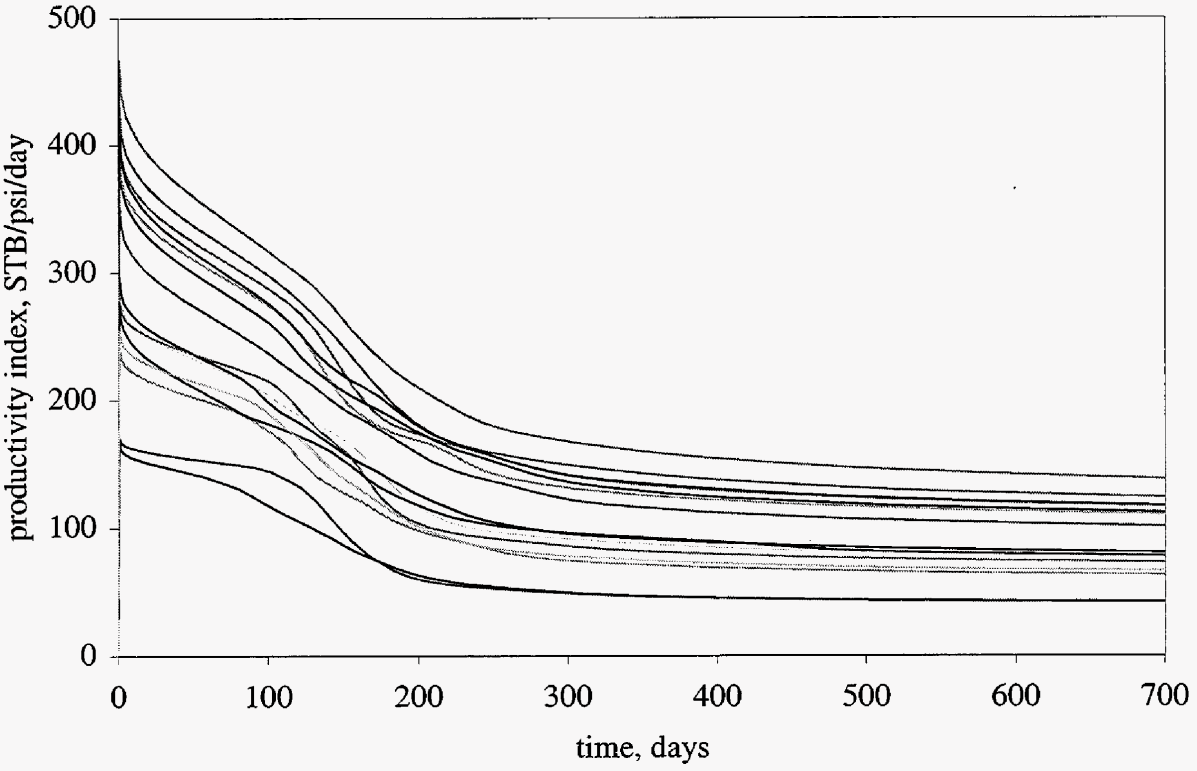

Fig. 6-2: Productivity index profiles (s-$\mathbf{k}^*$, permB)

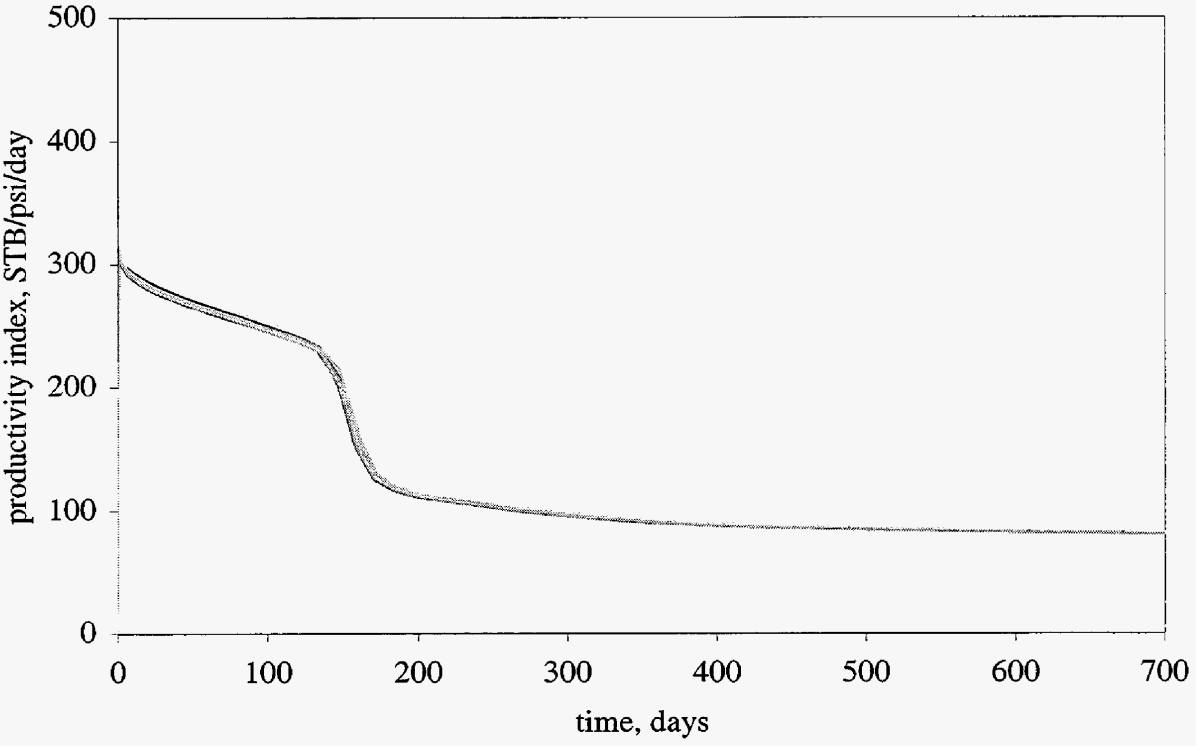

Fig. 6-3: Productivity index profiles ($\mathbf{k}^*$, permB)

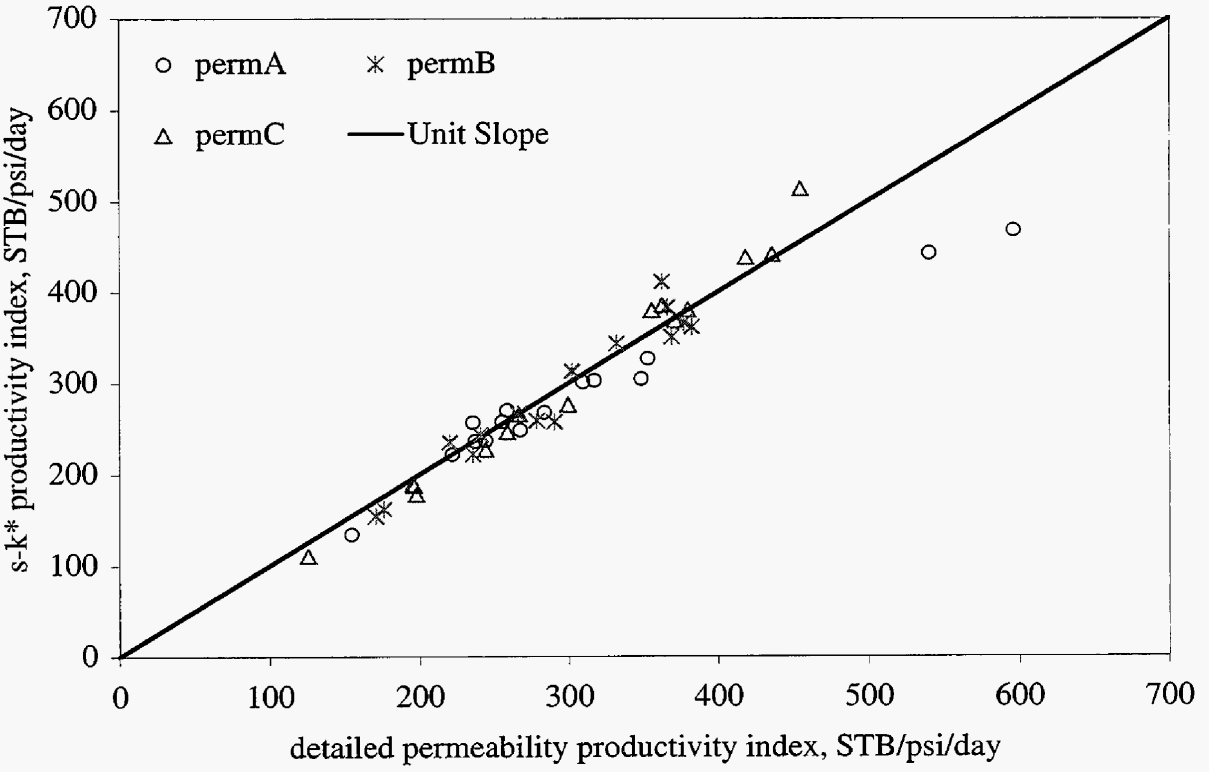

Fig. 6-4: Scatter plot of P_l estimated from s-$\mathbf{k}^*$ approach and detailed **k** descriptions

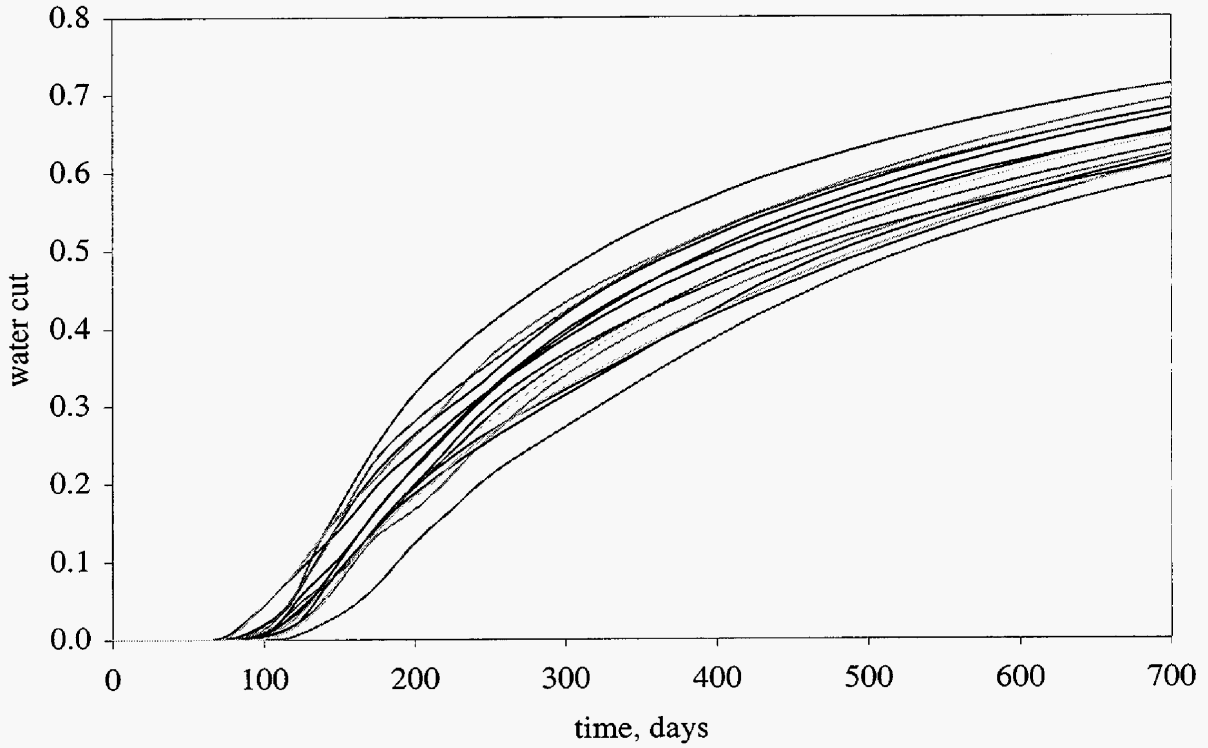

Fig. 6-5: Water cut profiles (detailed **k**, permB)

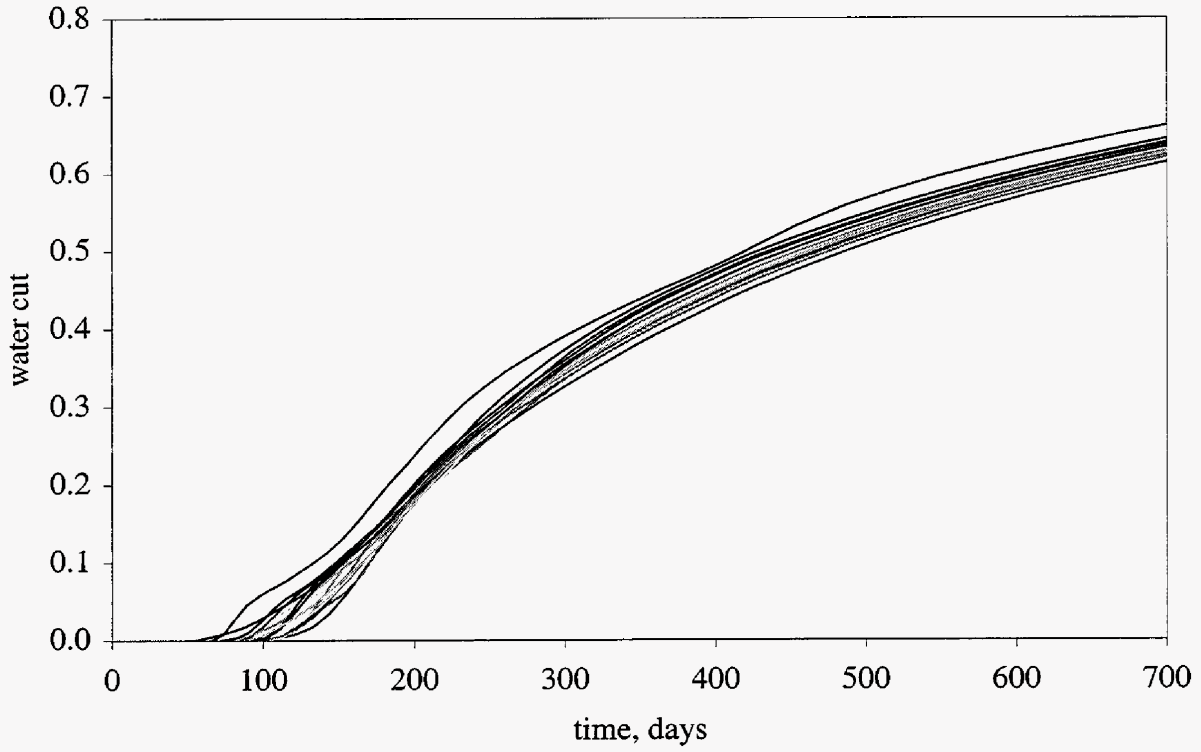

Fig. 6-6: Water cut profiles (s-$\mathbf{k}^*$, permB)

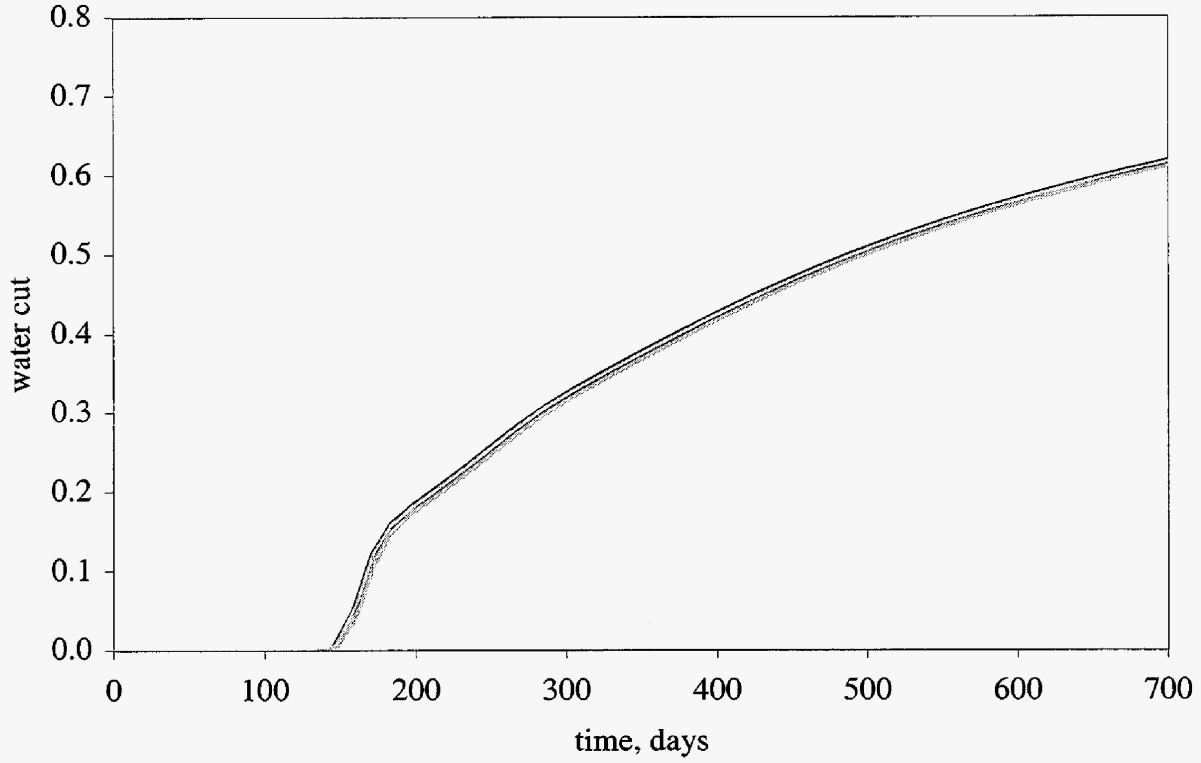

Fig. 6-7: Water cut profiles ($\mathbf{k}^*$, permB)

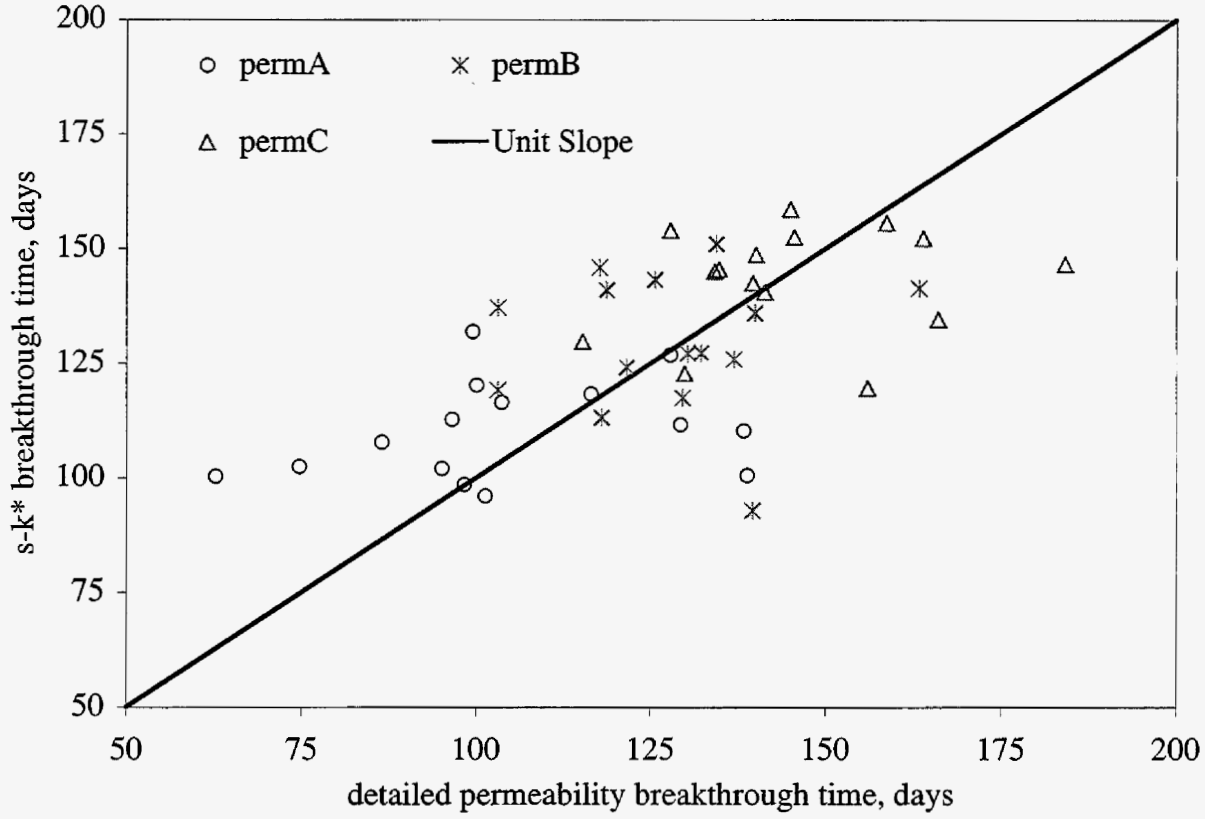

Fig. 6-8: Scatter plot of breakthrough times estimated from s-$\mathbf{k}^*$ and detailed **k** descriptions

6.3.2 Fixed oil rate cases with BHP constraint. The next cases involve a horizontal well producing at a fixed oil rate of 30,000 STB/d subject to a minimum bottom hole pressure constraint of 1500 psi. The reservoir is again underlain by an aquifer, but in this case the aquifer is much weaker (of pore volume about three times that of the reservoir) than in the previous examples. As a result, the well produces at the specified oil rate for some time (the plateau period, which is on the order of 700-1200 days) and then, once the bottom hole pressure constraint is reached, production declines.

In **Figs. 6-9** to **6-11**, we present results for oil rate Q_o versus time for the 15 permB realizations modeled using the detailed permeability fields, s-$\mathbf{k}^*$ and homogeneous permeability representations. There is significant variation in the period of plateau production t_p in the detailed **k** cases. Both the overall average and variation in t_p appear to be captured accurately by the s-$\mathbf{k}^*$ method. The homogeneous runs clearly do not capture this variation.

Table 6-5 displays results for $\overline{t_p}$ and σ_t for all of the cases considered. These results quantify the observations made above. Specifically, the s-$\mathbf{k}^*$ permeability representation is able to capture the average and variation in the plateau production period with good accuracy. This finding holds for all three sets of permeability statistics considered. The homogeneous permeability representation overpredicts slightly the period of plateau production (by about 10%) though it significantly underpredicts the variation around the mean. Results for productivity index as a function of time, though not shown, display similar levels of accuracy for the s-$\mathbf{k}^*$ method relative to the detailed **k** representation.

Table 6-5: Plateau Production Summary Statistics

	permA		permB		permC	
	t_p	σ_t	t_p	σ_t	t_p	σ_t
dk	931.2	141.6	952.6	125.6	1005.9	187.5
s-$\mathbf{k}^*$	945.3	147.0	1004.7	154.8	1032.9	213.6
$\mathbf{k}^*$	1008.0	26.7	1064.5	13.9	1094.3	6.6

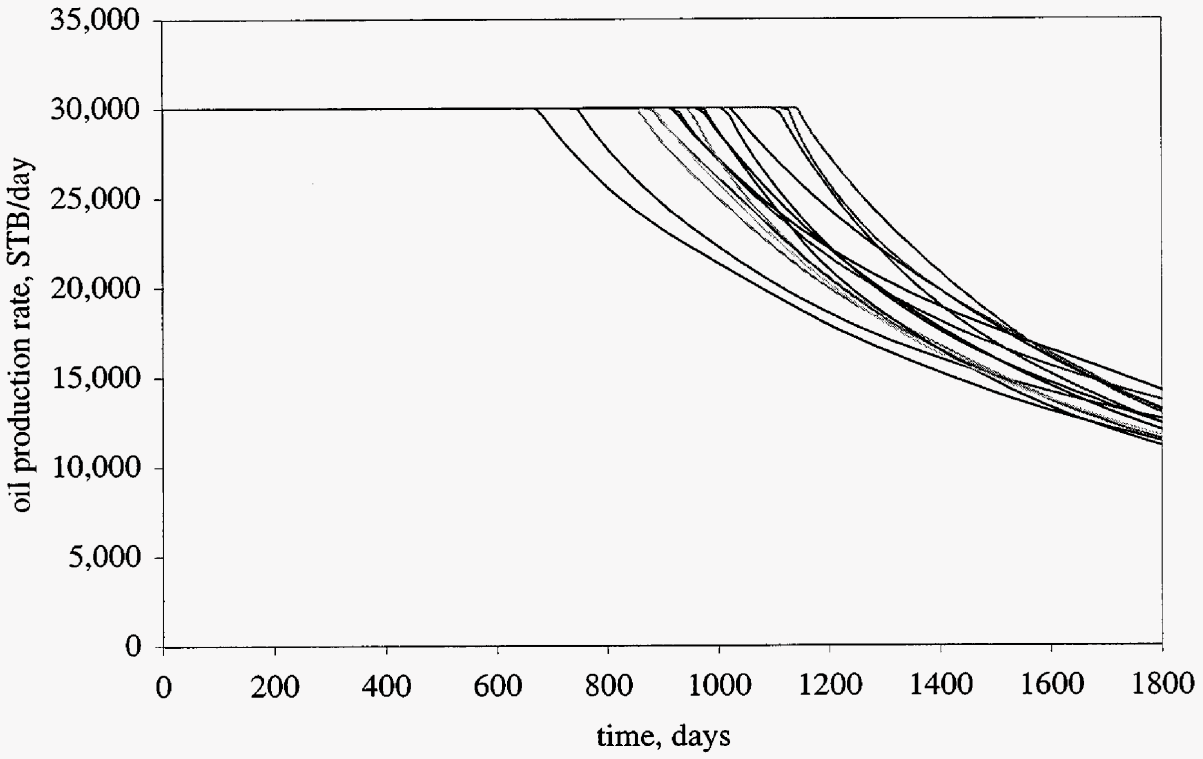

Fig. 6-9: Oil production profiles (detailed **k**, permB)

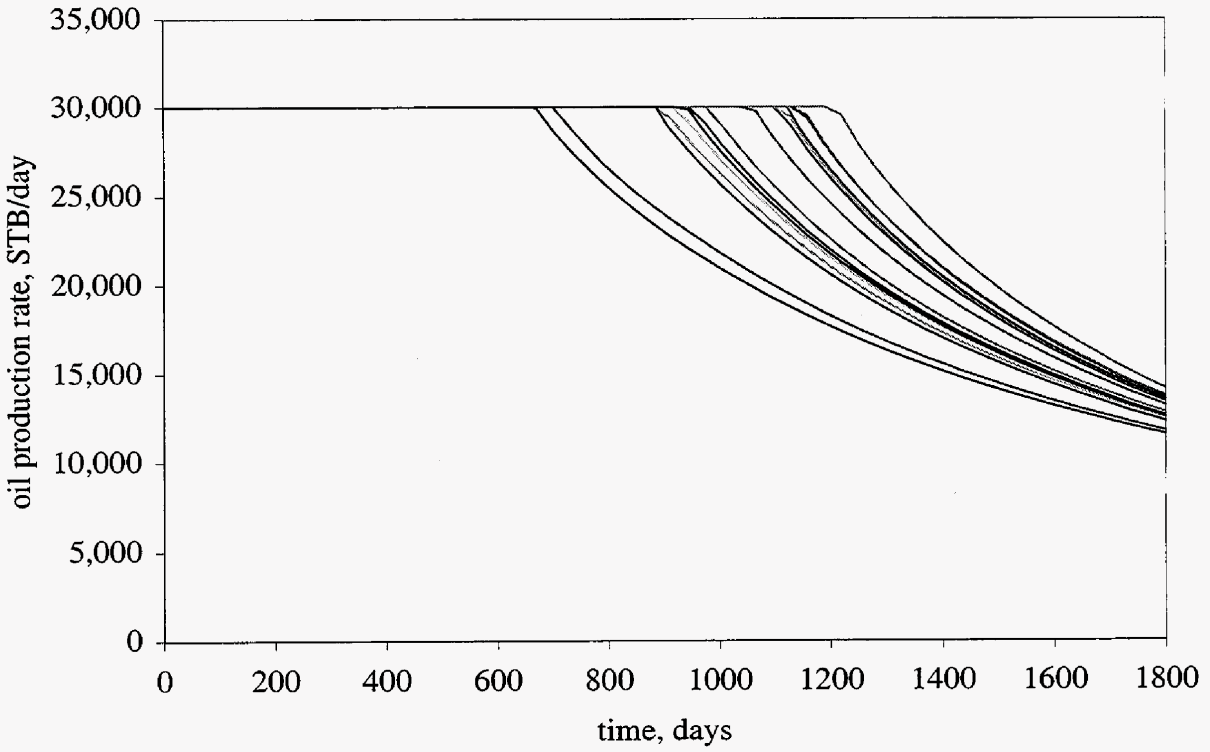

Fig. 6-10: Oil production profiles (s-$\mathbf{k}^*$, permB)

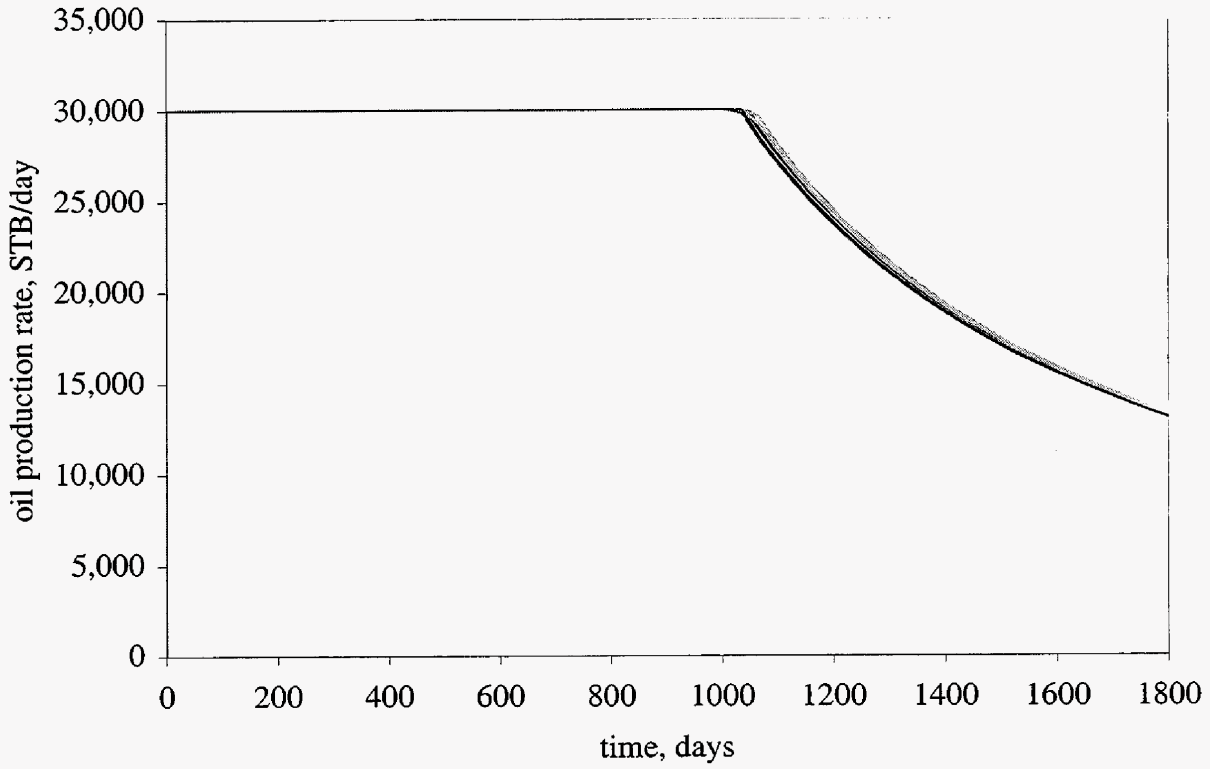

Fig. 6-11: Oil production profiles ($\mathbf{k}^*$, permB)

6.3.3 Unfavorable mobility ratio displacements. The displacements in the previous examples involved a favorable mobility ratio (endpoint water mobility less than endpoint oil mobility). To test the accuracy of the s-$\mathbf{k}^*$ method in more general cases, we also simulated the permA, permB and permC heterogeneity fields using fluid properties that resulted in an unfavorable mobility ratio displacement. For these runs, we set μ_o=4 cP, μ_w =0.38 cP, $k_{ro}(S_{wc})$=1.0 and $k_{rw}(S_{or})$=0.4. In addition, for these runs we introduced a density difference between oil and water (ρ_o =49 lb_m/ft^3 and ρ_w =63 lb_m/ft^3). For these simulations, the total liquid rate was fixed at 20,000 STB/d and a strong aquifer was present (as in the results presented in Figs. 6-2 to 6-9 and Tables 6-2 to 6-4).

Results for productivity (at 610 days) and breakthrough time for these unfavorable mobility ratio calculations are shown in **Tables 6-6** and **6-7**. From the tables, it is clear that the level of accuracy of the s-$\mathbf{k}^*$ results for these runs is comparable to that achieved in the unfavorable mobility ratio case (Tables 6-2 and 6-3). Specifically, both the average and variation in productivity are generally estimated with good accuracy (the permA results for productivity index are, however, less accurate in this case). Inspection of the results for individual realizations indicates that there is a close one to one correspondence between predictions using the detailed permeability and s-$\mathbf{k}^*$ descriptions. Similarly, the results for breakthrough time are consistent with those generated for the favorable mobility ratio case. These results clearly indicate that the s-$\mathbf{k}^*$ permeability description is applicable for a variety of two phase flow scenarios. Further, its accuracy does not appear to be strongly dependent on the details of the fluid and rock-fluid properties.

Table 6-6: Productivity Index Statistics for Unfavorable Mobility Ratio Runs (610 Days)

	permA		permB		permC	
	P_l	σ_p	P_l	σ_p	P_l	σ_p
dk	200.2	51.4	174.5	40.2	178.1	55.8
s-$\mathbf{k}^*$	169.7	46.1	169.0	43.8	176.5	64.5
$\mathbf{k}^*$	169.8	5.72	166.5	1.1	168.1	0.7

Table 6-7: Breakthrough Time Statistics for Unfavorable Mobility Ratio Runs

	permA		permB		permC	
	t_b	σ_t	t_b	σ_t	t_b	σ_t
dk	13.2	2.6	17.0	2.1	18.7	3.3
s-$\mathbf{k}^*$	13.1	1.7	15.7	2.4	17.7	2.6
$\mathbf{k}^*$	20.4	0.6	22.2	0.2	22.9	0.2

6.3.4 Use of s-$\mathbf{k}^*$ representation on coarser grids. From the results presented thus far, it is apparent that the s-$\mathbf{k}^*$ permeability representation is able to capture many quantities with good accuracy relative to the detailed permeability models. In general, the s-$\mathbf{k}^*$ permeability representation provides better results for global (integrated) quantities such as productivity index or plateau production period. Results for more local quantities such as water breakthrough time or water cut are generally less accurate. However, these results are still more accurate, relative to the detailed simulations, than the homogeneous runs. In the calculation of water breakthrough time, for example, the s-$\mathbf{k}^*$ permeability representation was able to provide estimates for $\overline{t_b}$ and σ_t in relatively close agreement with the detailed results.

Our intent in the examples above was to demonstrate the applicability of the basic s-$\mathbf{k}^*$ permeability representation for the calculation of many flow quantities of interest. The s-$\mathbf{k}^*$ model has the advantage of providing a relatively simple finite difference model that might be expected to require less CPU time than the finite difference model with the detailed permeability field (for models of the same grid dimensions). Interestingly, this was not found to be the case; the s-$\mathbf{k}^*$ models generally required about 30% more CPU time than the detailed $\mathbf{k}$ models. This is presumably due to the extra complications introduced into the model by the varying skin. It is possible that these timings could be improved through some tuning of convergence and solver parameters, but this was not attempted. Rather, because the basic s-$\mathbf{k}^*$ representation lends itself quite naturally to application on coarser models, we generated and simulated several coarse grid s-$\mathbf{k}^*$ models, as we now describe.

Starting with a detailed permeability field, an s-$\mathbf{k}^*$ model can be developed for a finite difference grid of any dimensions. The effective permeability is computed directly from the detailed permeability field, so it is unchanged as the model is coarsened. The skin in each well

block is also computed from the fine grid permeability field, though it will vary as the grid is coarsened. This is because the length of the well segment in a given well block increases as the grid is coarsened and as a result the integration domain in Eq. 6-2 changes. This in turn modifies the altered (near-well) permeability $k_{a,i}$ and thus the skin s_i in Eq. 6-1.

Using coarse grid s-$\mathbf{k}^*$ models generated in this way, we repeated many of the calculations presented above. The first set of results is for the 15 permB realizations simulated on a 23×23×17 grid using the s-$\mathbf{k}^*$ permeability representation. Results for productivity index P_l for the case of fixed total liquid rate and fluid properties indicated in Table 6-1 are shown in **Fig. 6-12** (compare this figure to Figs. 6-1 and 6-2). The close agreement between this figure and Fig. 6-2 demonstrates that the s-$\mathbf{k}^*$ representation does in fact maintain its accuracy on coarsened grids.

This is further demonstrated in **Fig. 6-13**, where we present results for the difference in productivity index (ΔP_l) between the fine grid and s-$\mathbf{k}^*$ results. Here, $\Delta P_l = P_l^{d\mathbf{k}} - P_l^{s\text{-}\mathbf{k}^*}$; i.e., ΔP_l quantifies the error in the s-$\mathbf{k}^*$ solution relative to the detailed $\mathbf{k}$ solution. Similarly, ΔP_l can be defined for the homogeneous case ($\Delta P_l = P_l^{d\mathbf{k}} - P_l^{\mathbf{k}^*}$). In Fig. 6-13, results for ΔP_l are presented for three different levels of grid refinement. We refer to these three different grids as the fine grid (45×45×35), the medium grid (23×23×17), and the coarse grid (15×15×11). The squares, triangles and ×'s correspond to ΔP_l for the fine, medium and coarse grid s-$\mathbf{k}^*$ solutions, respectively. The circles correspond to ΔP_l for the fine grid homogeneous case. The results presented are for ΔP_l computed for each of the 15 permB realizations at a time of 10 days.

From the figure, it is clear that there is very little variation in the ΔP_l results computed using the s-$\mathbf{k}^*$ permeability representation as the grid is coarsened (i.e., the squares, triangles and ×'s are quite close together for a given realization). In addition, ΔP_l for the s-$\mathbf{k}^*$ results, even on grids as coarse as 15×15×11, is generally less than ΔP_l for the homogeneous runs on the fine grid. This indicates that the coarse grid s-$\mathbf{k}^*$ results for P_l are in general more accurate than the fine grid homogeneous results.

In **Fig. 6-14** we present results for water cut using the s-$\mathbf{k}^*$ model on the medium grid (compare this figure to Figs. 6-5 and 6-6). Again, it is apparent that curves for the 15 realizations

vary relatively little as the s-$\mathbf{k}^*$ model is coarsened from 45×45×35 to 23×23×17. This is further illustrated in **Fig. 6-15**, where results for differences in water breakthrough time (relative to the detailed permeability model) are presented for the s-$\mathbf{k}^*$ model at the three different levels of grid refinement and for the fine grid homogeneous model. There is more variation here than in the P_l results (Fig. 6-13), particularly on the coarse grid. However, the s-$\mathbf{k}^*$ model continues to provide, on average, a better representation of t_b than the homogeneous model, even for the coarsest grid considered.

There is also a clear trend in these results, with $t_b^{s\text{-}\mathbf{k}^*}$ increasing by 5.6 days (on average) as we go from the fine grid to the medium grid. Similarly, going from the medium grid to the coarse grid increases $t_b^{s\text{-}\mathbf{k}^*}$ by about 10 days. This suggests that the variation in $t_b^{s\text{-}\mathbf{k}^*}$ observed here is largely due to numerical discretization effects (rather than an inaccurate permeability representation). This was in fact verified through simulations with the homogeneous model, which showed a very similar variation in t_b with grid dimension.

The results presented in this section demonstrate that the s-$\mathbf{k}^*$ permeability representation does in fact lend itself to application on coarse grids. Reasonable accuracy relative to the detailed $\mathbf{k}$ fine grid results, and relative to the fine grid s-$\mathbf{k}^*$ results, is maintained in the coarse grid s-$\mathbf{k}^*$ models. This indicates that the s-$\mathbf{k}^*$ approach is useful not only because it provides a highly simplified model (relative to the detailed permeability description) but also because it can be used to generate reasonably accurate (and highly efficient) coarse grid models.

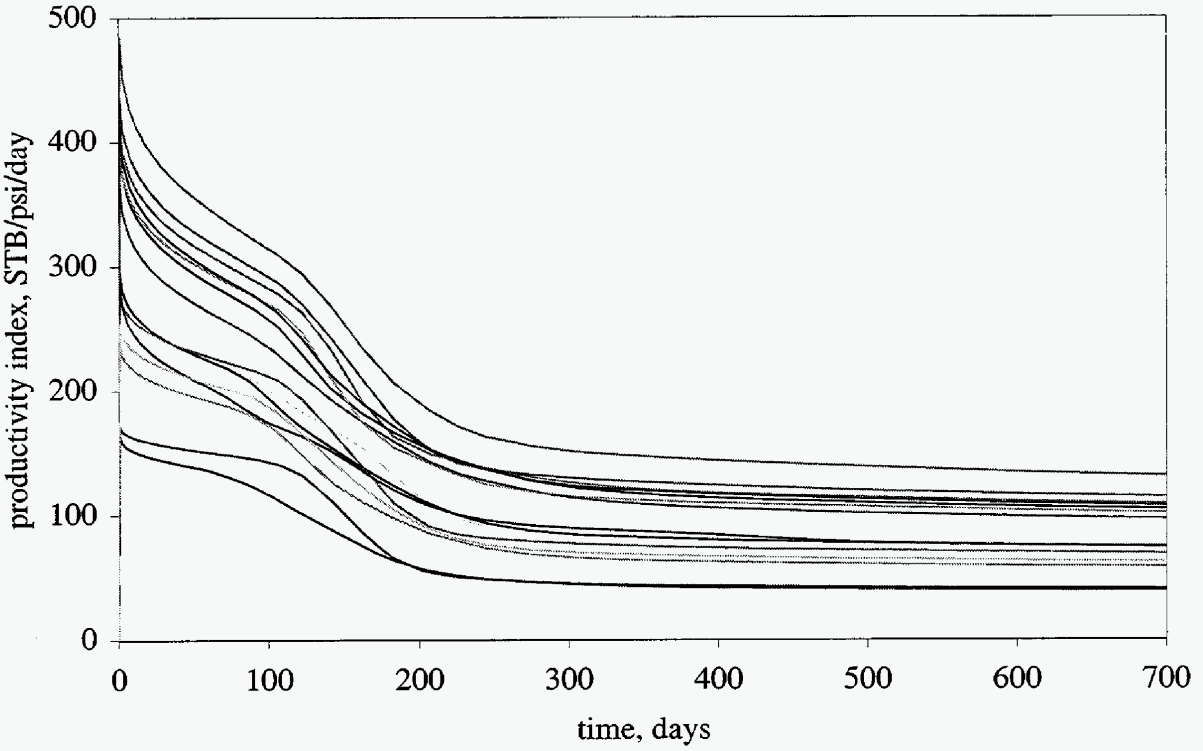

Fig. 6-12: Productivity index profiles (s-$\mathbf{k}^*$, permB) on medium grid (23×23×17)

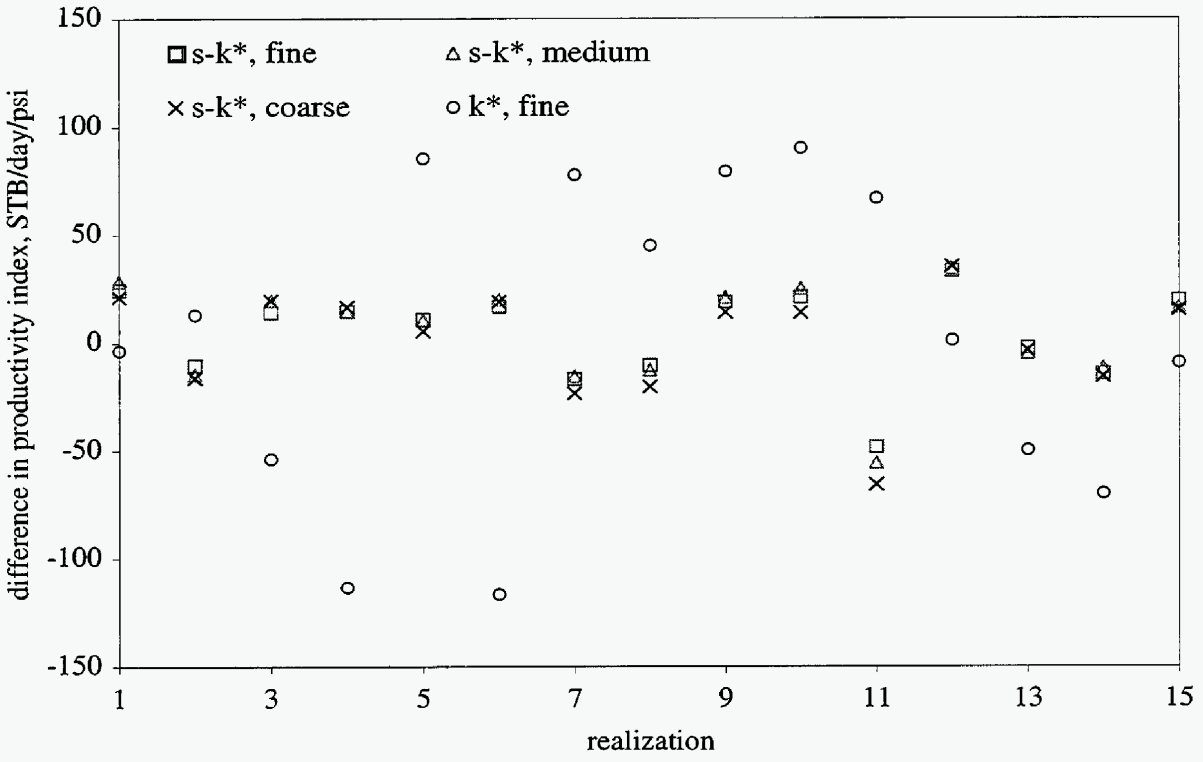

Fig. 6-13: Differences in productivity index at 10 days (relative to $P_l^{d\mathbf{k}}$) at different grid levels

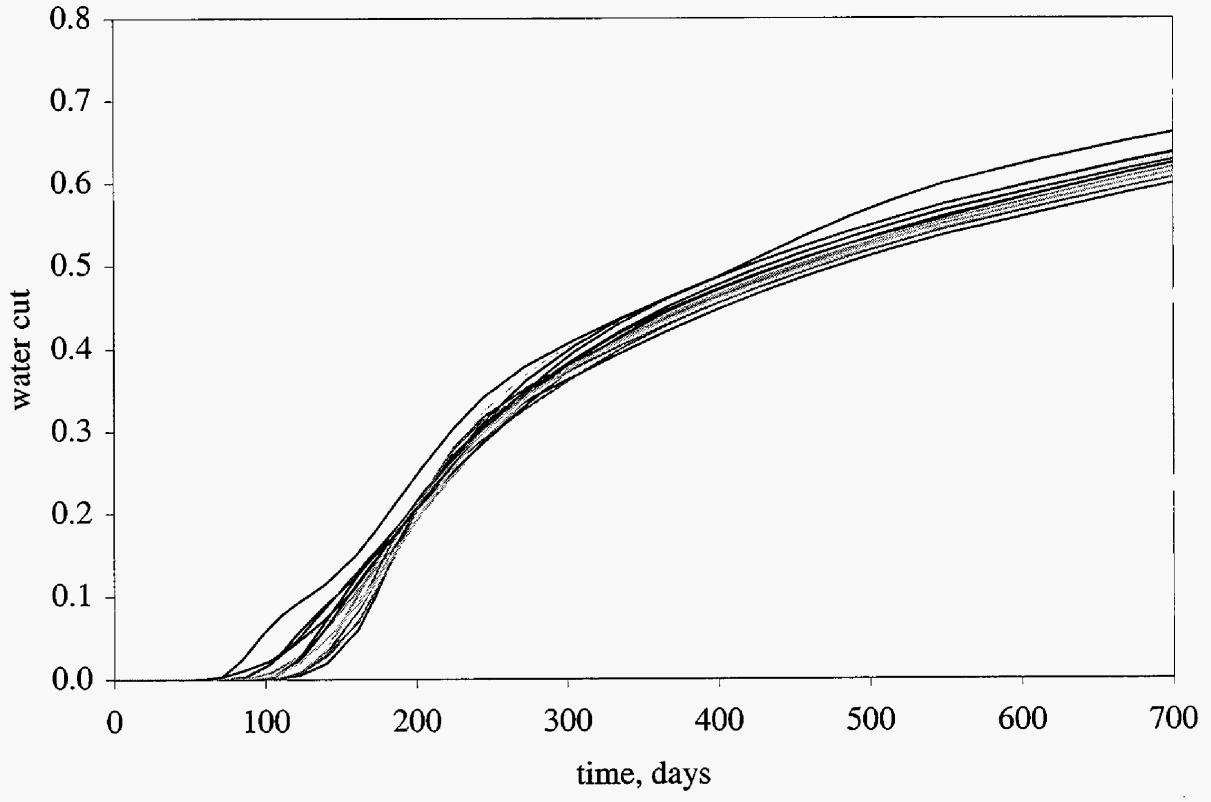

Fig. 6-14: Water cut profiles (s-$\mathbf{k}^*$, permB) on medium grid (23×23×17)

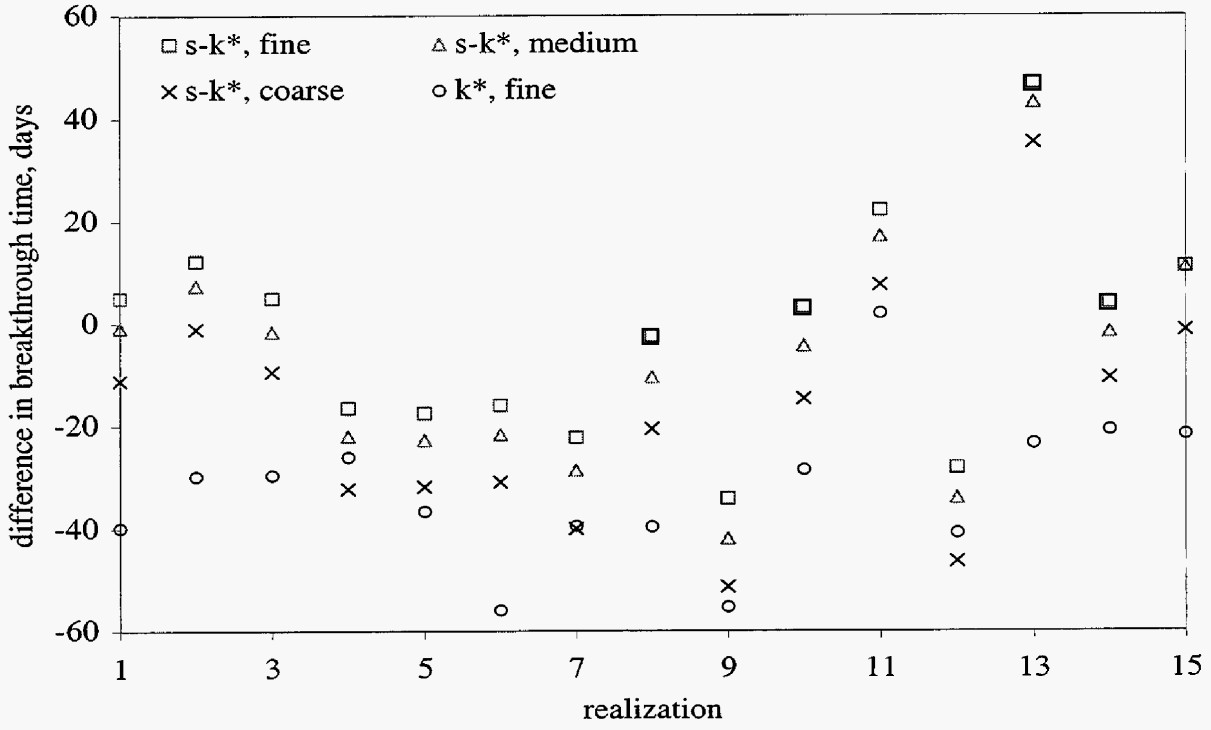

Fig. 6-15: Differences in breakthrough time (relative to $t_b^{d\mathbf{k}}$) at different grid levels

6.4 Discussion and Conclusions

In this work, we assessed the applicability of the s-$\mathbf{k}^*$ approximate permeability representation for modeling the performance of horizontal wells in heterogeneous reservoirs. We considered two phase flow problems, with the flow driven by a single horizontal producer. The simplified permeability representation entails the use of a constant background permeability $\mathbf{k}^*$ coupled with a near-well skin s that varies in each simulation well block. The background permeability captures large scale (global) flow effects while the variable skin approximates the effects of near-well heterogeneity.

The general level of accuracy of the method was established through extensive comparisons to detailed finite difference results. The method was shown to provide quite accurate results for integrated or global quantities, such as productivity index or plateau production period, both in terms of ensemble average and variation around this average. The method also provides reasonably accurate estimates of averages of local quantities such as water breakthrough time and water cut. The variation in these quantities, particularly water cut at late time, is however significantly underpredicted by the s-$\mathbf{k}^*$ permeability representation.

The method was also shown to provide substantially coarsened models that provide results in reasonable agreement with the fine grid s-$\mathbf{k}^*$ simulations (and thus with the detailed permeability results). Some degradation was observed in watercut predictions, though this was attributed more to numerical inaccuracies rather than inaccuracies in the permeability representation. We reiterate that specialized approaches appropriate for use with horizontal wells, as discussed in Chapter 5, do exist to coarsen detailed finite difference representations to coarser scales (e.g., Ding, 1995; Muggeridge et al., 1999; Mascarenhas and Durlofsky, 2000 – see Chapter 5). These approaches would be expected to provide more accurate coarse models than would the use of the s-$\mathbf{k}^*$ representation. However, these methods require the use of the full, detailed permeability field, which the s-$\mathbf{k}^*$ approach avoids.

The methodology presented in this work may be applicable to reservoir modeling in cases where near-well permeability and large scale (background) permeability can be estimated but a full, detailed geostatistical model is not available. Near-well permeability data can be estimated from well log and core data; large scale permeability may be available from well tests, from pro-

duction data, or from other data in nearby regions of the field. Then, given an estimate for $\mathbf{k}^*$ and permeability in the near-well region, skin in the well blocks can be estimated and the well performance modeled with an s-$\mathbf{k}^*$ permeability representation. This would represent an efficient but reasonably accurate means of simulating a reservoir with limited geological information.

6.5 References

Ababou, R.: "Identification of Effective Conductivity Tensor in Randomly Heterogeneous and Stratified Aquifers," presented at the Fifth Canadian-American Conference on Hydrogeology, Calgary, Sept. 18-20, 1990.

Aziz, K., Arbabi, S. and Deutsch, C.V.: "Why is it so Difficult to Predict the Performance of Horizontal Wells?" *JCPT*, 37-45, Oct. 1999.

Basquet, R., Alabert, F.G., Caltagirone, J.P. and Batsale, J.C.: "A Semi-Analytical Approach for Productivity Evaluation of Wells with Complex Geometry in Multilayered Reservoirs," paper SPE 49232 presented at the SPE Annual Technical Conference and Exhibition, New Orleans, Sept. 27-30, 1998.

Brekke, K. and Thompson, L.G.: "Horizontal Well Productivity and Risk Assessment," paper SPE 36578 presented at the SPE Annual Technical Conference and Exhibition, Denver, Oct. 6-9, 1996.

Deutsch, C. and Journel, A.G.: GSLIB: *Geostatistical Software Library and User's Guide*, 2nd edition, Oxford University Press, 368 p, 1998.

Ding, Y.: "Scaling-up in the Vicinity of Wells in Heterogeneous Field," paper SPE 29137 presented at the 1995 SPE Symposium on Reservoir Simulation, San Antonio, Texas, Feb. 12-15, 1995.

Durlofsky, L.J.: "An Approximate Model for Well Productivity in Heterogeneous Porous Media," *Math. Geol.*, **32**, 421-438, 2000.

Eclipse Reservoir Simulator, 99A Release, GeoQuest, Schlumberger, 1999.

Gharbi, R., Peters, E. and Garrouch, A.: "Effect of Heterogeneity on the Performance of Immiscible Displacement with Horizontal Wells," *J. Pet. Sci. and Eng.*, **18**, 35-47, 1997.

Hawkins, M.F.: "A Note on the Skin Effect," Trans. AIME **207**, 356-57, 1956.

Lee, S.H. and Milliken, W.J.: "The Productivity Index of an Inclined Well in Finite-Difference Reservoir Simulation," paper SPE 25247 presented at the SPE Symposium on Reservoir Simulation, New Orleans, Feb. 28-Mar. 3, 1993.

Mascarenhas, O. and Durlofsky, L.J.: "Coarse Scale Simulation of Horizontal Wells in Heterogeneous Reservoirs," *J. Pet. Sci. and Eng.*, **25**, 135-147, 2000.

Muggeridge, A.H., Cuypers, M., Bacquet, C. and Barker, J.W.: "Scale-up of Well Performance for Reservoir Flow Simulation," presented at the 1999 European Symposium on Improved Oil Recovery, Brighton, UK, Aug. 18-20.

Ouyang, L.-B. and Aziz, K.: "A Simplified Approach to Couple Wellbore Flow and Reservoir Inflow for Arbitrary Well Configuration," paper SPE 48936 presented at the SPE Annual Technical Conference and Exhibition, New Orleans, Sept. 27-30, 1998.

Wolfsteiner, C., Durlofsky, L.J. and Aziz, K.: "Approximate Model for Productivity of Nonconventional Wells in Heterogeneous Reservoirs, *SPEJ*, 218-226, June 2000a.

Wolfsteiner, C., Durlofsky, L.J. and Aziz, K.: "Efficient Estimation of the Effects of Wellbore Hydraulics and Reservoir Heterogeneity on the Productivity of Non-Conventional Wells," paper SPE 59399 presented at the SPE Asia Pacific Conference, Yokohama, Japan, April 25-26, 2000b.

Yamada, T. and Hewett, T.A.: "Production-Based Effective Vertical Permeability for a Horizontal Well, *SPERE*, 163-168, Aug. 1995.

7 Potential Application of New Modeling Approaches to Simulation While Drilling

Many of the approaches presented in this report (e.g., those described in Chapters 3, 5 and 6) represent efficient means for estimating the inflow and pressure profiles along a horizontal or other non-conventional well. The methods provide varying degrees of accuracy and computational efficiency. The appropriate method to use for a given problem will depend on the particular application, available data and required result. For example, if flow is strictly single phase and many realizations are to be modeled, the semi-analytical s-$\mathbf{k}^*$ approach might be the most appropriate approach. On the other hand, if the flow is multiphase and only a few scenarios are to be considered (and high accuracy is required), the general upscaling approach described in Chapter 5 might be the most suitable.

An important optimization problem that represents a significant challenge to the petroleum industry is the determination of the optimum length and trajectory of a non-conventional well while it is being drilled. Such a capability is conceivable, because detailed logging while drilling (LWD) and measurement while drilling (MWD) data are available during the drilling operation. In addition, the general geological setting and presumably some estimate of the relevant geostatistical parameters might also be available. Thus, real-time Simulation While Drilling (SWD) may be possible, provided sufficiently fast and accurate tools for evaluating well performance under many different scenarios were available.

Depending on the particular application, one of the methods presented in this report could potentially serve as the well performance model for such an optimization. The methods described in Chapters 3, 5 and 6 are computationally efficient and are capable of providing accurate estimates of the inflow and pressure profiles along non-conventional wells for a variety of cases. Again, the appropriate method to use will depend on the particular application. Additional complications, such as effects due to well completion and multiphase flow within the wellbore, may also have to be approximated. In subsequent work, we plan to assess the applicability of the methods presented in this report to simulation while drilling. More accurate, more computationally demanding approaches, such as upscaled finite difference models with specialized gridding schemes (i.e., models with modular grids), will also be considered.